Doctoral Dissertation

Precise Design and Construction of M−N_x Active Sites in Carbon-based Single-atom Catalysts Using Nitrogen-doped Nanographene Precursors

Koki Matsumoto

January 2022

Graduate School of Engineering,
Osaka University

Contents

General Introduction

In chemistry and biology, catalysts are key substances which accelerate reactions enabling high selectivity of products while maintaining their initial forms after reaction cycles. Developments of the catalysts have changed the industrial structure by enhancing the production efficiencies for chemicals. In this sense, catalysts are regarded as one of the major contributors to the growth of world economy. Even today, great efforts have been continuously devoted to developing catalysts for improving energy conversion (ex. fuel cells, water splitting) and resource acquisition (ex. N_2 fixation, CO_2 reduction) systems toward realizing sustainable and carbon neutral society.

Catalysts are primarily categorized into two: homogeneous and heterogeneous. Homogeneous catalysts such as soluble metal complexes and enzymes have a uniform structure of the active site and work in the same phase with reactants. They have the advantages due to their defined chemical structures: it is relatively easy to precisely describe the catalytic mechanism and finely tune their reactivity by chemical modification of the structures of their active sites including the active centers and the surrounding environments. Many challenging tasks have been achieved for synthesis of complicated compounds represented by natural products using homogeneous catalysts. However, separation from reactants sometimes becomes an issue in use of homogeneous catalysts. Moreover, their instability limits their practical application. Therefore, homogeneous catalysts are generally difficult to industrially use.

Heterogeneous catalysts, such as zeolites and metal nanoparticles on solid support, are assemblies of metal atoms. The metal atoms presented on the surface of the catalyst promote reactions in distinct phases with reactants. In contrast to homogeneous catalysts, they have excellent durability and can be easily separated and recovered from reaction mixtures. In addition, they are suitable for mass production. Because of these advantages, heterogeneous catalysts have been successful in industrial world.

The main issue of heterogeneous catalysts is their structural complexity. For example, metal nanoparticles have active metal atoms on the various locations: vertices, edges, and faces. Therefore, all active metal atoms have different intrinsic reactivities due to varied coordination environments. In addition, defects in metal nanoparticles add complexity. Due to their heterogeneous surfaces and indistinct structure of the active sites, it becomes much difficult to describe their catalytic mechanisms. It is, therefore, challenging to establish a straightforward strategy for developing an advanced heterogeneous catalyst.

To overcome the complexity of heterogeneous catalysts, downsizing the active species must be one approach. When the size is close to atomic level, the surface heterogeneity of the active species disappears (Figure 1). Thereby, characterization of the active sites and speculation of the catalytic mechanisms become easier. Furthermore, the utilization efficiency of the metal atoms as active species approaches 100% when all the isolated metal atoms serve a catalytic activity. In this context, single-atom catalysts containing isolated active metal atoms on heterogeneous materials have been attracted much attentions as one of the promising new families of heterogeneous catalysts.[1−3]

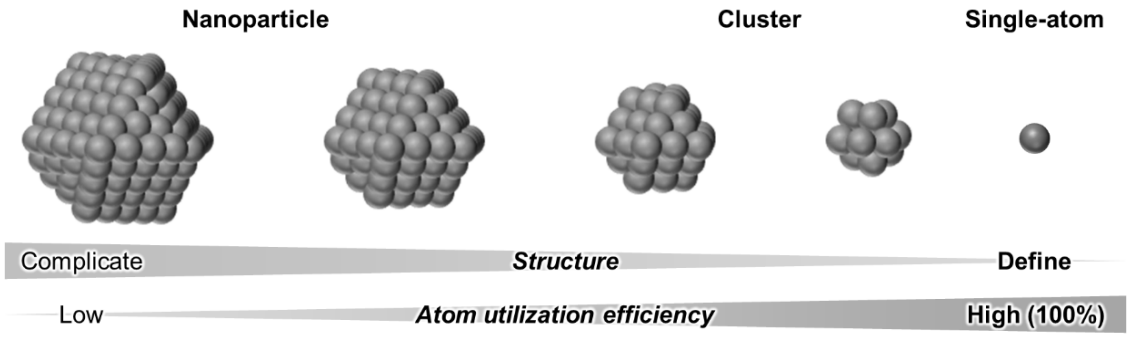

Figure 1. Downsizing a nanoparticle to a single-atom for simplifying the structure and increasing the atom utilize efficiency.

Single-atom catalyst

Single-atom catalysts (SACs) are defined as catalysts containing a homogeneous active metal species which exists as isolated single-atoms stabilized on heterogeneous support materials (Figure 2).[4–6] All active metal species in SACs possibly participate in the catalytic cycles of the reaction. In other words, the metal utilization efficiency of the active sites is potentially 100% similar to homogeneous molecular catalysts, although SACs are categorized in a group of heterogeneous catalysts. In addition, the electronic state of the active metal species is tuned by the chemical environment that the support materials serve.

The concept of SACs has been proposed by Zhang *et al*. in 2011. His group demonstrated that the isolated Pt atoms anchored on FeO_x show high catalytic activity toward CO oxidation reaction with the maximum atomic efficiency of Pt among all the catalysts.[3] Encouraged by this pioneering work, many types of the SACs containing transition metals as isolated active centers (ex. Pt, Ru, Rh, Ir, Fe, Co, Ni, Cu) on support materials (ex. metals, metal oxides, metal chalcogenides, zeolite, heteroatom-doped carbon materials) have been developed for various reactions.[7–10] According to SciFinder®, over 1100 publications about single-atom catalyst have been published in this decade.

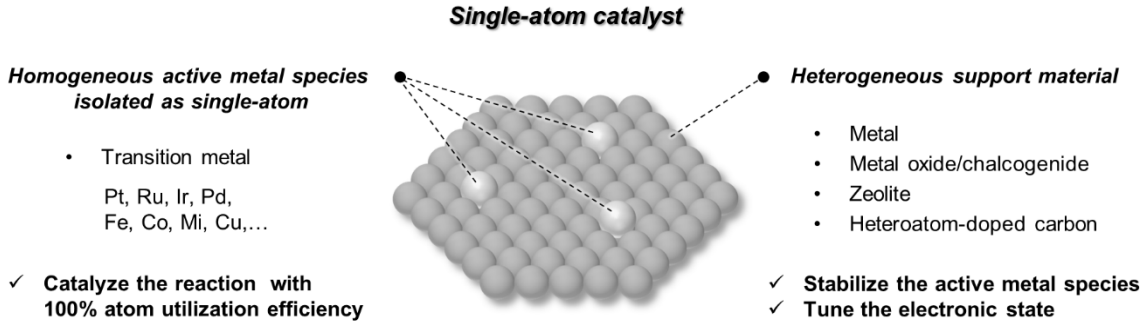

Figure 2. The Conceptual illustration of a single-atom catalyst with examples of active metal species and support materials.

M/N/C single-atom catalyst

Among the family of SACs, a catalyst containing isolated metal atoms anchored by the coordination of nitrogen atoms (M−N_x sites) as an active site is called as "M/N/C single-atom catalyst" (M = metal, N = nitrogen, C = carbon) (Figure 3a).[5,6] The chemical structure of the M−N_x active sites have been verified with the recent progress of analytical techniques for the heterogeneous catalysts (Figure 3b).[11−16] As the M−N_x sites are integrated into the π-conjugated graphene layer, the metal center of the M−N_x sites have a unique electronic structure and show an anodically shifted redox behavior derived from the electron-withdrawing nature of delocalized π-electrons in a carbon basal plane.[13,17−19] The carbon-based materials, of course, show high conductivity and thermal- and chemical-durability. Accordingly, M/N/C single-atom catalysts have been developed as electrocatalysts for oxygen reduction reaction (ORR),[20−22] hydrogen evolution reaction (HER),[23−25] oxygen evolution reaction (OER),[26−29] nitrogen reduction reaction (NRR),[16,30,31] CO_2 reduction reaction (CO_2RR),[32−35] and others.[36,37] These electrochemical reactions are pivotal to develop the environmentally friendly energy conversion and resource acquisition systems. Therefore, the family of M/N/C single-atom catalysts has been regarded as one of the most important research subjects for realizing a sustainable society.[4,38,39]

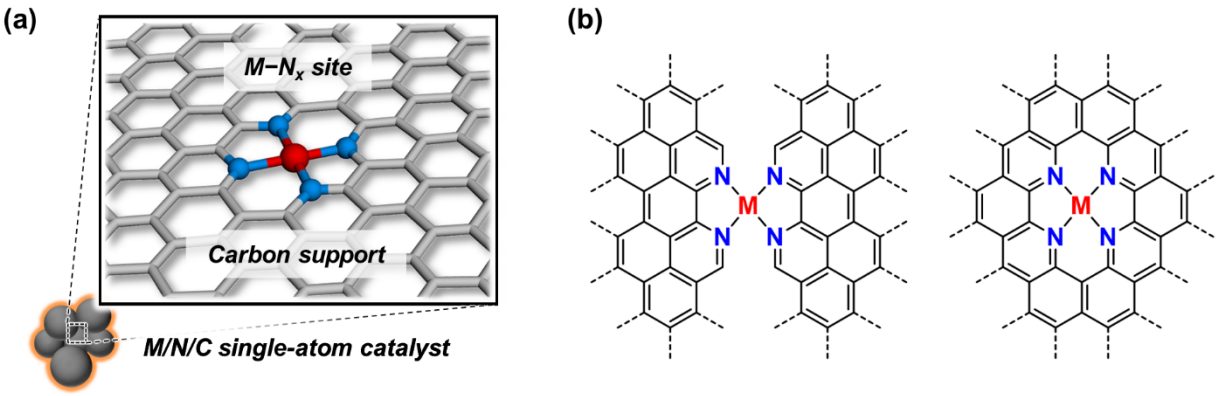

Figure 3. (a) The illustration of a M/N/C single atom catalyst. (b) The chemical structures of M−N_x sites.

Preparation of M/N/C single-atom catalyst

One of the most common preparation methods of M/N/C single-atom catalysts (M/N/C catalysts) is a high-temperature pyrolysis method.[36,40−43] This method consists of three steps; (1) preparation of a catalyst precursor containing metal, nitrogen and carbon sources, (2) pyrolysis of the precursor at appropriate temperature in the range of 600 ºC to 1000 ºC in an aerobic atmosphere, (3) acid washing to remove metal aggregates when needed (Figure 4). The prepared precursors are carbonized and merged in the graphene layer during pyrolysis, and then the M−N_x sites are randomly constructed (Figure 5). The metal aggregates would be simultaneously generated as byproducts via sintering of the metal atoms. Since the existence of the byproducts makes the identification of the active sites difficult, acid washing is often performed after pyrolysis to obtain M/N/C catalysts with high purity.

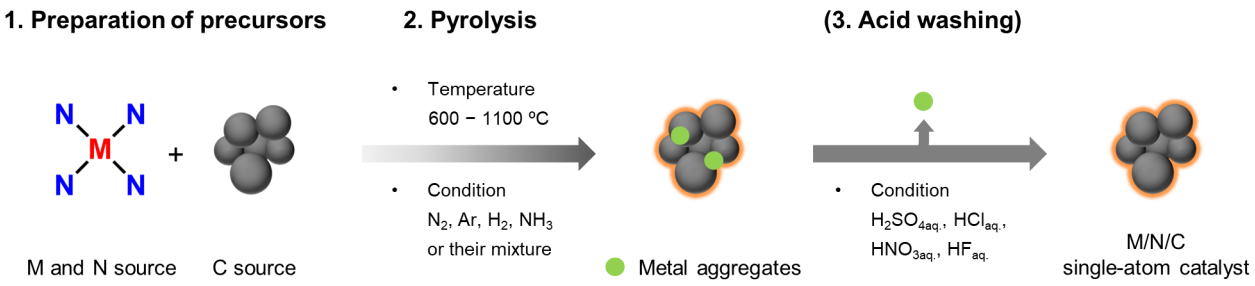

Figure 4. High-temperature pyrolysis method for the preparation of a M/N/C single-atom catalyst.

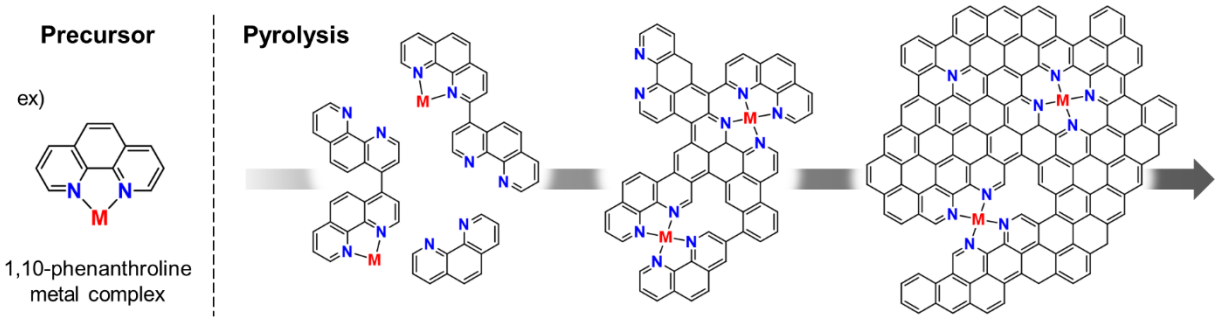

Figure 5. Schematic illustration of the graphitization and formation of M−N_x sites during pyrolysis.

The high-temperature pyrolysis method was extensively developed by Jahnke *et al*.[44] They demonstrated that the pyrolyzed transition metal macrocyclic complexes mixed with carbon supports show the improved catalytic activity for oxygen reduction reaction (ORR) and durability than those of the transition metal macrocycles complexes. This pyrolyzed material is the first example of the M/N/C catalyst, but there was little insight into the structure of active sites at that time. Nevertheless, it was believed that the partially retained metal−N_4 center on carbon derived from the metal macrocyclic complex after pyrolysis contributes to improvements of the activity and durability. Therefore, tremendous efforts have been devoted to developing the M/N/C catalyst prepared from metal macrocyclic complexes[45–48] and confirming the transformation of the precursor to the active sites by various analytical method such as thermogravimetric mass spectroscopy (TG-MS),[49] X-ray photoelectron spectroscopy (XPS),[46,50,51] time of flight secondary ion mass spectroscopy (ToF-SIMS),[52–54] and X-ray absorption fine structure (XAFS).[55,56]

The breakthrough in the preparation of the catalysts was the finding that the M/N/C catalysts with high catalytic activities can be prepared from individual metal, nitrogen, and carbon sources. In 1989, Yeager *et al*. have reported that the M/N/C catalyst prepared by pyrolysis of the mixture of polyacrylonitrile (PAN) and metal salts shows high catalytic activity for ORR.[57] This discovery expanded the range of candidates for catalyst precursors from expensive metal macrocyclic complexes to inexpensive nitrogen-containing compounds with simple metal salts and arrowed to easily optimize the molecular design of precursors and procedure for preparation of M/N/C catalysts.

The representative M/N/C catalysts which have dramatically improved activity for ORR were reported by Dodelet *et al*. in 2009 and Zelenay *et al*. in 2011. The synthetic procedure of the Dodelet's catalyst involves vigorous mixing of a carbon support (BP2000) having high surface area, with 1,10-phenanthroline and iron salts by ball milling and then, performing two-step pyrolysis for the mixture; first in Ar atmosphere, then in NH_3 atmosphere, respectively. In this report, they proposed the formation of Fe−N_4 sites at the edge of graphene layer as an active site (Figure 2b). This work also provided a finding that the active sites are efficiently constructed by spatial compartment of metal and nitrogen sources by adsorbing on large surface area of the carbon support.[58] Zelenay *et al*. investigated N-containing polymers such as polypyrrole and polyaniline with iron or cobalt salts as precursors. The N-containing polymers were converted to the carbon structure with homogeneously dispersed nitrogen atoms for anchoring metal ions after pyrolysis, resulting in achievement of high loading of the dispersed metal species in the catalysts.[59]

Based on the above findings, the family of metal-organic frameworks (MOFs), which are crystalline porous materials and are constructed by coordination of metal ions and organic linkers, have been paid attention as a promising precursor for synthesis of M/N/C catalysts. Many pioneering works relating to the MOF-based M/N/C catalysts were reported by Li *et al*.[24,60,61] They utilized the zeolitic imidazolate frameworks (ZIFs) (ex. zinc-based ZIFs, ZIF-8 and cobalt-based ZIF, ZIF-67) as precursors. ZIFs have high content of nitrogen atoms all over the materials and the 3D porous structure which allows to incorporate the other metal and nitrogen sources. In the case of ZIF-8, particularly, zinc atoms can be removed by evaporation over 907 ºC (boiling point of zinc), serving the N_x coordination sites derived via carbonization of imidazolate linkers that are available to stabilize the other doped metal atoms. As a result, ZIF-8 based precursors are effectively converted to M/N/C catalysts containing large amounts of M−N_x sites in porous carbon framework. Therefore, ZIF-8 has become a new platform of M/N/C catalysts and various types of the M/N/C catalysts have been synthesized by following this strategy.[62−64] In 2019, Wu *et al*. reported that the construction of Fe−N_x sites without generating iron aggregates during pyrolysis using iron co-doped ZIF-8 with strict adjustment of the loading amount of doped iron atoms. This Fe/N/C catalyst prepared from the iron doped ZIF-8 shows superior activity toward ORR, which is now a benchmark.[65]

The developments of M/N/C catalysts have been supported by the recent progress of analytical technology and the insight on the structure of active sites. In 2013, Mukerjee *et al*. proposed that the structure of the active sites for ORR in the Fe/N/C catalyst are an Fe−N_x coordination structure embedded within graphene layers by *in-situ* X-ray absorption spectrometry.[13] In 2017, Zelenay *et al*. succeeded direct observation of the Fe−N_x sites within graphene layer by STEM-EELS.[14] In 2021, Jaouen *et al*. proposed the detailed structure and the spin state of the Fe−N_x sites by *in-situ* ^{57}Fe Mössbauer spectroscopy with computational analysis.[66] These findings have been provided us the direction for designing the catalysts to improve the performance. However, the variation of the precursors to construct the ideal structure of the active sites has been still limited. Therefore, continuous efforts in exploring a design of precursors and developing novel approach to achieve precise and efficient constructions of active sites are required.

Synthesis of nanographenes with atomic-level precision

It is desired to creature the M–N_x active sites in a graphene layer. For this purpose, the author paid attention to the research field of carbon materials to find clues for developing a new approach to construct the M–N_x active sites.

Graphene has been regarded as one of the most attractive carbon materials because of their unique property derived from its 2D structure constructed by the π-conjugated carbons since the single graphene layer was isolated by Geim *et al*. in 2004.[67] Particularly, the graphene has been studied for the application of electronic devises because of their ultrahigh charge-carrier mobility. However, the lack of the band gap in the graphene limits its application because the devices using the graphene cannot be switched off.[68] This disadvantage has been overcome by cutting off the 2D structure of graphene to obtain quasi-zero-dimensional graphene quantum dots (QODs) or quasi-one-dimensional graphene nanoribbons (GNRs),[69,70] which are collectively called nanographenes. Their limited π-conjugation gives a band gap, making nanographenes promising materials for application as a semiconductor.

The properties of nanographenes are highly depended on their width, length, edge structure, and doped heteroatoms.[71] Synthetic methods to access nanographenes with an atomic-level precision had been required to correctly understand the structure–property relationship and produce a nanographene with desired properties. This demand has been met through developing a methodology of bottom-up synthesis. The bottom-up synthesis is usually comprised of three steps, (1) design of an aromatic compound containing aryl or heteroaryl substituents in the adjacent positions as a unit structure, (2) polymerization of the unit compound when the target compound has large width or length, and (3) cyclodehydrogenation reaction to convert the π-conjugated plane structure of the nanographene (Figure 6).[72] Various kinds of atomically precise QODs and GNRs have been synthesized through this method.

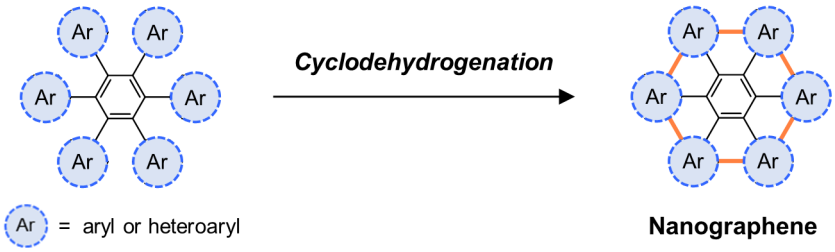

Figure 6. General synthetic scheme of nanographene compounds.

In 1990's, Müllen *et al*. reported the synthesis of hexa-*peri*-hexabenzocoronene (HBC) (Figure 7a) and other nanographenes through Scholl reaction for a cyclodehydrogenation.[73–75] Synthesis of N-doped HBC was also reported by Draper *et al*. in 2002 (Figure 7b).[76] In addition, a surface-assisted method for producing nanographenes was developed in 2010's.[77–79] In this method, the polymerization and cyclodehydrogenation are supported by metal surface upon thermal activation. This method allows to synthesize the nanographenes with low solubility. Müllen *et al*. successfully synthesized various GNRs through a surface-assisted method (Figure 7c).[70,80]

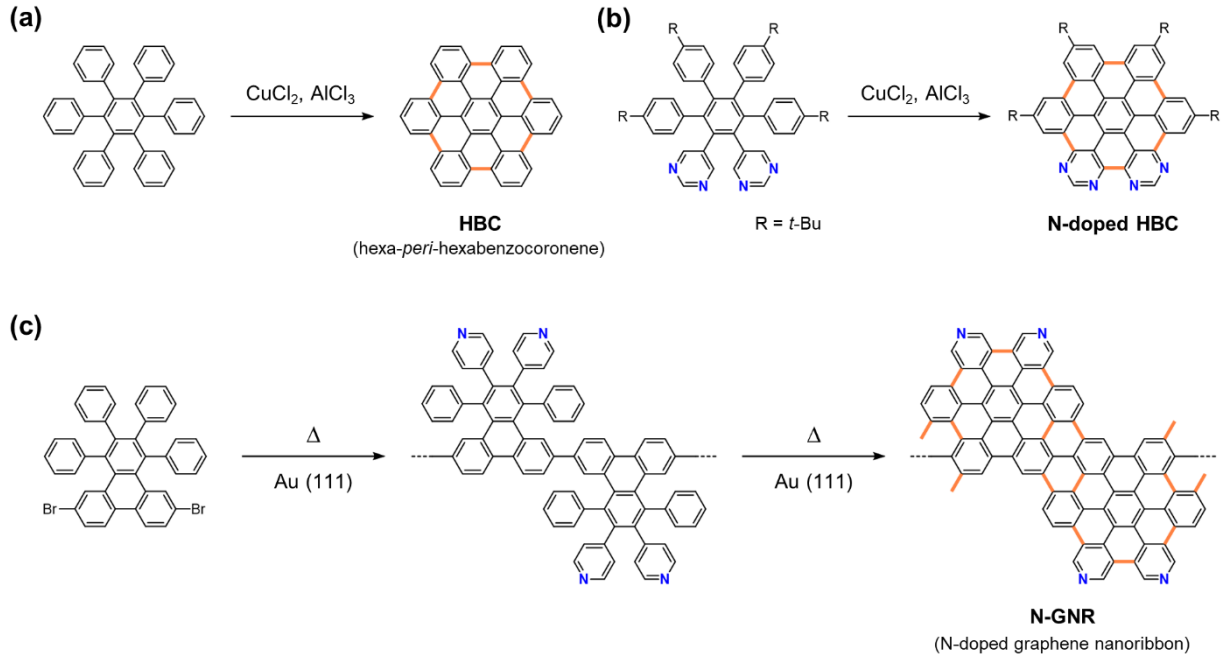

Figure 7. Synthetic schemes of (a) HBC, (b) N-doped HBC by chemical oxidation and (c) N-GNR by surface-assisted cyclodehydrogenation.

Inspired by the chemical structures of nanographenes with the atomically defined structure and doped nitrogen atoms at the desired positions, the author has been attempted to apply the synthetic method of nanographenes to preparation of M/N/C single-atom catalysts. He employed aromatic compounds, which has preorganized aryl or heteroaryl rings in the adjacent positions as a precursor for the M/N/C single-atom catalyst. When the pyrolytic treatment is performed to the precursor with a metal salt and a carbon support, it is anticipated that the cyclodehydrogenation of the precursor occurs prior to the uncontrollable graphitization, following generation of corresponding nanographenes. Therefore, the M−N_x active sites would be precisely and efficiently constructed along with the nanographene structure (Figure 8). Based on this strategy, the author developed the Fe/N/C catalyst for ORR (Chapters 1 and 3), and Co/N/C catalyst (Chapter 2) for HER from N-doped nanographene precursors to facilitate the construction of the M−N_x active sites during pyrolysis and improve the catalytic activity.

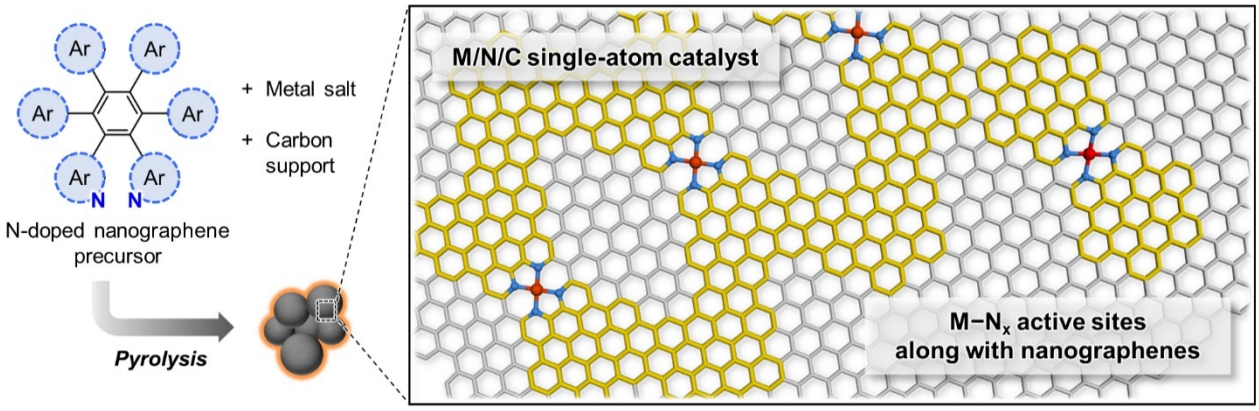

Figure 8. The strategy for the preparation of M/N/C single-atom catalysts using N-doped nanographene precursors.

Outline of This Thesis

Chapter 1: *Preparation of Fe/N/C Catalysts Using N-doped Graphene Nanoribbon Precursors for an Electrocatalytic Oxygen Reduction Reaction*

The Fe/N/C single-atom catalysts were prepared by pyrolysis of an N-doped graphene nanoribbon (N-GNR) precursor, pyridine-substituted triphenylene polymers, as nitrogen and carbon sources. The Fe−N_x active sites were efficiently constructed from the designed N-doped GNR precursor and the prepared catalyst showed high catalytic activity in electrochemical oxygen reduction reaction (ORR) under acidic condition with four-electron reduction pathway. The details of the graphitization process of the precursor were investigated by analyzing the precursors pyrolyzed at various temperatures using MgO particles as a sacrificial template. The chemical structures of the N-GNR precursors having preorganized aromatic rings and its pyrolysis conditions for graphitization were found to be important factors for generation of the Fe–N_x active sites along with the N-GNR structure in high performance Fe/N/C single-atom catalysts for the ORR.

Chapter 2: *Construction of Co−N_x Active Sites derived from Precursors Forming N-doped Graphene Nanoribbons for an Electrocatalytic Hydrogen Evolution Reaction*

The synthetic methodology based on an N-doped graphene nanoribbon (N-GNR) was applied to the construction of a Co−N_x structure in Co/N/C catalysts. Precursors, pyridine-substituted triphenylene polymers, are converted to N-GNR with cobalt-chelating N2 ligand structures during pyrolysis, and the cobalt-bound N-GNR was incorporated into the graphene layer. The existence of atomically dispersed cobalt atoms was confirmed by STEM-EELS observations. The resulting Co/N/C catalysts were highly active toward electrochemical hydrogen evolution reaction (HER) under acidic conditions.

Chapter 3: *One-step Preparation of Fe/N/C Single-atom Catalysts Containing Fe−N_4 Active Sites from an Iron Complex with Ligands Forming Nanographenes*

The Fe/N/C single-atom catalysts were prepared from iron complexes containing 5,6,7,8-tetraphenyl-1,12-diazatriphenylene ligands with two bromo substituents by one-step pyrolysis. The ligand used was a precursor of N-doped hexa-*peri*-hexabenzocoronene (N-HBC). The iron complexes were efficiently converted to atomically dispersed Fe−N_4 active sites without generating less active iron aggregates during pyrolysis. The Fe−N_4 active sites were identified by STEM-EELS observations and *in-situ* electrochemical Fe K edge X-ray absorption spectroscopic mesurements. The Fe/N/C catalysts show high catalytic activity toword ORR under acidic condition with high four-electron reduction selectivity.

References

[1] S. Mitchell, J. Pérez-Ramírez, *Nat. Commun.* **2020**, *11*, 4302.

[2] H. He, H. H. Wang, J. Liu, X. Liu, W. Li, Y. Wang, *Molecules* **2021**, *26*, 6501.

[3] B. Qiao, A. Wang, X. Yang, L. F. Allard, Z. Jiang, Y. Cui, J. Liu, J. Li, T. Zhang, *Nat. Chem.* **2011**, *3*, 634−641.

[4] L. Zhang, Y. Ren, W. Liu, A. Wang, T. Zhang, *Nat. Sci. Rev.* **2018**, *5*, 653−672.

[5] M. B. Gawande, P. Fornasiero, R. Zbořil, *ACS Catal.* **2020**, *10*, 2231−2259.

[6] Q. Zhang, X. Zhang, J. Wang, C. Wang, *Nanotechnology* **2020**, *32*, 032001.

[7] J. Liu, *ACS Catal.* **2017**, *7*, 34−59.

[8] L. Liu, A. Corma, *Chem. Rev.* **2018**, *118*, 4981−5079.

[9] S. K. Kaiser, Z. Chen, D. Faust Akl, S. Mitchell, J. Pérez-Ramírez, *Chem. Rev.* **2020**, *120*, 11703−11809.

[10] N. Cheng, L. Zhang, K. Doyle-Davis, X. Sun, *Electrochem. Energy Rev.* **2019**, *2*, 539−573.

[11] L. Li, X. Chang, X. Lin, Z.-J. Zhao, J. Gong, *Chem. Soc. Rev.* **2020**, *49*, 8156−8178.

[12] M.-X. Chen, L. Tong, H.-W. Liang, *Chem. Eur. J.* **2021**, *27*, 145−157.

[13] N. Ramaswamy, U. Tylus, Q. Jia, S. Mukerjee, *J. Am. Chem. Soc.* **2013**, *135*, 15443−15449.

[14] H. T. Chung, D. A. Cullen, D. Higgins, B. T. Sneed, E. F. Holby, K. L. More, P. Zelenay, *Science* **2017**, *357*, 479−484.

[15] L. Jiao, J. Li, L. L. Richard, Q. Sun, T. Stracensky, E. Liu, M. T. Sougrati, Z. Zhao, F. Yang, S. Zhong, H. Xu, S. Mukerjee, Y. Huang, D. A. Cullen, J. H. Park, M. Ferrandon, D. J. Myers, F. Jaouen, Q. Jia, *Nat. Mater.* **2021**, *20*, 1385−1391.

[16] S.-Y. Lv, C.-X. Huang, G. Li, L.-M. Yang, *ACS Appl. Mater. Interfaces* **2021**, *13*, 29641−29653.

[17] U. Tylus, Q. Jia, K. Strickland, N. Ramaswamy, A. Serov, P. Atanassov, S. Mukerjee, *J. Phys. Chem. C* **2014**, *118*, 8999−9008.

[18] U. I. Kramm, I. Herrmann-Geppert, J. Behrends, K. Lips, S. Fiechter, P. Bogdanoff, *J. Am. Chem. Soc.* **2016**, *138*, 635−640.

[19] D. Huang, Y. Luo, S. Li, L. Liao, Y. Li, H. Chen, J. Ye, *Mater. Horizons* **2020**, *7*, 970−986.

[20] J. Han, J. Bian, C. Sun, *Research* **2020**, *2020*, 9512763.

[21] H. Xu, D. Wang, P. Yang, A. Liu, R. Li, Y. Li, L. Xiao, X. Ren, J. Zhang, M. An, *J. Mater. Chem. A* **2020**, *8*, 23187−23201.

[22] C.-X. Zhao, B.-Q. Li, J.-N. Liu, Q. Zhang, *Angew. Chem. Int. Ed.* **2021**, *60*, 4448−4463.

[23] H. Fei, J. Dong, M. J. Arellano-Jiménez, G. Ye, N. Dong Kim, E. L. G. Samuel, Z. Peng, Z. Zhu, F. Qin, J. Bao, M. J. Yacaman, P. M. Ajayan, D. Chen, J. M. Tour, *Nat. Commun.* **2015**, *6*, 8668.

[24] Y. Pan, S. Liu, K. Sun, X. Chen, B. Wang, K. Wu, X. Cao, W.-C. Cheong, R. Shen, A. Han, Z. Chen, L. Zheng, J. Luo, Y. Lin, Y. Liu, D. Wang, Q. Peng, Q. Zhang, C. Chen, Y. Li, *Angew. Chem. Int. Ed.* **2018**, *57*, 8614−8618.

[25] Y. J. Sa, S. O. Park, G. Y. Jung, T. J. Shin, H. Y. Jeong, S. K. Kwak, S. H. Joo, *ACS Catal.* **2019**, *9*, 83−97.

[26] X. Li, P. Cui, W. Zhong, J. Li, X. Wang, Z. Wang, J. Jiang, *Chem. Commun.* **2016**, *52*, 13233−13236.

[27] B. Wurster, D. Grumelli, D. Hötger, R. Gutzler, K. Kern, *J. Am. Chem. Soc.* **2016**, *138*, 3623−3626.

[28] Y. Zheng, Y. Jiao, Y. Zhu, Q. Cai, A. Vasileff, L. H. Li, Y. Han, Y. Chen, S.-Z. Qiao, *J. Am. Chem. Soc.* **2017**, *139*, 3336−3339.

[29] H. Fei, J. Dong, Y. Feng, C. S. Allen, C. Wan, B. Volosskiy, M. Li, Z. Zhao, Y. Wang, H. Sun, P. An, W. Chen, Z. Guo, C. Lee, D. Chen, I. Shakir, M. Liu, T. Hu, Y. Li, A. I. Kirkland, X. Duan, Y. Huang, *Nat. Catal.* **2018**, *1*, 63−72.

[30] J. H. Montoya, C. Tsai, A. Vojvodic, J. K. Nørskov, *ChemSusChem* **2015**, *8*, 2180−2186.

[31] Y. Qiu, X. Peng, F. Lü, Y. Mi, L. Zhuo, J. Ren, X. Liu, J. Luo, *Chem. Asian J.* **2019**, *14*, 2770−2779.

[32] H. B. Yang, S.-F. Hung, S. Liu, K. Yuan, S. Miao, L. Zhang, X. Huang, H.-Y. Wang, W. Cai, R. Chen, J. Gao, X. Yang, W. Chen, Y. Huang, H. M. Chen, C. M. Li, T. Zhang, B. Liu, *Nat. Energy* **2018**, *3*, 140−147.

[33] H. Yang, Y. Wu, G. Li, Q. Lin, Q. Hu, Q. Zhang, J. Liu, C. He, *J. Am. Chem. Soc.* **2019**, *141*, 12717−12723.

[34] C. Xia, Y. Qiu, Y. Xia, P. Zhu, G. King, X. Zhang, Z. Wu, J. Y. Kim, D. A. Cullen, D. Zheng, P. Li, M. Shakouri, E. Heredia, P. Cui, H. N. Alshareef, Y. Hu, H. Wang, *Nat. Chem.* **2021**, *13*, 887−894.

[35] Y. Lu, Z. Zhang, H. Wang, Y. Wang, *Appl. Catal. B* **2021**, *292*, 120162.

[36] D. Zhao, Z. Zhuang, X. Cao, C. Zhang, Q. Peng, C. Chen, Y. Li, *Chem. Soc. Rev.* **2020**, *49*, 2215−2264.

[37] C. Zhu, S. Fu, Q. Shi, D. Du, Y. Lin, *Angew. Chem. Int. Ed.* **2017**, *56*, 13944−13960.

[38] Y. Peng, B. Lu, S. Chen, *Adv. Mater.* **2018**, *30*, 1801995.

[39] S. Ding, M. J. Hülsey, J. Pérez-Ramírez, N. Yan, *Joule* **2019**, *3*, 2897−2929.

[40] W. Yang, T.-P. Fellinger, M. Antonietti, *J. Am. Chem. Soc.* **2011**, *133*, 206−209.

[41] R. Wu, J. Wang, K. Chen, S. Chen, J. X. Li, Q. Wang, Y. Nie, Y. Song, H. Chen, Z. Wei, *Electrochim. Acta* **2017**, *244*, 47−53.

[42] Á. García, T. Haynes, M. Retuerto, P. Ferrer, L. Pascual, M. A. Peña, M. Abdel Salam, M. Mokhtar, D. Gianolio, S. Rojas, *Ind. Eng. Chem. Res.* **2021**. DOI: org/10.1021/acs.iecr.1c02841

[43] M.-X. Chen, M. Zhu, M. Zuo, S.-Q. Chu, J. Zhang, Y. Wu, H.-W. Liang, X. Feng, *Angew. Chem. Int. Ed.* **2020**, *59*, 1627−1633.

[44] H. Jahnke, M. Schönborn, G. Zimmermann, *Top. Curr. Chem.* **1976**, *61*, 133−181.

[45] V. S. Bagotzky, M. R. Tarasevich, K. A. Radyushkina, O. A. Levina, S. I. Andrusyova, *J. Power Sources* **1978**, *2*, 233−240.

[46] J. Blomquist, H. Lång, R. Larsson, A. Widelöv, *J. Chem. Soc. Faraday Trans.* **1992**, *88*, 2007−2011.

[47] M. Kato, N. Fujibayashi, D. Abe, N. Matsubara, S. Yasuda, I. Yagi, *ACS Catal.* **2021**, *11*, 2356−2365.

[48] Z.-Y. Wu, M.-X. Chen, S.-Q. Chu, Y. Lin, H.-W. Liang, J. Zhang, S.-H. Yu, *iScience* **2019**, *15*, 282−290.

[49] D. Scherson, A. A. Tanaka, S. L. Gupta, D. Tryk, C. Fierro, R. Holze, E. B. Yeager, R. P. Lattimer, *Electrochim. Acta* **1986**, *31*, 1247−1258.

[50] P. Gouérec, M. Savy, J. Riga, *Electrochim. Acta* **1998**, *43*, 743−753.

[51] G. Lalande, G. Faubert, R. Côté, D. Guay, J. P. Dodelet, L. T. Weng, P. Bertrand, *J. Power Sources* **1996**, *61*, 227−237.

[52] F. Jaouen, S. Marcotte, J.-P. Dodelet, G. Lindbergh, *J. Phys. Chem. B* **2003**, *107*, 1376−1386.

[53] M. Lefèvre, J. P. Dodelet, P. Bertrand, *J. Phys. Chem. B* **2000**, *104*, 11238−11247.

[54] M. Lefèvre, J. P. Dodelet, P. Bertrand, *J. Phys. Chem. B* **2002**, *106*, 8705−8713.

[55] A. Zitolo, V. Goellner, V. Armel, M.-T. Sougrati, T. Mineva, L. Stievano, E. Fonda, F. Jaouen, *Nat. Mater.* **2015**, *14*, 937−942.

[56] A. Zitolo, N. Ranjbar-Sahraie, T. Mineva, J. Li, Q. Jia, S. Stamatin, G. F. Harrington, S. M. Lyth, P. Krtil, S. Mukerjee, E. Fonda, F. Jaouen, *Nat. Commun.* **2017**, *8*, 957.

[57] S. Gupta, D. Tryk, I. Bae, W. Aldred, E. Yeager, *J. Appl. Electrochem.* **1989**, *19*, 19−27.

[58] M. Lefèvre, E. Proietti, F. Jaouen, J.-P. Dodelet, *Science* **2009**, *324*, 71−74.

[59] G. Wu, K. L. More, C. M. Johnston, P. Zelenay, *Science* **2011**, *332*, 443−447.

[60] P. Yin, T. Yao, Y. Wu, L. Zheng, Y. Lin, W. Liu, H. Ju, J. Zhu, X. Hong, Z. Deng, G. Zhou, S. Wei, Y. Li, *Angew. Chem. Int. Ed.* **2016**, *55*, 10800−10805.

[61] Y. Chen, S. Ji, Y. Wang, J. Dong, W. Chen, Z. Li, R. Shen, L. Zheng, Z. Zhuang, D. Wang, Y. Li, *Angew. Chem. Int. Ed.* **2017**, *56*, 6937−6941.

[62] L. Jiao, H.-L. Jiang, *Chem* **2019**, *5*, 786−804.

[63] Z. Song, L. Zhang, K. Doyle-Davis, X. Fu, J.-L. Luo, X. Sun, *Adv. Energy Mater.* **2020**, *10*, 2001561.

[64] Y. Wang, J. Wang, D. Wei, M. Li, *ACS Appl. Mater. Interfaces* **2019**, *11*, 35755−35763.

[65] H. Zhang, H. T. Chung, D. A. Cullen, S. Wagner, U. I. Kramm, K. L. More, P. Zelenay, G. Wu, *Energy Environ. Sci.* **2019**, *12*, 2548−2558.

[66] J. Li, M. T. Sougrati, A. Zitolo, J. M. Ablett, I. C. Oğuz, T. Mineva, I. Matanovic, P. Atanassov, Y. Huang, I. Zenyuk, A. Di Cicco, K. Kumar, L. Dubau, F. Maillard, G. Dražić, F. Jaouen, *Nat. Catal.* **2021**, *4*, 10−19.

[67] K. S. Novoselov, A. K. Geim, S. V. Morozov, D. Jiang, Y. Zhang, S. V. Dubonos, I. V. Grigorieva, A. A. Firsov, *Science* **2004**, *306*, 666−669.

[68] F. Schwierz, *Nat. Nanotechnol.* **2010**, *5*, 487−496.

[69] J. Wu, W. Pisula, K. Müllen, *Chem. Rev.* **2007**, *107*, 718−747.

[70] X.-Y. Wang, X. Yao, K. Müllen, *Sci. China Chem.* **2019**, *62*, 1099−1144.

[71] S. Fujii, T. Enoki, *Acc. Chem. Res.* **2013**, *46*, 2202−2210.

[72] A. Narita, X.-Y. Wang, X. Feng, K. Müllen, *Chem. Soc. Rev.* **2015**, *44*, 6616−6643.

[73] R. S. Jassas, E. U. Mughal, A. Sadiq, R. I. Alsantali, M. M. Al-Rooqi, N. Naeem, Z. Moussa, S. A. Ahmed, *RSC Adv.* **2021**, *11*, 32158−32202.

[74] M. Müller, C. Kübel, K. Müllen, *Chem. Eur. J.* **1998**, *4*, 2099−2109.

[75] C. Kübel, K. Eckhardt, V. Enkelmann, G. Wegner, K. Müllen, *J. Mater. Chem.* **2000**, *10*, 879−886.

[76] S. M. Draper, D. J. Gregg, R. Madathil, *J. Am. Chem. Soc.* **2002**, *124*, 3486−3487.

[77] J. Cai, P. Ruffieux, R. Jaafar, M. Bieri, T. Braun, S. Blankenburg, M. Muoth, A. P. Seitsonen, M. Saleh, X. Feng, K. Müllen, R. Fasel, *Nature* **2010**, *466*, 470−473.

[78] Z. Chen, W. Zhang, C.-A. Palma, A. Lodi Rizzini, B. Liu, A. Abbas, N. Richter, L. Martini, X.-Y. Wang, N. Cavani, H. Lu, N. Mishra, C. Coletti, R. Berger, F. Klappenberger, M. Kläui, A. Candini, M. Affronte, C. Zhou, V. De Renzi, U. del Pennino, J. V. Barth, H. J. Räder, A. Narita, X. Feng, K. Müllen, *J. Am. Chem. Soc.* **2016**, *138*, 15488−15496.

[79] J. Cai, C. A. Pignedoli, L. Talirz, P. Ruffieux, H. Söde, L. Liang, V. Meunier, R. Berger, R. Li, X. Feng, K. Müllen, R. Fasel, *Nat*. *Nanotechnol*. **2014**, *9*, 896−900.

[80] X.-Y. Wang, X. Yao, A. Narita, K. Müllen, *Acc*. *Chem*. *Res*. **2019**, *52*, 2491−2505.

Chapter 1

Preparation of Fe/N/C Catalysts Using N-doped Graphene Nanoribbon Precursors for an Electrocatalytic Oxygen Reduction Reaction

Reproduced in part with permission from [*ACS Appl. Mater. Interfaces* **2021**, *13*, 15101−15112]
DOI: 10.1021/acsami.0c21321

1-1. Introduction

Polymer electrolyte fuel cells (PEFCs) are promising sustainable energy conversion devices requiring developments in electrode catalysts for electrochemical oxygen reduction reaction (ORR) which is a cathode reaction of PEFCs to improve the performance of PEFCs (Figure 1-1).[1,2] Platinum-based electrocatalysts exhibit the highest kinetic activity for four-electron ORR in the cathode of PEFCs.[3−5] However, the high cost and scarcity of platinum have limited widespread applications of platinum-based PEFCs. To replace platinum, non-precious metal-based catalysts have been extensively studied and a leading alternative to platinum-based catalysts is an Fe/N/C catalyst prepared by pyrolysis of precursors containing iron, nitrogen, and carbon.[6−10]

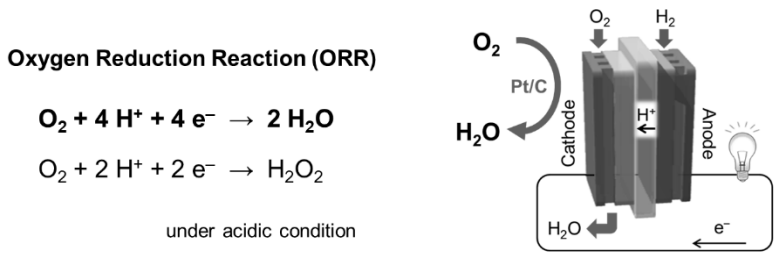

Figure 2-1. Schematic illustration of polymer electrolyte fuel cells with the reaction formulas of ORR.

For developing highly active Fe/N/C catalysts, precise construction and characterization of the active site structures are required. Nitrogen-containing organic compounds such as phenanthroline,[11] polypyrrole,[12] and polyaniline,[13] and others[14−18] have been employed as key precursors in construction of Fe–N_x active sites. Several studies using X-ray absorption spectroscopy, X-ray photoelectron spectroscopy and ^{57}Fe Mössbauer spectroscopy have unveiled the structures of the Fe–N_x active sites in the Fe/N/C catalysts. These structures include four nitrogen atoms embedded within the graphene layer or two nitrogen atoms on the edge of graphene coordinates to the iron ion (Figure 1-2a).[11,19−24] However, there have been some disagreements regarding these chemical structures due to their diversity and the different properties of the active sites of the materials,[25−28] and the difficulties in controlling the structure of the materials during the process of pyrolysis have been encountered. Therefore, further improvements in construction of precise Fe–N_x active sites embedded within the graphene layer have been required.

A variety of graphene nanomaterials with atomically precise structures have been prepared based on recent progress in development of bottom-up synthetic methods.[29] In the 1990's, Müllen and co-workers reported the successful preparation of defined polycyclic aromatic hydrocarbons (PAHs) through a solution-mediated approach based on a Diels-Alder cycloaddition followed by oxidation *via* the Scholl reaction.[30,31] This approach has been expanded from PAHs to graphene nanoribbons (GNRs), which are narrow strips of graphene.[32] Since the 2010's, surface-assisted methods for producing graphene nanomaterials have also been developed.[33] In these methods, the polymerization of the precursors and the cyclodehydrogenation are assisted by the metal surface upon thermal activation. These methods further enable introductions of heteroatoms such as nitrogen, oxygen, phosphorous, sulfur at precise positions in the GNRs.[34–37]

Inspired by both developments of the bottom-up synthesis of the graphene nanomaterials and previous findings of the advantages of using π-expanded aromatic compounds as precursors for the Fe/N/C catalysts reported by Hayashi and co-workers,[38,39] the author next envisioned thermally-controlled construction of a precise Fe–N_x structure along with the N-doped GNR (N-GNR) (Figure 1-2b). In this chapter, the author describes the fabrication, characterization, and electrocatalytic properties of a series of Fe/N/C catalysts prepared by pyrolysis of the N-GNR precursors in the presence of $FeCl_2$ and either carbon black or MgO as support materials. It was found that the precursors in which two nitrogen atoms coordinate to the iron ion at the edge of the N-GNRs greatly assisted the formation of the Fe–N_x active sites and significantly improved the catalytic activity for the ORR of the materials.

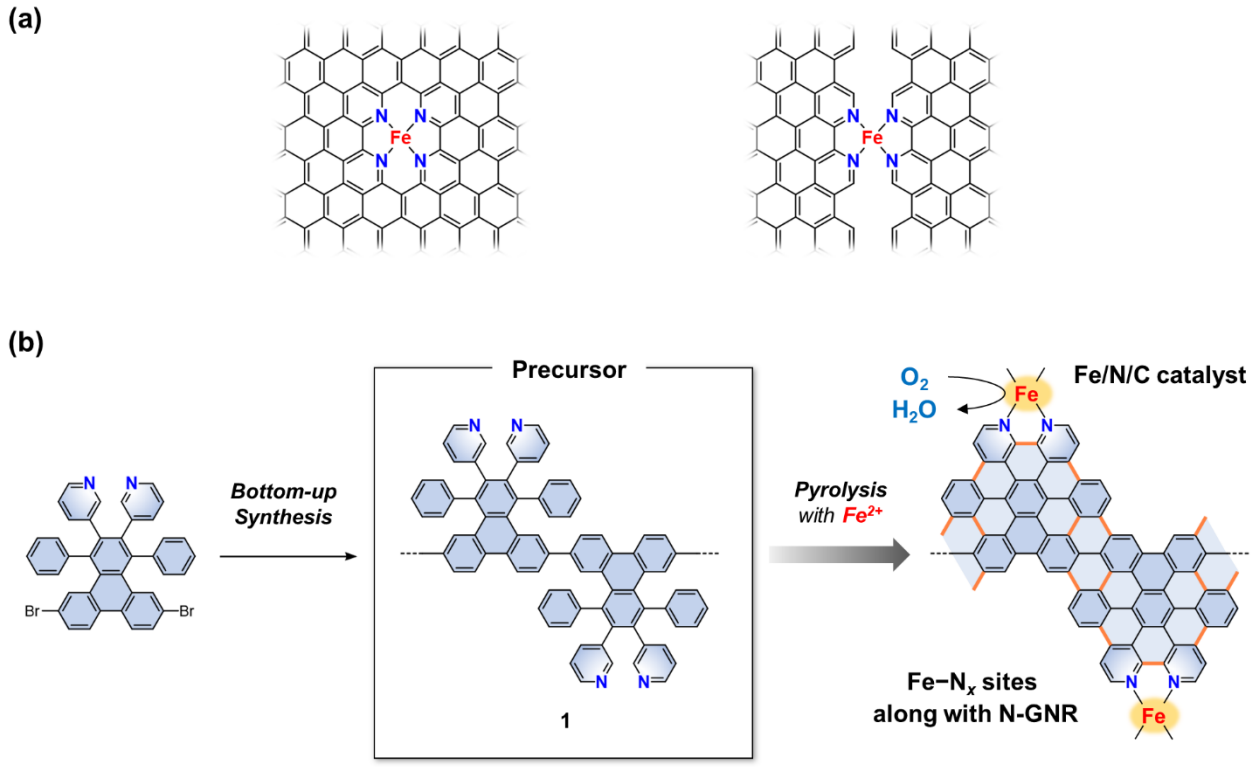

Figure 1-2. (a) Proposed active site structures of Fe/N/C catalysts. (b) Strategy for the construction of the Fe−N_x active sites in the Fe/N/C catalyst via a thermally controlled annulation reaction of the N-GNR precursor during pyrolysis.

1-2. Results and Discussion

Design and synthesis of precursors

The author designed aromatic polymers **1**−**4**, in which 1,2,3,4-tetraaryltriphenylene units are connected to each other at the 6 and 11 positions to fabricate Fe−N_x active sites along the N-GNR structure on the Fe/N/C catalysts (Figure 1-3). These polymer precursors have preorganized phenyl rings or nitrogen-containing aromatic rings at the adjacent positions of the unit structure. These structures would be efficiently converted into the GNR structures through intramolecular annulation reaction between preorganized aromatic rings during pyrolysis. Precursors **1** and **2** contain two 3-pyridyl and 3-quinolyl groups, respectively, at the 2 and 3 positions of the triphenylene core. Both precursors **1** and **2** are expected to form an N2 site, in which two nitrogen atoms coordinate to the iron ion, after annulation, as shown in Figure 1-2b. Precursor **3** containing two 4-pyridyl groups at the 2 and 3 positions, which does not form the N2 site, was prepared to evaluate the influence of the position of the nitrogen atoms on the GNR precursor. Furthermore, precursor **4** without nitrogen atoms was used as a reference. Polymer precursors **1**−**4** were synthesized from compound **9** and the corresponding alkyne compounds via the Diels−Alder reaction, followed by Yamamoto polymerization using bis(1,5-cyclooctadiene)nickel(0), $Ni(COD)_2$, as a catalyst (Scheme 1-1).[34,40] The polymerization was confirmed by matrix-assisted laser desorption ionization time-of-flight (MALDI-TOF) mass spectrometry (Figure 1-4). The corresponding monomeric precursors **5**−**8** were also synthesized as reference compounds (Figure 1-3). These monomer precursors are expected to be converted into the corresponding hexa-*peri*-hexabenzocoronene-type compounds by the pyrolytic treatment.

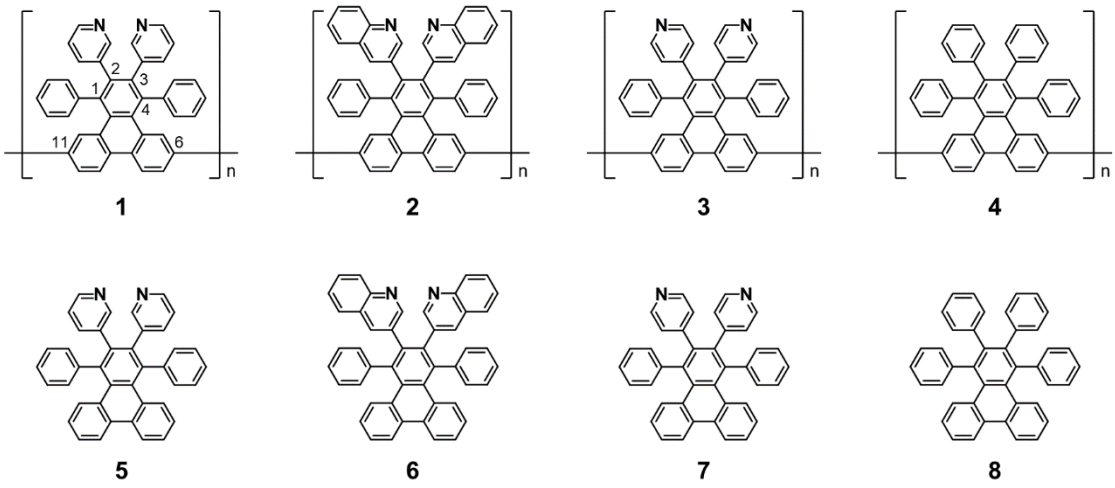

Figure 1-3. Chemical structures of precursors **1**−**8**.

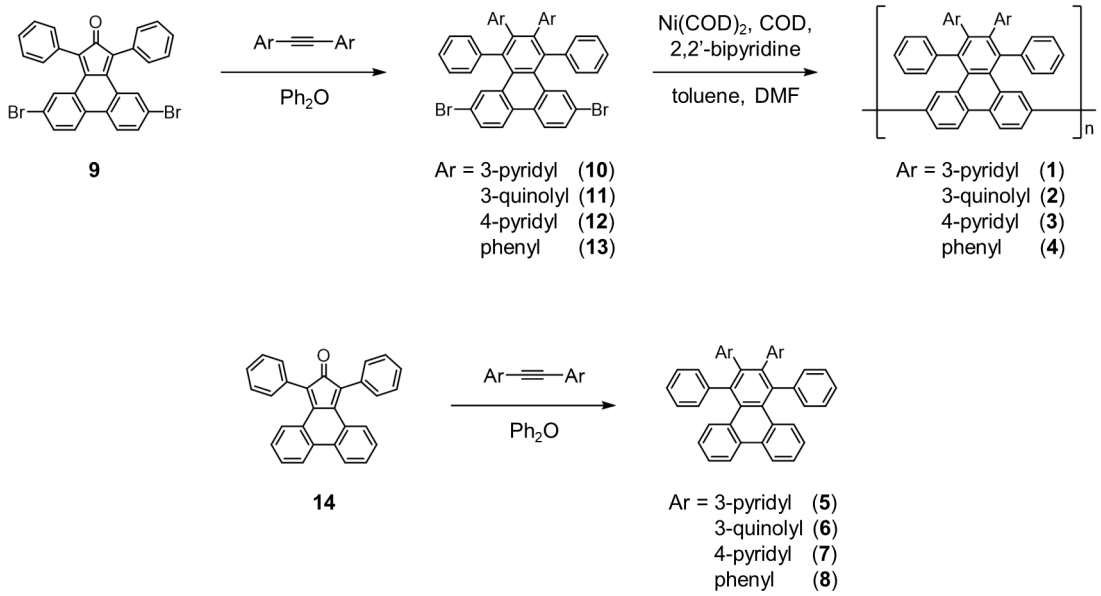

Scheme 1-1. Synthesis of precursors **1**−**8**.

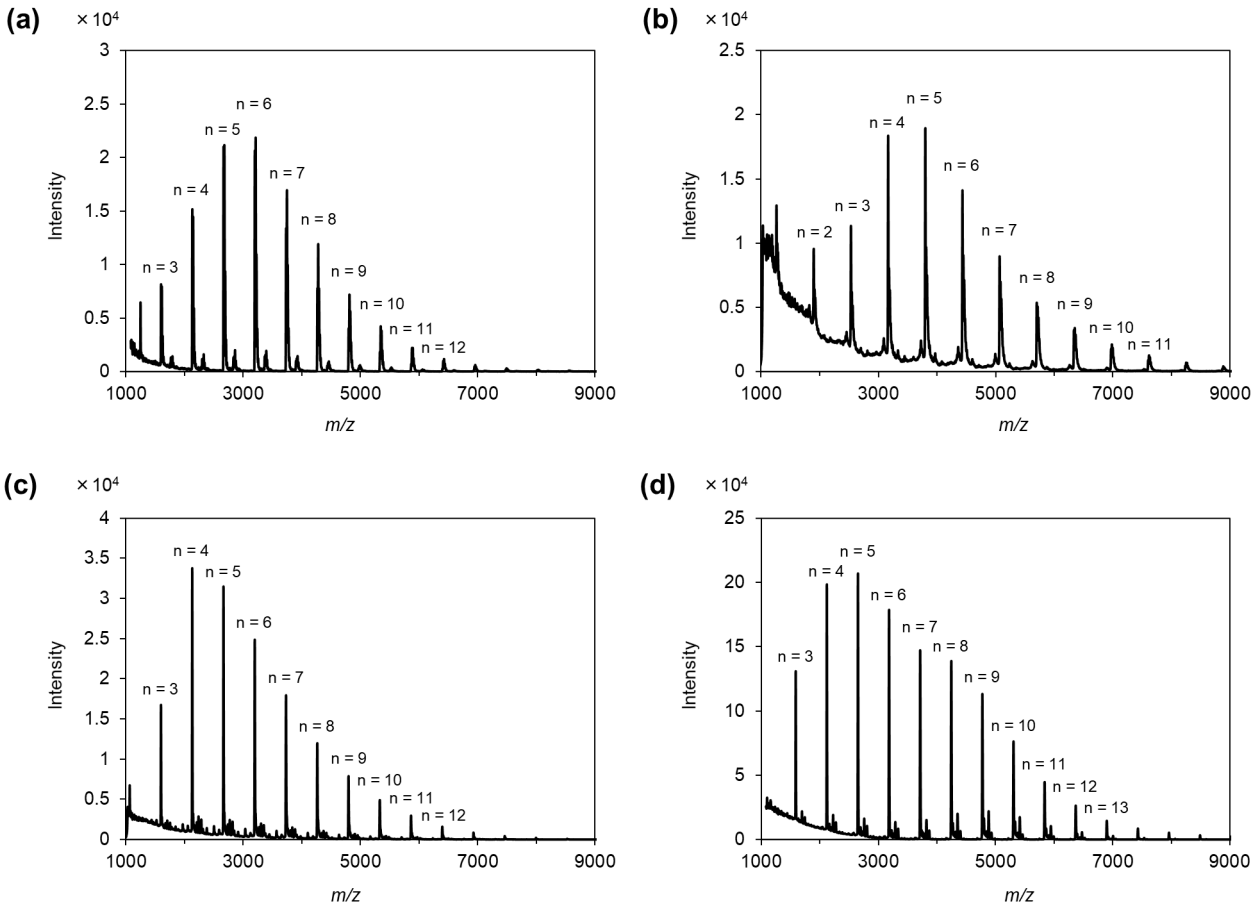

Figure 1-4. MALDI-TOF MS of polymerized precursors (a) **1**, (b) **2**, (c) **3**, and (d) **4**.

The thermal stabilities of the precursors were evaluated by the loss of mass of the precursors during pyrolysis under N_2 flow, which were determined by thermogravimetric analysis (TGA) (Figure 1-5). The thermal decomposition temperature (T_D) values of the polymerized compounds **1**–**4** are 545 °C, 530 °C, 550 °C, and 560 °C, respectively. These values are approximately 200 °C higher than those of the corresponding monomer compounds **5** (355 °C), **6** (370 °C), **7** (340 °C), and **8** (315 °C). The monomer precursors would be thermally decomposed or sublimed at these temperatures. Importantly, the weight loss values of **1**–**4** at 900 °C are within the range between 14% and 20% (Table 1-1). When the polymer precursors were converted to the GNR structure via the intramolecular annulation reaction, the value of weight loss was calculated to be about 2.6%. Although the experimental loss of the weight according to the TGA curves is higher than the calculated value, more than 80% of precursors **1**–**4** are converted to the thermally stable structure and the compositions of the precursors remain after pyrolysis.

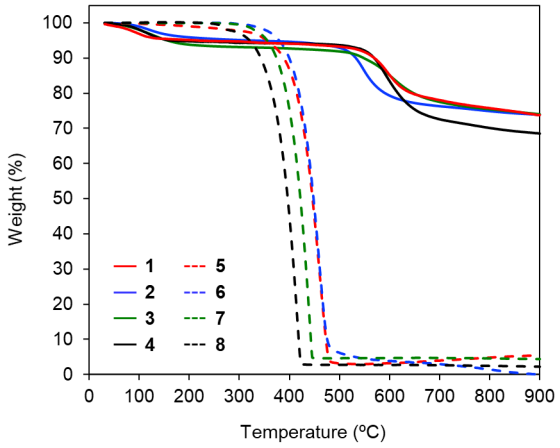

Figure 1-5. Thermal gravimetric analysis curves of precursors **1** (red solid line), **2** (blue solid line), **3** (green solid line), **4** (black solid line), **5** (red dashed line), **6** (blue dashed line), **7** (green dashed line), and **8** (black dashed line).

Table 1-1. Results of TG Measurements.

Precursor	T_D[a] (ºC)	Weight loss[b] (%)
1	545	16
2	530	17
3	550	14
4	560	20
5	355	92
6	370	93
7	340	94
8	315	96

[a]Thermal decomposition temperature values. [b]Weight loss values near the decomposition temperature.

Preparation of the Fe/N/C catalysts

The Fe/N/C electrocatalysts were prepared from the precursors using two methods A and B (Figure 1-6), respectively. In method A, precursor **1**–**8**, the iron salts, and carbon black (Vulcan® XC72R, VC) were vigorously mixed and the resulting row materials were pyrolyzed at 1000 ºC for 2 h under N_2 flow.[38,39] Then, Fe/**1**@VC, Fe/**2**@VC, Fe/**3**@VC, Fe/**4**@VC, Fe/**5**@VC, Fe/**6**@VC, Fe/**7**@VC, or Fe/**8**@VC was obtained. Although the TGA curves indicate that the monomers **5**–**8** are thermally decomposed or sublimed over 400 °C, these precursors can form the active sites and be remained when they are pyrolyzed in the presence of VC.

In method B, precursor **1**, the iron salts, and MgO particles (ϕ = 50 nm), which are used as a sacrificial template, were combined and the mixture was pyrolyzed.[41] The pyrolysis temperature was set to 500 °C, 600 °C, 700 °C, 800 °C, 900 °C or 1000 °C, respectively. Then, the acid washing was conducted to remove MgO template and inactive iron impurities generated by the aggregation of iron atoms. After washing with a deionized water and drying, Fe/**1**@MgO[500 °C], Fe/**1**@MgO[600 °C], Fe/**1**@MgO[700 °C], Fe/**1**@MgO [800 °C], Fe/**1**@MgO[900 °C], and Fe/**1**@MgO[1000 °C] were obtained. The Fe/N/C catalysts prepared by method B contain only the component derived from the precursors. This method therefore enables precise characterization of the chemical structure and the composition of the pyrolyzed precursors.

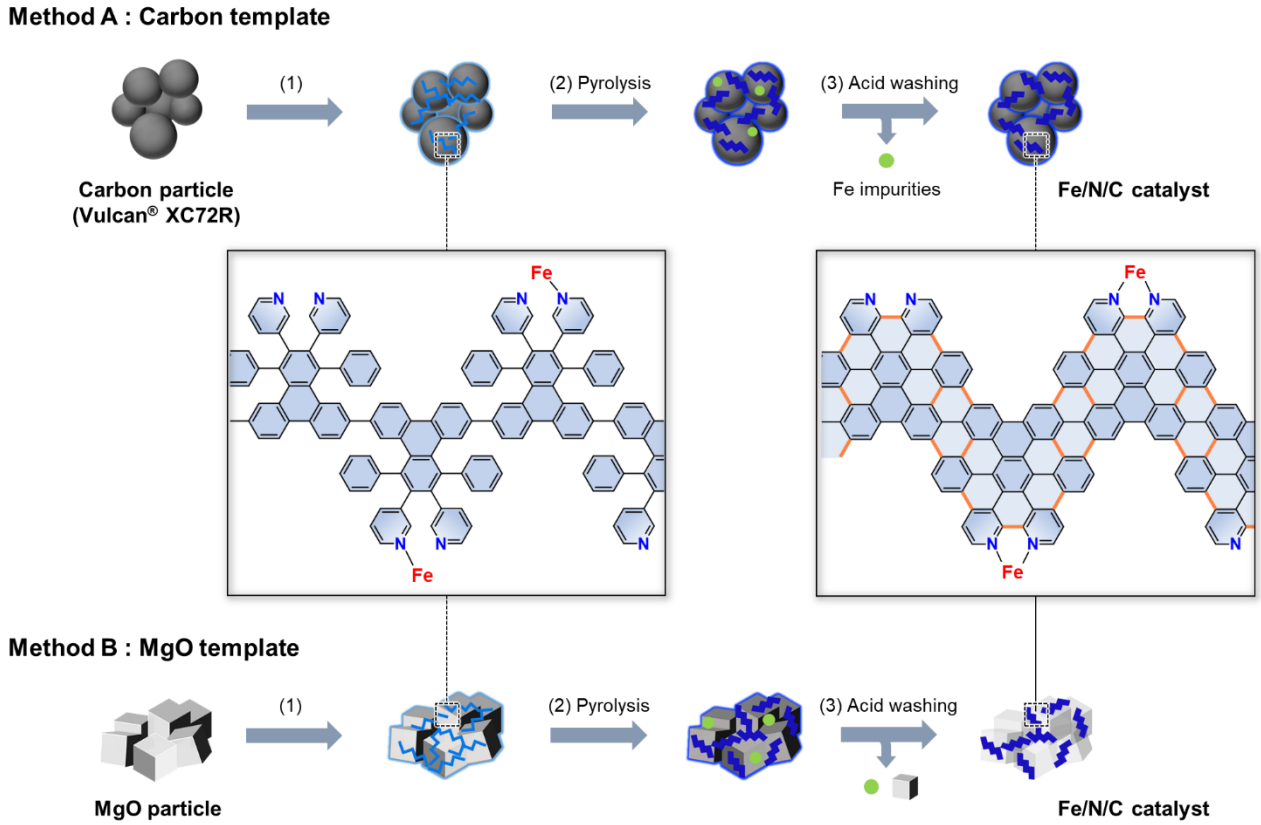

Figure 1-6. Schematic illustration of the methods for preparation of Fe/N/C catalysts. (1) The precursor (light blue zigzag line) and iron ion are mixed with carbon particles (method A) or MgO particles (method B), (2) pyrolysis under N_2 flow, and (3) acid washing to remove iron impurities (light green circle) and MgO particles in method B.

Electrocatalytic activities for oxygen reduction reaction (ORR)

Rotating ring-disk electrode (RRDE) measurements were performed to determine the ORR activities of the Fe/N/C catalysts prepared by method A (Figure 1-7). Fe/**1**@VC shows the highest performance for ORR activity in the catalysts with an onset potential of 0.88 V vs. reversible hydrogen electrode (RHE), determined for $j = -0.05$ mA·cm^{-2}. Fe/**2**@VC also exhibits significantly positive-shifted onset potential (0.86 V vs. RHE) for O_2 reduction compared to that of Fe/**3**@VC (0.81 V vs. RHE). Fe/**4**@VC shows much lower activity (0.61 V vs. RHE). These results indicate that nitrogen-containing moieties in the GNR structures are essential to improve the ORR activity and that the position of the nitrogen atoms in the precursors strongly affects the activity of the Fe/N/C catalysts. A similar trend is found in the case of the catalysts prepared from monomer precursors **5**–**8**. However, the onset potentials of the catalysts prepared from the monomer precursors negatively shift compared to those of the catalysts prepared from the corresponding polymer precursors **1**–**4**. RRDE measurements were also performed to quantify hydrogen peroxide (H_2O_2) as a byproduct during ORR. The percentage of H_2O_2 during O_2 reduction were calculated from the RRDE for each catalyst. Fe/**1**@VC and Fe/**2**@VC generated less than 10% H_2O_2 in the range from 0.0 to 0.7 V vs. RHE. Finally, it is worth mentioning that the catalytic activities for the ORR of Fe/**1**@VC and Fe/**2**@VC are always superior to those of the other catalysts in terms of the onset potential. These results indicate that the structure of the N-GNR precursor is quite important for the performance of the Fe/N/C catalysts.

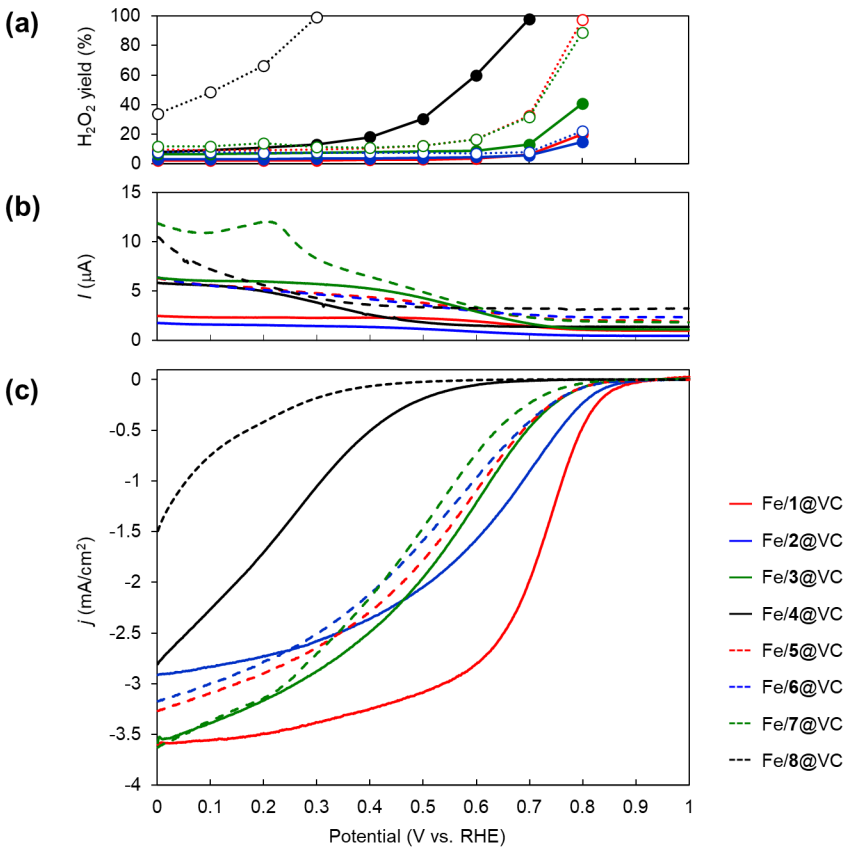

Figure 1-7. (a) H_2O_2 yield, (b) ring current and (c) disk current density of the catalysts. The linear sweep voltammograms were recorded during positive sweep with 5 mV·s^{-1} at 2000 rpm in an O_2 saturated 0.1 M $HClO_{4aq}$ solution.

In addition, the mass-based site density (MSD), defined as the number of redox-active Fe–N_x sites per unit mass of the catalyst, and the turnover frequency (TOF), which represents the number of electrons transferred per an active site and per a second, were calculated using the results of cyclic voltammetry (CV) measurements in a N_2-purged electrolyte (Figure 1-8) and linear sweep voltammetry in an O_2-saturated electrolyte (Figure 1-7c).[20,42] These values of the catalysts are listed in Table 1-2. The MSD values of Fe/**1**@VC (5.4×10^{19} sites·g_{cat}^{-1}) and Fe/**2**@VC (3.3×10^{19} sites·g_{cat}^{-1}) are significantly greater than those of the other catalysts. Furthermore, Fe/**1**@VC and Fe/**2**@VC exhibit higher TOF values (0.14 e·site^{-1}·s^{-1}, 0.12 e·site^{-1}·s^{-1}, respectively) relative to the other catalysts. These results support the fact that the highly active Fe–N_x sites are effectively produced from precursors **1** and **2**.

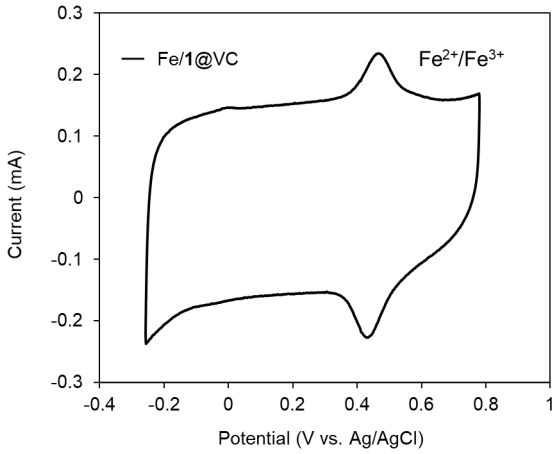

Figure 1-8. CV curve of Fe/**1**@VC in an N_2-saturated 0.1 M $HClO_{4aq}$ solution at 50 mV·s^{-1} at 2000 rpm from −0.258 to 0.742 V vs. Ag/AgCl. Catalyst loading: 0.41 mg_{cat}·cm^{-2}.

Table 1-2. Summary of MSD and TOF Values.

Fe/N/C catalysts	MSD[a] (10^{19}·sites·g_{cat}^{-1})	TOF $_{at\ 0.8\ V}$[b] (10^{-2}·e·site^{-1}·s^{-1})
Fe/**1**@VC	5.4	14
Fe/**2**@VC	3.3	12
Fe/**3**@VC	1.0	6.3
Fe/**5**@VC	2.8	1.9
Fe/**6**@VC	2.4	4.4
Fe/**7**@VC	1.4	4.2

[a]Mass-based site density. [b]Turnover frequency at 0.8 V vs. RHE.

Characterizations of the Fe/N/C catalysts

The morphology of Fe/**1**@VC−Fe/**5**@VC prepared by method A was investigated by transmission electron microscopy (TEM) (Figure 1-9) and scanning electron microscopy (SEM) with energy dispersive X-ray (EDX) mapping analysis (Figures 1-10). These catalysts have spherical structures with diameters of 40−70 nm, which retain the inherent nanostructure of VC (Figure 1-9a). Interestingly, metal or metal oxide nanoparticles do not exist in the TEM image of Fe/**1**@VC, suggesting that iron is highly dispersed within the carbon materials (Figure 1-9b). Although iron nanoparticles with a diameter of ca. 1 nm were observed on the surface of Fe/**2**@VC, their numbers are quite limited (Figure 1-9c). In contrast, large particles were clearly observed in Fe/**3**@VC and Fe/**4**@VC (Figures 1-9d and e). These results indicate that the Fe-coordinating N2 structures along the GNR framework in the catalysts, Fe/**1**@VC and Fe/**2**@VC, contribute to the tight binding of the iron ions during pyrolysis and suppression of generating larger iron nanoparticles via sintering. As a result, the iron species can be highly dispersed in Fe/**1**@VC and Fe/**2**@VC. In the case of Fe/**5**@VC prepared from monomer precursor **5** with the Fe-coordinating N2 structure, small nanoparticles are found (Figure 1-9f), suggesting that the N2 site constructed along the GNR structure of polymer precursor **1** is more effective at dispersing the iron species within the carbon support compared to the precursor with the N2 site in monomer precursor **5**. This can be explained by the lower thermal stability of monomer precursor **5**, which sublimes at temperatures above 400 °C. The existence and dispersity of the iron species in each catalyst were also confirmed by SEM-EDX mapping analysis (Figure 1-10).

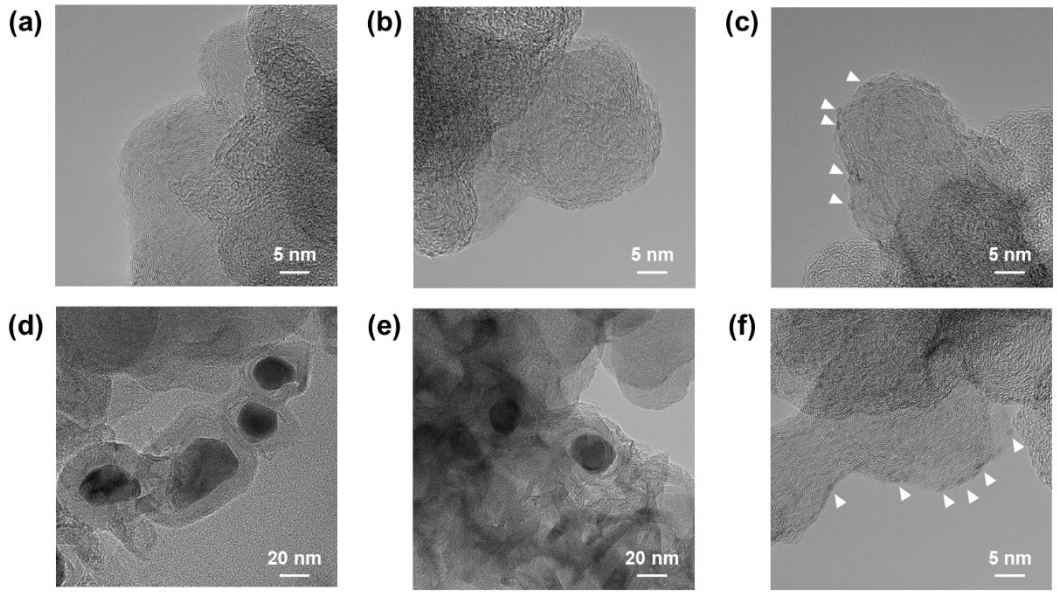

Figure 1-9. TEM images of (a) VC, (b) Fe/**1**@VC, (c) Fe/**2**@VC, (d) Fe/**3**@VC, (e) Fe/**4**@VC, and (f) Fe/**5**@VC. The small aggregates are highlighted by white triangles.

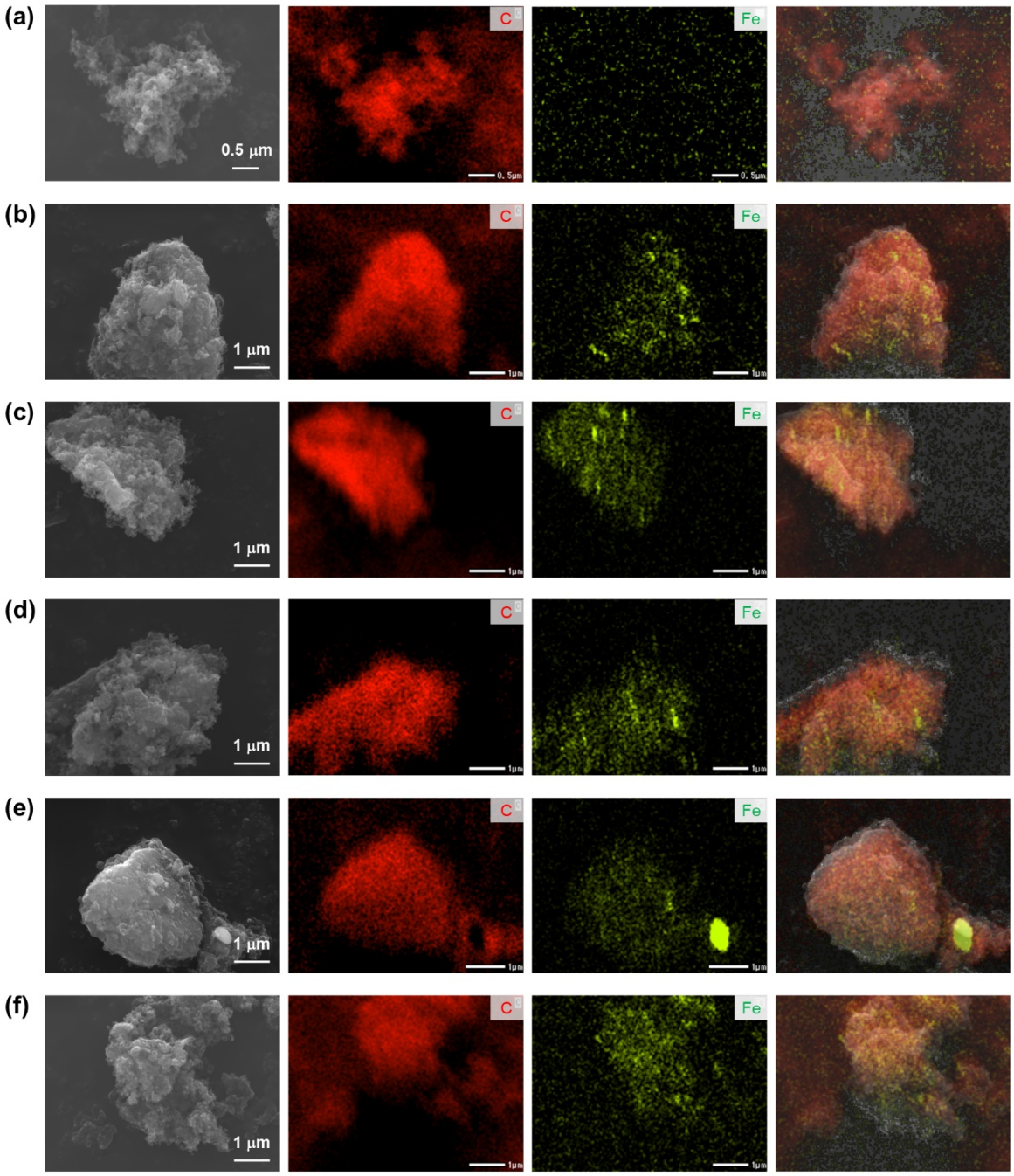

Figure 1-10. SEM images, EDX element mapping images of carbon (red) and iron (light green), and overlaid SEM images of (a) VC, (b) Fe/**1**@VC, (c) Fe/**2**@VC, (d) Fe/**3**@VC, (e) Fe/**4**@VC, and (f) Fe/**5**@VC.

Powder X-ray diffraction

The formation of the iron particles as byproducts was confirmed by powder X-ray diffraction (powder-XRD) measurements (Figure 1-11). All the catalysts exhibit broad diffraction peaks at 2 θ = ca. 26.0 and 44.0º, which are assigned to the carbonaceous structures. The observed sharp peaks at 2 θ = 43.5 and 44.5º indicate the existence of iron carbides (Fe_3C) and bulk Fe, respectively. Such iron particles are not detected in Fe/**1**@VC, although the other catalysts (Fe/**2**@VC−Fe/**8**@VC) contain the Fe_3C or bulk Fe. These results are in good accordance with the TEM measurements (Figure 1-9).

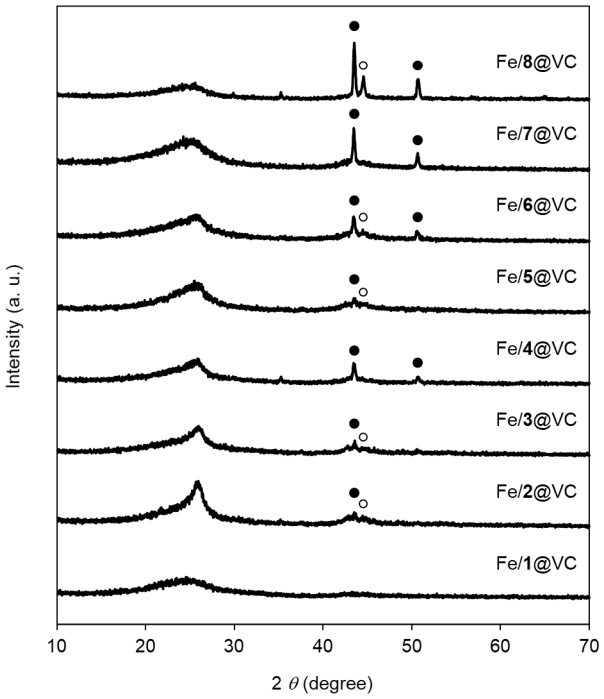

Figure 1-11. XRD patterns of the catalysts. The XRD peaks of Fe_3C (JCPDS 00-034-0001) and bulk Fe (JCPDS 00-006-0696) are marked by filled circles and open circles, respectively.

Fe K-edge X-ray absorption spectroscopy

The electronic states and environments around iron atoms in Fe/**1**@VC and Fe/**5**@VC were analyzed by Fe K-edge X-ray absorption spectroscopy (XAS) (Figure 1-12). The X-ray absorption near edge structure (XANES) spectra of the catalysts were compared with those of the reference samples; FeO, Fe_2O_3 and Fe-foil (Figure 1-12a). The pre-edge and absorption edge features of Fe/**1**@VC and Fe/**5**@VC clearly do not match those of FeO, Fe_2O_3, and Fe-foil, indicating that the electronic states of the iron species in the carbon catalysts are different from those of the standard inorganic iron materials.[25,43]

Next, the local environments around the iron atoms in Fe/**1**@VC and Fe/**5**@VC were evaluated by Fourier-transformed extended X-ray absorption fine structure (FT-EXAFS) analysis (Figure 1-12b). According to the FT-EXAFS spectrum of Fe-foil, the Fe–Fe distances in the first and second coordination shells were determined to be ca. 2.6 and 4.9 Å with the phase correction, respectively. In addition, the Fe–N distance was determined to be ca. 2.1 Å with the phase correction by referring the FT-EXAFS spectrum of Fe-tetraphenylporphyrin chloride complex (FeTPPCl). The two distinct strong peaks are observed in the spectrum of Fe/**1**@VC. One of the strong peaks can be assigned to be the Fe–N bond length (2.1 Å),[44] suggesting that Fe/**1**@VC clearly contains Fe–N_x structures. Another strong peak is assigned to the Fe–Fe bond length (2.6 Å) of the iron aggregates. This short Fe–Fe distance corresponds to the distance of the first coordination shell in the iron particles, indicating that the iron particles in Fe/**1**@VC are quite small and consist of a minimum number of the iron atoms providing the first coordination shell. In the FT-EXAFS spectrum of Fe/**5**@VC, strong two peaks and a small shoulder, which correspond to the Fe–Fe and Fe–N distances, respectively, were observed. This result suggests that Fe/**5**@VC contains iron aggregates and a small portion of the Fe–N_x structure. These EXAFS results support the fact that the polymer precursor **1** more efficiently generates the appropriate Fe–N_x structure than corresponding monomer precursor **5**.

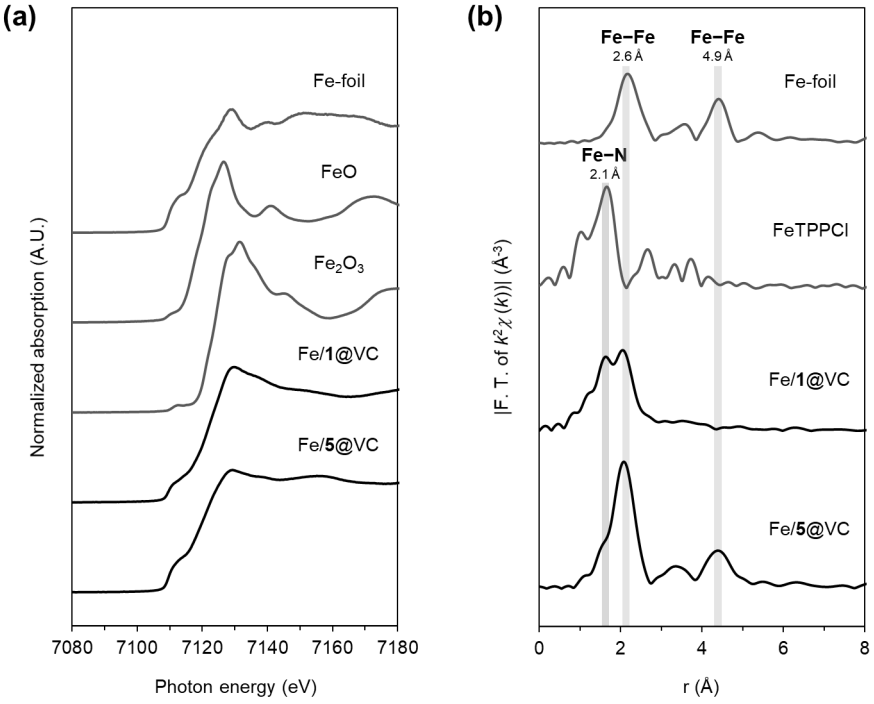

Figure 1-12. (a) Normalized Fe K-edge XANES spectra of Fe/**1**@VC, Fe/ **5**@VC, and reference samples: Fe foil, FeO, and Fe_2O_3. (b) Fourier transformed EXAFS spectroscopy oscillations of Fe/**1**@VC, Fe/ **5**@VC, and reference samples: Fe foil and Fe-tetraphenylporphyrin chloride complex (FeTPPCl). The Fe−Fe distances of Fe-foil and the Fe−N distance of FeTPPCl are highlighted. The Fe−Fe distances in the first and second coordination shells with the phase correction (ca. 2.6 and 4.9 Å) and the Fe−N distance with the phase correction (ca. 2.1 Å) are indicated on the top of the peaks.

X-ray photoelectron spectroscopy

X-ray photoelectron spectroscopy (XPS) measurements were carried out to identify the chemical bonding state of the nitrogen atoms in the Fe/N/C catalysts (Figure 1-13). The XPS N1s spectra were fitted with peaks assigned to four nitrogen species including pyridinic *N*, Fe–*N*, graphitic *N*, and *N*-oxide (Figure 1-13a).[45,46] The relative ratios of each nitrogen species are summarized in the bar graph (Figure 1-13b). Importantly, the relative ratios of Fe–*N* species consisting of the Fe–N_x structures are higher in Fe/**1**@VC (33.4%) and Fe/**2**@VC (28.7%) than the ratio determined for Fe/**3**@VC (23.9%). These data suggest that precursors **1** and **2** with two Fe-coordinating nitrogen atoms are advantageous for generating the Fe–N_x structures. In addition, the relative ratios of the Fe–*N* species in Fe/**5**@VC, Fe/**6**@VC, and Fe/**7**@VC are 21.0, 24.7, and 18.3, respectively. These values are smaller than those of Fe/**1**@VC–Fe/ **3**@VC, which are prepared from the corresponding polymer precursors. Taken together, polymer precursors **1** and **2** forming the N2 site coordinating to an iron atom during pyrolysis are preferable for the construction of the Fe–N_x active sites.

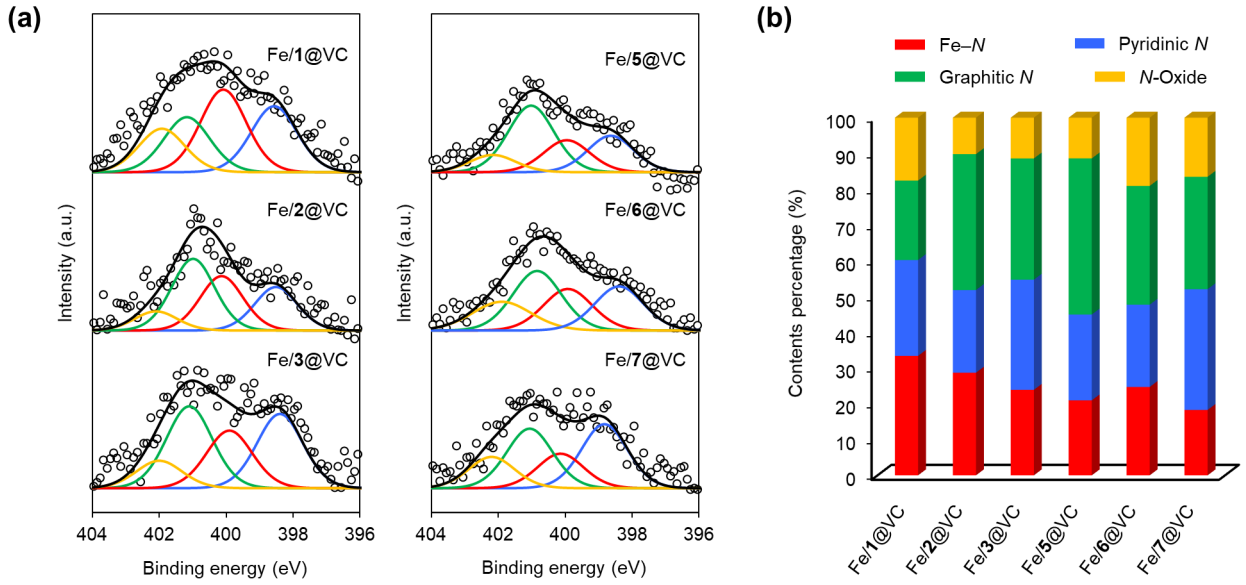

Figure 1-13. (a) XPS N1s spectra of Fe/**1**@VC–Fe/**3**@VC and Fe/**5**@VC–Fe/**7**@VC with the simulated peaks of Fe–*N* (red), pyridinic *N* (blue), graphitic *N* (green), and *N*-oxide (yellow). (b) Relative ratios of the four nitrogen species.

Characterizations and ORR activity of materials prepared by method B

To further analyze the formation process of the Fe–N_x structure from polymer precursor **1**, the Fe/N/C catalysts (Fe/**1**@MgO[X ºC], X = 500, 600, 700, 800, 900, and 1000) were also prepared by method B (Figure 1-6) at different pyrolysis temperatures in the range of 500–1000 °C. Since method B does not use additional carbon materials, the transformation of the chemical structure of the precursors can be clearly characterized. The chemical structures of the catalysts prepared at the different temperatures were analyzed by Raman spectroscopy, XPS, and elemental analysis, and their electrocatalytic activity toward ORR were evaluated.

The carbon catalysts, Fe/**1**@MgO, prepared by pyrolysis at 500−1000 °C were analyzed by Raman spectroscopy (Figure 1-14a). A sharp peak at 1600 cm^{-1} and a broad peak at around 1200−1400 cm^{-1} are found in the Raman spectra of Fe/**1**@MgO[500 °C] and Fe/**1**@MgO[600 °C]. These peaks are assigned to the stretching vibration of C=C double bonds and a breathing vibration of phenyl rings, respectively, suggesting the formation of GNR-like structure.[40,47,48] In contrast, the spectra of the precursors pyrolyzed at higher temperatures (> 700 °C) present typical D (disorder) and G (graphite) bands at 1350 and 1580 cm^{-1}, respectively,[49,50] indicating that precursor **1** is converted into the graphitized materials at temperatures above 700 °C.

To follow the formation of the Fe−N_x structure after pyrolysis, XPS analyses were performed (Figures 1-14b and c). A strong peak of pyridinic *N* at 398.5 eV was observed in the mixture of the iron ion and precursor **1** before pyrolysis. The peak intensity of Fe−*N* at 399.8 eV increases as the pyrolysis temperature raises while the peak intensity of pyridinic *N* decreases. This suggests that the pyridinic *N* species is converted into Fe−*N* and forms the Fe−N_x structures during pyrolysis. The ratio of Fe−*N* species reaches a maximum (43.4%) at 800 °C. The contents of other nitrogen species such as graphitic *N* and *N*-oxides increase at temperatures above 500 °C.

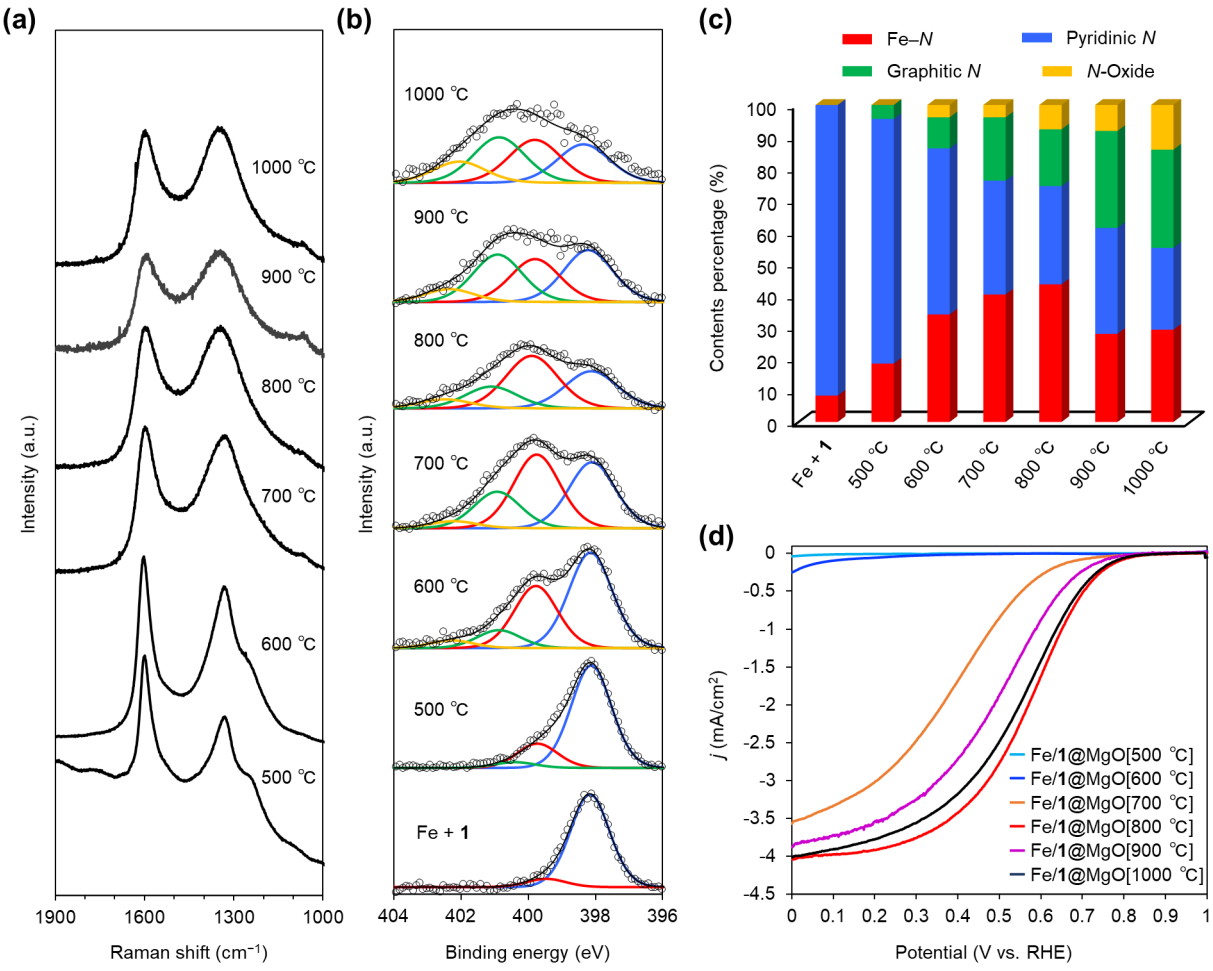

Figure 1-14. Characterizations and ORR activities of the Fe/N/C catalysts prepared by method B at 500, 600, 700, 800, 900, and 1000 °C. (a) Raman spectra, (b) XPS N1s spectra with simulated peaks of Fe−*N* (red), pyridinic *N* (blue), graphitic *N* (green), and *N*-oxide (yellow), (c) relative ratios of the four nitrogen species, and (d) ORR polarization curves.

The ORR activity of the Fe/N/C catalysts prepared using MgO at different temperatures was investigated by rotating disk electrode (RDE) measurements (Figure 1-14d). Fe/**1**@MgO[500 °C] and Fe/**1**@MgO[600 °C] do not exhibit any catalytic currents in ORR. Fe/**1**@MgO[700 °C] shows a moderate ORR activity (E_{onset} = 0.73 V vs. RHE) and that of Fe/**1**@MgO[800 °C] is the most positive (E_{onset} = 0.82 V vs. RHE). The onset potentials of Fe/**1**@ MgO[900 °C] and Fe/**1**@MgO[1000 °C] are shifted slightly negative relative to that of Fe/**1**@MgO[800 °C].

The atom ratios of hydrogen atoms per carbon atoms (H/C) at various pyrolysis temperatures are determined from the results of elemental analysis (Figure 1-15a). The decrease in the H/C values supports the fact that the graphitization process proceeds through an oxidative coupling reaction with a loss of hydrogen atoms. The H/C value decreases significantly until the pyrolysis temperature is reached to 700 °C. In contrast, the H/C value decreases gradually at temperatures above 700 °C. These results are in good accordance with the spectral changes observed in the Raman measurements (Figure 1-15a).

The absolute amounts of the nitrogen species, Fe−*N*, pyridinic *N*, graphitic *N*, and *N*-oxide, in the precursor pyrolyzed at 500−1000 °C were also determined from the results of the elemental analysis and the XPS N1s analysis (Figure 1-15a). These regions are discernible for the decrease in the relative amount of the pyridinic *N* species; below 700 °C, the amounts of pyridinic *N* decrease rapidly, and above 700 °C, a slower decrease of the content of pyridinic *N* is observed. This trend correlates with the changes in the H/C values. Furthermore, the amounts of Fe−*N* species increase concomitantly up to 700 °C and slightly more up to 800 °C. Therefore, the Fe−N_x structures are mainly formed together with generation of the GNR structures up to 800 °C. It was observed that further increasing the pyrolysis temperature results in the decomposition of the Fe−N_x structure with the formation of graphitic *N* and *N*-oxide species.

The relation between the onset potentials for ORR and the pyrolysis temperature is shown in Figure 1-15b. The ORR activities of the catalysts prepared at different pyrolysis temperatures are clearly correlated with the graphitization process of precursor **1** and the generation of the Fe−N_x active sites. Based on these results, the author proposed that the highly active Fe−N_x sites for ORR were efficiently constructed via intramolecular annulation and further graphitization of N-doped graphene nanoribbon precursor **1**. Within the temperature range of 800−1000 °C, the onset potentials are similar, although the number of Fe−N_x active sites decreases. This result may be explained by the fact that the improved conductivity provided by the graphitization of the precursors compensates for the loss of the active sites. The data of the characterizations and the evaluation of ORR activities of the catalysts prepared in this work are summarized in Table 1-3.

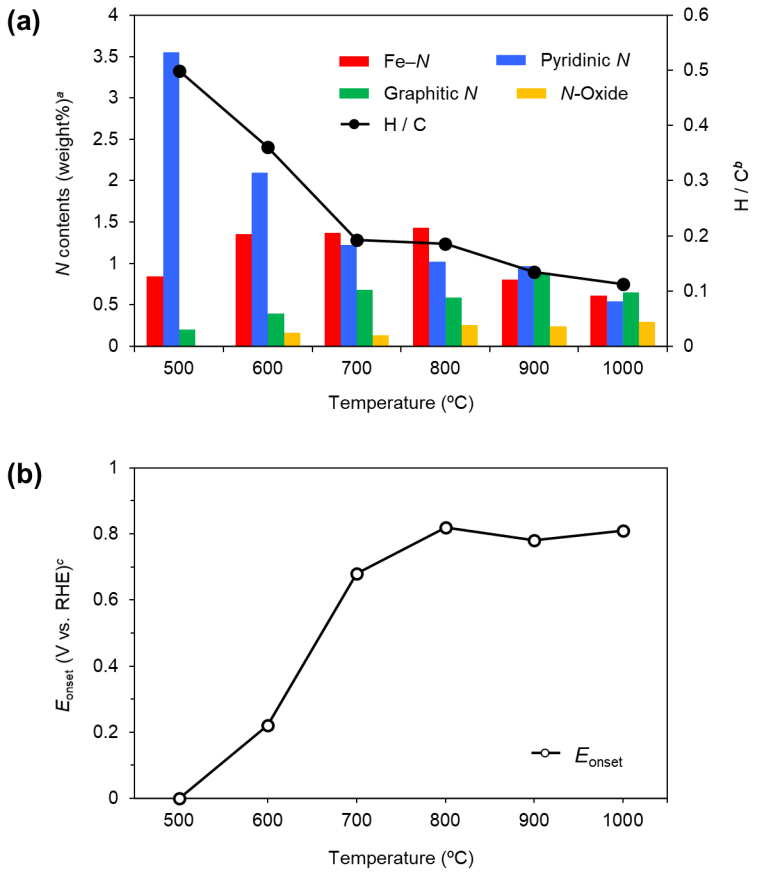

Figure 1-15. Temperature dependency of (a) the ratios of hydrogen vs. carbon (line graph), the contents of nitrogen species (bar graph) and the E_{onset} values of Fe/**1**@MgO for ORR. [a]The content of each *N* species was calculated from the elemental analysis and XPS data. [b]H/C values were calculated based on the results of elemental analysis. [c]The values of E_{onset} were estimated using RDE during positive sweep with 5 $mV \cdot s^{-1}$ at 2000 rpm in an O_2 saturated 0.1 M $HClO_{4aq}$ solution.

Table 1-3. Summary of Characterizations and ORR Activity of the Catalysts.

Catalyst	Elemental analysis				XPS (N1s)					E_{onset}[c]
	Fe[a]	N	C	H	Fe−*N*		Pyridinic-*N*	Graphitic- *N*	*N*-oxide	
	wt%	wt%	wt%	wt%	wt%[b]	%	%	%	%	V vs. RHE
Fe/**1**@VC	1.3	0.7	86.0	0.2	0.24	33.4	26.8	22.2	17.7	0.88
Fe/**2**@VC	1.1	0.5	90.4	0	0.14	28.7	23.1	38.0	10.2	0.86
Fe/**3**@VC	1.3	0.4	89.4	0	0.10	23.9	30.8	33.9	11.5	0.81
Fe/**4**@VC	1.0	0.2	88.8	0	–	–	–	–	–	0.61
Fe/**5**@VC	1.0	0.9	87.0	0.2	0.19	21.0	24.0	43.6	11.4	0.81
Fe/**6**@VC	1.0	0.9	89.3	0.4	0.22	24.7	23.0	33.2	19.1	0.80
Fe/**7**@VC	1.2	0.5	84.9	0.8	0.09	18.3	33.8	31.4	16.5	0.74
Fe/**8**@VC	1.5	0.2	83.6	0.6	–	–	–	–	–	0.38
Fe/**1**@MgO[X °C]										
X = 500	0.6	4.6	79.0	3.3	0.85	18.4	77.2	4.4	0	–
X = 600	0.6	4.0	77.0	2.3	1.36	33.9	52.4	9.8	4.0	0.20
X = 700	0.6	3.4	73.1	1.2	1.37	40.2	35.9	20.0	3.9	0.64
X = 800	0.7	3.3	73.6	1.2	1.43	43.4	31.0	17.9	7.7	0.82
X = 900	0.7	2.9	72.0	0.8	0.80	27.8	33.4	30.6	8.2	0.78
X = 1000	1.5	2.1	72.9	0.7	0.61	29.1	25.8	31.0	14.1	0.81

[a]Determined by ICP-OES. [b]Calculated from the results of the XPS and the elemental analyses. [c]The potential at j = −0.05 mA·cm^{-2} in the ORR polarization curve.

1-3. Summary

The author demonstrated that the Fe/N/C catalysts prepared by applying the bottom-up synthesis of the N-doped GNR have excellent ORR activity. The catalysts prepared by pyrolysis of $FeCl_2$, N-GNR precursors and Vulcan® XC-72R exhibit positively shifted onset potentials of 0.88 V vs. RHE for Fe/**1**@VC and 0.86 V vs. RHE for Fe/**2**@VC. The ORR activity of Fe/**1**@VC is significantly higher than that of the other catalysts prepared from polymers **3** and **4**, and monomers **5**−**8**. The Fe/**1**@VC is found to have the highest content of the Fe−N_x active sites, thereby showing the highest ORR activity. In addition, it is verified that the efficiency of the formation of the Fe−N_x active sites highly depends on the position of nitrogen atoms in the framework of the N-GNR precursor, which enables formation of N2 sites coordinating to the iron ions on the edge of GNRs. Furthermore, the important process of the construction of the Fe−N_x active sites involves the intramolecular annulation and the graphitization of precursor **1** at approximately 700 °C during pyrolysis This work provides an attractive strategy for designing proper Fe−N_x active sites and the relationship between the chemical structure of the precursor and the ORR activity of the Fe/N/C catalysts.

1-4. Experimental Section

Materials and methods

All reagents were used without purification. All solvents were dried with molecular sieves 3Å before use. ^{1}H NMR and ^{13}C NMR spectra were recorded on a Bruker BioSpin DPX400 NMR spectrometer (400 MHz). ESI-TOF MS analyses were performed on a Bruker micrOTOF focus III mass spectrometer. Thernally decomposition temperature (T_d) values of the precursors were determined by thermogravimetry analysis (TGA) using a Mac Science TG-DTA TMA DSC with a heating rate of 10 ºC·min^{-1} in an N_2 stream on platinum pan. The morphologies of the catalysts and their elemental mapping images were investigated by scanning electron microscopy (SEM) using JEOL JSM-7600F equipped with an energy-dispersive X-ray spectroscope (EDX). High-resolution transmission electron microscopy (HR-TEM) observations were performed using a HITACHI HF-2000 field emission TEM operated at an accelerating voltage of 200 kV. X-ray diffraction (XRD) spectra were measured with Bruker D2 PHASER 2nd Generation with CuKα radiation. The iron content of the Fe/N/C catalysts was characterized by inductively coupled plasma optical emission spectroscopy (ICP-OES) using a SHIMAZDU ICPS-7510 system. The elemental analysis of carbon, hydrogen and nitrogen was performed on JM10 (J-SCIENCE LAB Co., Ltd.). Raman spectra were obtained using a JASCO NRS3100 instrument with a 532 nm laser. XAS measurements were conducted at the BL11 beamline of SAGA Light Source (SAGA-LS) at Tosu, Japan. ATHENA program was used for the Fe K-edge spectra analysis.[51] The EXAFS data were processed according to the standard procedures using the ATHENA module implemented in the IFEFIT software packages. The phase corrections of EXAFS spectra were performed by REX2000 (Rigaku Co.).[52] The chemical bonding states of nitrogen species in the catalysts were determined by X-ray photoelectron spectroscopy (XPS) performed on a SHIMADZU KRATOSAXIS-165x.

Synthesis of the precursors

Acetylene derivatives, 5,10-dibromo-1,3-diphenyl-2*H*cyclopenta[*l*]phenanthren-2-one (**9**), 1,3-diphenyl-2*H*-cyclopenta-[*l*]phenanthren-2-one (**14**), and compounds **10**−**13** and **5**−**8** were synthesized according to the literature with some modifications.[34,40] Compound **9**, for synthesis of compounds **10**−**13**, or **14**, for synthesis of compounds **5**−**8**, (7.7 mmol) and acetylene derivatives (7.7 mmol) were suspended in diphenyl ether (50 mL) and the mixture was deoxygenated by freeze−pump−thaw cycling three times. The mixture was refluxed under an Ar atmosphere for 12 h. After the reaction mixture was cooled to room temperature, the solvent was removed in vacuo. The residues were purified by silica gel column chromatography (hexane/AcOEt).

Synthesis of 3,3′-(6,11-Dibromo-1,4-diphenyltriphenylene-2,3-diyl)dipyridine (10)

Compound **9** (4.2 g, 7.7 mmol) and 1,2-di(pyridin-3-yl)ethyne (1.4 g, 7.7 mmol) were used for the reaction, and the product was obtained as a white solid. Yield 22%. ^{1}H NMR (400 MHz, DMSO-d_6): δ = 8.50 (d, 2H, J = 8.4 Hz), 8.11 (d, 2H, J = 4.8 Hz), 7.96 (d, 2H, J = 6.4 Hz), 7.66 (s, 2H), 7.63 (d, 2H, J = 8.8 Hz), 7.22 (m, 6H), 7.19 (m, 2H), 7.10 (m, 4H), 6.96 (m, 2H); ^{13}C NMR (100 MHz, DMSO- d_6): δ = 151.36, 151.29, 147.21, 141.50, 138.63, 138.46, 133.67, 132.33, 131.86, 131.83, 130.48, 130.35, 129.87, 129.03, 127.68, 126.08, 122.39, 122.31, 120.17; ESI-TOF MS (positive mode) *m*/*z* calcd. for $C_{40}H_{24}Br_2N_2$ $[M + H]^+$ 691.0379, found 691.0369.

Synthesis of 3,3′-(6,11-Dibromo-1,4-diphenyltriphenylene-2,3-diyl)diquinoline (11)

Compound **9** (4.2 g, 7.7 mmol) and 1,2-di(quinolin-3-yl)ethyne (2.2 g, 7.7 mmol) were used for the reaction, and the product was obtained as a white solid. Yield 25%. ^{1}H NMR (400 MHz, CD_2Cl_2): δ = 8.33 (d, 1H, J = 2.0 Hz), 8.30 (d, 2H, J = 8.8 Hz), 8.27 (d, 1H, J = 2.0 Hz), 7.80 (t, 2H, J = 6.0 Hz), 7.74 (d, 1H, J = 2.0 Hz), 7.72 (d, 1H, J = 2.0 Hz), 7.55 (m, 6H), 7.40 (m, 4H), 7.15 (m, 10H); ^{13}C NMR (100 MHz, CD_2Cl_2): δ = 152.56, 152.46, 146.07, 141.71, 139.16, 139.13, 138.35, 138.26, 138.13, 133.30, 133.26, 133.04, 132.32, 132.27, 132.11, 131.52, 131.48, 130.45, 130.24, 129.66, 129.61, 129.38, 129.23, 129.12, 129.10, 129.01, 127.91, 127.75, 127.69, 127.66, 127.14, 127.07, 126.99, 126.94, 125.15, 120.59; ESI-TOF MS (positive mode) *m*/*z* calcd. for $C_{48}H_{28}Br_2N_2$ $[M + H]^+$ 791.0692, found 791.0687.

Synthesis of 4,4′-(6,11-Dibromo-1,4-diphenyltriphenylene-2,3-diyl)dipyridine (12)

Compound **9** (4.2 g, 7.7 mmol) and 1,2-di(pyridin-4-yl)ethyne (1.4 g, 7.7 mmol) were used for the reaction, and the product was obtained as a white solid. Yield 28%. ^{1}H NMR (400 MHz, CD_2Cl_2): δ = 8.27 (d, 2H, J = 8.8 Hz), 7.71 (d, 2H, J = 2.0 Hz), 7.55 (dd, 2H, J = 2.0, 8.4 Hz), 7.23 (m, 6H), 7.07 (m, 4H); ^{13}C NMR (100 MHz, CD_2Cl_2): δ = 148.32, 141.38, 138.11, 137.82, 132.99, 132.18, 132.00, 131.37, 130.48, 130.19, 129.06, 127.85, 125.14, 120.58; ESI-TOF MS (positive mode) *m*/*z* calcd. for $C_{40}H_{24}Br_2N_2$ $[M + H]^+$ 691.0379, found 691.0311.

Synthesis of 3,3′-(1,4-Diphenyltriphenylene-2,3-diyl)dipyridine (5)

Compound **14** (2.9 g, 7.7 mmol) and 1,2-di(pyridin-3-yl)ethyne (1.4 g, 7.7 mmol) were used for the reaction, and the product was obtained as a white solid. Yield 34%. ^{1}H NMR (400 MHz, CD_2Cl_2): δ = 8.47 (d, 2H, J = 7.6 Hz), 8.16 (m, 2H), 7.93 (dd, 2H, J = 2.4, 9.6 Hz), 7.63 (dd, 2H, J = 0.8, 8.4 Hz), 7.10 (m, 14H), 6.90 (m, 2H); ^{13}C NMR (100 MHz, CD_2Cl_2): δ = 152.10, 151.90, 147.10, 147.08, 142.60, 138.94, 138.74, 138.24, 137.23, 137.19, 136.47, 136.41, 132.58, 132.48, 132.39, 132.33, 132.22, 132.20, 132.10, 130.75, 130.20, 128.87, 128.83, 128.64, 128.62, 127.25, 127.10, 126.02, 123.67, 122.39, 122.18; ESI-TOF MS (positive mode) *m*/*z* calcd. for $C_{40}H_{26}N_2$ $[M + H]^+$ 535.2169, found 535.2170.

Synthesis of 3,3′-(1,4-Diphenyltriphenylene-2,3-diyl)diquinoline (6)

Compound **14** (2.9 g, 7.7 mmol) and 1,2-di(quinolin-3-yl)ethyne (2.1 g, 7.7 mmol) were used for the reaction, and the product was obtained as a white solid. Yield 41%. ^{1}H NMR (400 MHz, CD_2Cl_2): δ = 8.49 (d, 2H, J = 8.0 Hz), 8.31 (d, 1H, J = 2.4 Hz), 8.25 (d, 1H, J = 2.4 Hz), 7.80 (m, 2H), 7.63 (t, 2H, J = 7.2 Hz), 7.50 (m, 10H), 7.05 (m, 12H); ^{13}C NMR (100 MHz, CD_2Cl_2): δ = 152.72, 145.94, 142.53, 138.71, 137.26, 133.75, 133.71, 132.50, 132.36, 132.18, 130.76, 130.23, 129.58, 128.92, 128.81, 128.79, 128.70, 127.90, 127.73, 127.33, 127.17, 126.94, 126.08, 123.71; ESI-TOF MS (positive mode) *m*/*z* calcd. for $C_{48}H_{30}N_2$ $[M + H]^+$ 635.2482, found 635.2476.

Synthesis of 4,4′-(1,4-Diphenyltriphenylene-2,3-diyl)dipyridine (7)

Compound **14** (2.9 g, 7.7 mmol) and 1,2-di(pyridin-4-yl)ethyne (1.4 g, 7.7 mmol) were used for the reaction, and the product was obtained as a white solid. Yield 28%. ^{1}H NMR (400 MHz, CD_2Cl_2): δ = 8.46 (dd, 2H, J = 1.2, 8.0 Hz), 8.13 (dd, 4H, J = 1.6, 6.0 Hz), 7.61 (dd, 2H, J = 0.8, 8.4 Hz), 7.45 (t, 2H, J = 7.6 Hz), 7.16 (m, 6H), 7.05 (m, 6H), 6.70 (dd, 4H, J = 1.6, 6.0 Hz); ^{13}C NMR (100 MHz, CD_2Cl_2): δ = 149.12, 148.47, 142.23, 137.43, 137.19, 132.34, 132.24, 132.14, 130.64, 130.20, 128.76, 127.37, 126.93, 126.07, 125.26, 123.70; ESI-TOF MS (positive mode) *m*/*z* calcd. for $C_{40}H_{26}N_2$ $[M + H]^+$ 535.2178, found 535.2170.

General Procedure for the Synthesis of Polymer Precursors (1−4)[34,40]

$Ni(COD)_2$ (2.0 g, 5.9 mmol), 2,2′-bipyridine (920 mg, 5.9 mmol), and COD (1.1 mL, 5.9 mmol) were added to degassed dimethylformamide (DMF) (26 mL). The reaction mixture was heated at 55 °C for 30 min. Compound **10**−**13** (1.5 mmol) in degassed toluene (30 mL) was added to the reaction mixture. The mixture was stirred at 80 °C for 2 days. The polymer was precipitated by addition of methanol (100 mL), filtered, and washed with methanol, conc. HCl, water, 0.5 M NaOH solution in methanol, water, acetone, and hexane to obtain a yellow solid.

Synthesis of precursor 1

Compound **10** (1.0 g, 1.5 mmol) was polymerized to give compound **1** as a yellow solid (650 mg). The obtained compound was identified by MALDI-TOF MS (Figure 1-4a).

Synthesis of precursor 2

Compound **11** (1.2 g, 1.5 mmol) was polymerized to give compound **2** as a yellow solid (670 mg). The obtained compound was identified by MALDI-TOF MS (Figure 1-4b).

Synthesis of precursor 3

Compound **12** (1.0 g, 1.5 mmol) was polymerized to give compound **3** as a yellow solid (400 mg). The obtained compound was identified by MALDI-TOF MS (Figure 1-4c).

Synthesis of precursor 4

Compound **13** (1.0 g, 1.5 mmol) was polymerized to give compound **4** as a yellow solid (710 mg). The obtained compound was identified by MALDI-TOF MS (Figure 1-4d).

Preparation of the catalysts

Method A

Carbon black Vulcan® XC-72R (VC, Cabot, USA) was used as a carbon support. Electrocatalysts were prepared from the precursors and VC by pyrolysis in N_2 flow as follows: the precursors (0.1 mmol) dissolved in $CHCl_3$ (50 mL), $FeCl_2 \cdot 4H_2O$ (19.8 mg, 0.1 mmol) dissolved in methanol (10 mL) and VC powder (33.3 mg) was mixed. The suspension was vigorously vortexed and sonicated for 30 min. After removal of the solvent, the residue was placed on an alumina boat (length: 80 mm, width: 16 mm, height: 10 mm), and then inserted into a quartz tube (diameter 50 mm, length 800 mm). The quartz tube was installed in a hinge split tube furnace (Koyo Thermo Systems Co., Ltd., KTF045N1). The residue was preheated from ambient temperature to 300 ºC for 1 h under N_2 flow (0.2 $L \cdot min^{-1}$) and incubated for 2 h. The residue was then immediately heated to 1000 ºC for 1 h, and then incubated for 2 h. The temperature of the sample inside the furnace was recorded with a thermocouple equipped with a data logger (CHINO Corporation, MC3000). After cooling, the pyrolyzed catalyst was ground, suspended in a 0.5 M H_2SO_{4aq} solution, incubated at 80 ºC for 3 h to leach out impurities such as iron oxides and iron carbides, and washed with excess volumes of deionized water. The dried carbon catalyst was used for the experiments.

Method B

MgO particles (ϕ = 50 nm, Sigma-Aldrich) were used as a template material. Electrocatalysts were prepared from the precursors and MgO by pyrolysis under N_2 flow as follows: the precursors (0.1 mmol) dissolved in $CHCl_3$ (50 mL), $FeCl_2 \cdot 4H_2O$ (19.8 mg, 0.1 mmol) dissolved in methanol (10 mL) and MgO particle powders (316 mg) were mixed. The suspension was vigorously vortexed and sonicated for 30 min. After removal of the solvent, the residue was placed on an alumina boat (length: 80 mm, width: 16 mm, height: 10 mm), and then inserted into a quartz tube (diameter 50 mm, length 800 mm). The quartz tube was installed in a hinge split tube furnace (Koyo Thermo Systems Co. Ltd., KTF045N1). The residue was heated to 500 °C, 600 °C, 700 °C, 800 °C, 900 °C, or 1000 °C, respectively, and incubated for 2 h under N_2 flow (0.2 $L \cdot min^{-1}$). The rate of temperature increase was set to 2 $°C \cdot min^{-1}$. The temperature of the sample inside the furnace was recorded with a thermocouple equipped with a data logger (CHINO Corporation, MC3000). After cooling, the pyrolyzed catalyst was ground, suspended in a 1.0 M HNO_{3aq} solution, incubated at room temperature for 2 h to leach out impurities such as iron oxides and iron carbides and the MgO templates, and then washed with excess volumes of deionized water. This entire acid washing process was then repeated for extra two times. The dried carbon catalyst was used for the experiments.

Electrochemical measurements

The performance of the catalyst in ORR was evaluated in a 0.1 M $HClO_{4aq}$ solution. A rotating ring-disk electrode (RRDE) with a glassy carbon disk electrode (ϕ = 5 mm) and a platinum ring was used for the electrochemical measurements. Electrode rotation rates were controlled using a Pine Instruments AFMSRCE rotator with a Pine MSRX motor controller. An electrode was polished to mirror flat with alumina powder (50 nm) before use. The catalyst ink was prepared with 4.0 mg of catalyst and 100 μL of 5 wt% Nafion® (Sigma–Aldrich) in a mixture of lower aliphatic alcohols and H_2O. The ink was vortexed and sonicated in an ultrasonic bath at 100 W at 35 kHz for

30 min. Then, 2 μL of catalyst ink was loaded onto the surface of the electrode and dried. Electrochemical tests were conducted with a potentiostat (ALS, electrochemical analyzer model 610B) using a typical three-electrode system, with platinum wire as a counter electrode and Ag/AgCl as a reference electrode. The potential difference between Ag/AgCl and RHE was calculated, and the value is 0.258 V in a 0.1 M $HClO_{4aq}$ solution. The scan rate was 5 $mV{\cdot}s^{-1}$ from −0.258 to 0.742 V vs. the Ag/AgCl reference electrode. Before each potential scan, the electrolyte of the 0.1 M $HClO_{4aq}$ solution was saturated with O_2 for at least 30 min, and O_2 purging was continued during the electrochemical experiments. The measured currents of the disk and the ring electrodes were subtracted from the background current at the N_2-saturated electrolyte. In the RRDE test, the ring potential was set to 1.0 V versus the Ag/AgCl reference electrode. The onset potentials (E_{onset}) were defined as a potential showing $j = -0.05$ $mA{\cdot}cm^{-2}$ in RDE measurement, where j represents the current density. The RRDE collection efficiency (N) was calibrated in 0.1 M $HClO_{4aq}$ solution with 10 mM $K_3Fe(CN)_6$ electrolyte. The measured N value is 0.26 in our system. The percentage of H_2O_2 in total amount of the product was calculated by equation 1:

$$X_{\mathrm{H_2O_2}} = 2\,I_{\mathrm{r}}\,(I_r + N \times |I_{\mathrm{d}}|) \times 100 \quad \text{---------- (1)}$$

The TOF value which is defined as the number of electrons transferred per an active site and unit time (second) ($e{\cdot}site^{-1}{\cdot}s^{-1}$) was calculated by equation 2:

$$TOF = J_{kin}(0.8\ \mathrm{V\ vs.\ RHE})/(MSD \times e) \quad \text{---------- (2)}$$

where J_{kin} (0.8 V vs. RHE) represents the gravimetric kinetic current density ($A{\cdot}g^{-1}$) at 0.8 V vs. RHE, MSD (mass-based site density) is the number of the Fe–N_x active sites normalized by mass of the catalyst ($sites{\cdot}g^{-1}$), and e is elementary charge. The J_{kin} value is calculated by equation 3:

$$J_{kin}(0.8\ \mathrm{V\ vs.\ RHE}) = J_{lim} \times J(0.8\ \mathrm{V\ vs.\ RHE})/(|J_{lim}| - |J(0.8\ \mathrm{V\ vs.\ RHE})|) \quad \text{---------- (3)}$$

where J_{lim} represents the gravimetric limiting current density, and $J_{0.8\ \mathrm{V}}$ is the gravimetric current density observed at 0.8 V vs. RHE. J_{lim} and $J_{0.8\ \mathrm{V}}$ can be evaluated from the linear sweep voltammograms in the RDE measurement. MSD was evaluated by the cyclic voltammetry (CV) in an N_2-saturated 0.1 M $HClO_{4aq}$ solution at 50 $mV{\cdot}s^{-1}$ at 2000 rpm from −0.258 to 0.742 V vs. the Ag/AgCl reference electrode (Figure 1-8) and calculated by equation 4:

$$MSD = Q/(e \times n \times g_{cat}) \quad \text{---------- (4)}$$

where Q represents $Fe^{2+/3+}$ coulombic charge (C) calculated from the result of CV in an N_2-saturated solution, n is reaction number ($n = 1$ in this redox system), and g_{cat} is loaded weight of the catalyst (0.08 mg).

References and Notes

[1] M. K. Debe, *Nature* **2012**, *486*, 43−51.

[2] D. Banham, S. Ye, *ACS Energy Lett*. **2017**, *2*, 629−638.

[3] M. Shao, Q. Chang, J.-P. Dodelet, R. Chenitz, *Chem. Rev.* **2016**, *116*, 3594−3657.

[4] A. Rabis, P. Rodriguez, T. J. Schmidt, *ACS Catal.* **2012**, *2*, 864−890.

[5] D. Higgins, P. Zamani, A. Yu, Z. Chen, *Energy Environ. Sci.* **2016**, *9*, 357−390.

[6] F. Jaouen, E. Proietti, M. Lefèvre, R. Chenitz, J.-P. Dodelet, G. Wu, H. T. Chung, C. M. Johnston, P. Zelenay, *Energy Environ. Sci.* **2011**, *4*, 114−130.

[7] U. Martinez, S. Komini Babu, E. F. Holby, H. T. Chung, X. Yin, P. Zelenay, *Adv*. *Mater*. **2019**, *31*, 1806545.

[8] Q. Li, R. Cao, J. Cho, G. Wu, *Adv. Energy Mater.* **2014**, *4*, 1301415.

[9] W. Wang, Q. Jia, S. Mukerjee, S. Chen, *ACS Catal.* **2019**, *9*, 10126−10141.

[10] X. X. Wang, M. T. Swihart, G. Wu, *Nat. Catal.* **2019**, *2*, 578−589.

[11] M. Lefèvre, E. Proietti, F. Jaouen, J.-P. Dodelet, *Science* **2009**, *324*, 71−74.

[12] R. Bashyam, P. Zelenay, *Nature* **2006**, *443*, 63−66.

[13] G. Wu, K. L. More, C. M. Johnston, P. Zelenay, *Science* **2011**, *332*, 443−447.

[14] Z. Chen, D. Higgins, A. Yu, L. Zhang, J. Zhang, *Energy Environ. Sci.* **2011**, *4*, 3167−3192.

[15] Y. Chen, S. Ji, Y. Wang, J. Dong, W. Chen, Z. Li, R. Shen, L. Zheng, Z. Zhuang, D. Wang, Y. Li, *Angew. Chem. Int. Ed.* **2017**, *56*, 6937−6941.

[16] Q. Lai, L. Zheng, Y. Liang, J. He, J. Zhao, J. Chen, *ACS Catal.* **2017**, *7*, 1655−1663.

[17] H. Zhang, S. Hwang, M. Wang, Z. Feng, S. Karakalos, L. Luo, Z. Qiao, X. Xie, C. Wang, D. Su, Y. Shao, G. Wu, *J. Am. Chem. Soc.* **2017**, *139*, 14143−14149.

[18] R. Jiang, L. Li, T. Sheng, G. Hu, Y. Chen, L. Wang, *J. Am. Chem. Soc.* **2018**, *140*, 11594−11598.

[19] U. I. Kramm, J. Herranz, N. Larouche, T. M. Arruda, M. Lefèvre, F. Jaouen, P. Bogdanoff, S. Fiechter, I. Abs-Wurmbach, S. Mukerjee, J.-P. Dodelet, *Phys. Chem. Chem. Phys.* **2012**, *14*, 11673−11688.

[20] N. Ramaswamy, U. Tylus, Q. Jia, S. Mukerjee, *J. Am. Chem. Soc.* **2013**, *135*, 15443−15449.

[21] Q. Jia, N. Ramaswamy, U. Tylus, K. Strickland, J. Li, A. Serov, K. Artyushkova, P. Atanassov, J. Anibal, C. Gumeci, S. C. Barton, M.-T. Sougrati, F. Jaouen, B. Halevi, S. Mukerjee, *Nano Energy* **2016**, *29*, 65−82.

[22] H. T. Chung, D. A. Cullen, D. Higgins, B. T. Sneed, E. F. Holby, K. L. More, P. Zelenay, *Science* **2017**, *357*, 479−484.

[23] L. Li, S. Shen, G. Wei, X. Li, K. Yang, Q. Feng, J. Zhang, *ACS Appl. Mater. Interfaces* **2019**, *11*, 14126−14135.

[24] T. Mineva, I. Matanovic, P. Atanassov, M.-T. Sougrati, L. Stievano, M. Clémancey, A. Kochem, J.-M. Latour, F. Jaouen, *ACS Catal.* **2019**, *9*, 9359−9371.

[25] U. Tylus, Q. Jia, K. Strickland, N. Ramaswamy, A. Serov, P. Atanassov, S. Mukerjee, *J. Phys. Chem. C* **2014**, *118*, 8999−9008.

[26] M. Kim, J. M. Yoo, C.-Y. Ahn, J.-H. Jang, Y. J. Son, H. Shin, J. Kang, Y. S. Kang, S. J. Yoo, K.-S. Lee, Y.-E. Sung, *ChemCatChem* **2019**, *11*, 5982−5988.

[27] Y. Mun, S. Lee, K. Kim, S. Kim, S. Lee, J. W. Han, J. Lee, *J. Am. Chem. Soc.* **2019**, *141*, 6254−6262.

[28] Y. Wang, Y.-J. Tang, K. Zhou, *J. Am. Chem. Soc.* **2019**, *141*, 14115−14119.

[29] X.-Y. Wang, X. Yao, K. Müllen, *Sci*. *China Chem*. **2019**, *62*, 1099−1144.

[30] M. Müller, C. Kübel, K. Müllen, *Chem. Eur. J.* **1998**, *4*, 2099−2109.

[31] J. Wu, W. Pisula, K. Müllen, *Chem. Rev.* **2007**, *107*, 718−747.

[32] A. Narita, X. Feng, K. Müllen, *Chem. Rec.* **2015**, *15*, 295−309.

[33] J. Cai, P. Ruffieux, R. Jaafar, M. Bieri, T. Braun, S. Blankenburg, M. Muoth, A. P. Seitsonen, M. Saleh, X. Feng, K. Müllen, R. Fasel, *Nature* **2010**, *466*, 470−473.

[34] J. Cai, C. A. Pignedoli, L. Talirz, P. Ruffieux, H. Söde, L. Liang, V. Meunier, R. Berger, R. Li, X. Feng, K. Müllen, R. Fasel, *Nat. Nanotechnol.* **2014**, *9*, 896−900.

[35] Z. Chen, W. Zhang, C.-A. Palma, A. Lodi Rizzini, B. Liu, A. Abbas, N. Richter, L. Martini, X.-Y. Wang, N. Cavani, H. Lu, N. Mishra, C. Coletti, R. Berger, F. Klappenberger, M. Kläui, A. Candini, M. Affronte, C. Zhou, V. De Renzi, U. del Pennino, J. V. Barth, H. J. Räder, A. Narita, X. Feng, K. Müllen, *J. Am. Chem. Soc.* **2016**, *138*, 15488−15496.

[36] X.-Y. Wang, J. I. Urgel, G. B. Barin, K. Eimre, M. Di Giovannantonio, A. Milani, M. Tommasini, C. A. Pignedoli, P. Ruffieux, X. Feng, R. Fasel, K. Müllen, A. Narita, *J. Am. Chem. Soc.* **2018**, *140*, 9104−9107.

[37] X.-Y. Wang, X. Yao, A. Narita, K. Müllen, *Acc. Chem. Res.* **2019**, *52*, 2491−2505.

[38] Y. Tanaka, A. Onoda, S.-i. Okuoka, T. Kitano, K. Matsumoto, T. Sakata, H. Yasuda, T. Hayashi, *ChemCatChem* **2018**, *10*, 743−750.

[39] A. Onoda, Y. Tanaka, K. Matsumoto, M. Ito, T. Sakata, H. Yasuda, T. Hayashi, *RSC Adv*. **2018**, *8*, 2892−2899.

[40] T. H. Vo, M. Shekhirev, D. A. Kunkel, M. D. Morton, E. Berglund, L. Kong, P. M. Wilson, P. A. Dowben, A. Enders, A. Sinitskii, *Nat. Commun.* **2014**, *5*, 3189.

[41] W. Liu, L. Zhang, X. Liu, X. Liu, X. Yang, S. Miao, W. Wang, A. Wang, T. Zhang, *J. Am. Chem. Soc.* **2017**, *139*, 10790−10798.

[42] S. Yasuda, Y. Uchibori, M. Wakeshima, Y. Hinatsu, H. Ogawa, M. Yano, H. Asaoka, *RSC Adv*. **2018**, *8*, 37600−37605.

[43] Q. Jia, N. Ramaswamy, H. Hafiz, U. Tylus, K. Strickland, G. Wu, B. Barbiellini, A. Bansil, E. F. Holby, P. Zelenay, S. Mukerjee, *ACS Nano* **2015**, *9*, 12496−12505.

[44] H. Wang, N. Yang, W. Li, W. Ding, K. Chen, J. Li, L. Li, J. Wang, J. Jiang, F. Jia, Z. Wei, *ACS Energy Lett*. **2018**, *3*, 1345−1352.

[45] Y. J. Sa, J. Kim, S. Joo, *J. Electrochem. Sci. Technol.* **2017**, *8*, 169−182.

[46] L. Zhou, C. Yang, J. Wen, P. Fu, Y. Zhang, J. Sun, H. Wang, Y. Yuan, *J. Mater. Chem. A* **2017**, *5*, 19343−19350.

[47] Y. Wang, D. C. Alsmeyer, R. L. McCreery, *Chem. Mater.* **1990**, *2*, 557−563.

[48] T. H. Vo, M. Shekhirev, D. A. Kunkel, F. Orange, M. J. F. Guinel, A. Enders, A. Sinitskii, *Chem*. *Commun*. **2014**, *50*, 4172−4174.

[49] T. Jawhari, A. Roid, J. Casado, *Carbon* **1995**, *33*, 1561−1565.

[50] G. Katagiri, *TANSO* **1996**, *1996*, 304−313.

[51] A. Onoda, Y. Tanaka, T. Ono, S. Takeuchi, A. Sakai, T. Hayashi, *J. Porphyr. Phthalocyanines* **2015**, *19*, 510−516.

[52] T. Taguchi, T. Ozawa, H. Yashiro, *Phys. Scr.* **2005**, 205.

Chapter 2

Construction of Co−N_x Active Sites derived from Precursors Forming N-doped Graphene Nanoribbons for an Electrocatalytic Hydrogen Evolution Reaction

Reproduced in part with permission from [*Bull. Chem. Soc. Jpn.* **2021**, *94*, 2898−2905]
DOI: 10.1046/bcsj.20210302

2-1. Introduction

An efficient method of hydrogen production has been vigorously studied to overcome environmental and energy problems in efforts to improve hydrogen-based technologies.[1] The electrocatalytic hydrogen evolution reaction (HER) is a promising way to produce large amounts of pure hydrogen molecules. Therefore, a highly active electrocatalyst is required for achievement of high efficiency of the energy conversion. In particular, attractive non-precious metal-based catalysts including transition-metal chalcogenides, carbides, nitrides or phosphides, have been reported as alternatives for precious metal catalysts.[2−13]

In the class of non-precious metal-based catalysts, cobalt and nitrogen co-doped carbon (Co/N/C) catalysts have been attracted much attention because of the high catalytic activity and the durability in the HER.[14−18] Previous studies have revealed that the most plausible active site of the Co/N/C catalysts prepared by pyrolysis of precursors containing cobalt ion, nitrogen sources, and a carbon support is a Co−N_x coordination structure embedded within the graphene layer.[19−24] Particles of cobalt or cobalt oxide, which are less active for catalysis, are also generated by pyrolysis.[25] Such particles are easily produced by sintering during pyrolysis for the preparation of a catalyst. Therefore, methods for efficient and precise construction of the Co−N_x active sites have been required to suppress the sintering of cobalt atoms and enhance the activity of Co/N/C catalysts toward HER. In this sense, a wide range of precursors including macrocyclic compounds, polymers, metal-organic frameworks, and other carbon materials have been investigated.[25−31]

The author described a new method for construction of Fe−N_x active sites in Fe/N/C-type carbon catalysts using polymerized triphenylene compounds with preorganized aromatic rings as precursors in the chapter 1.[32] The design of the precursors was inspired by thermally controlled bottom-up synthesis of N-doped graphene nanoribbons (N-GNR) (Figure 2-1).[33−38] The triphenylene precursors having aromatic rings preorganized at the adjacent positions are converted to N-GNR structures with coordination sites for metal ions via intramolecular annulations during pyrolysis (Figure 2-2). This method was found to be advantageous for efficient construction of the Fe−N_x active sites in the Fe/N/C catalysts, which have high catalytic activity for the electrochemical oxygen reduction reaction.

Those facts led the author to expect that the method using N-GNR precursors is also effective in generating Co−N_x active sites in the Co/N/C catalysts with high electrocatalytic activity in HER. In this chapter, the author describes the characterization of the Co/N/C catalysts prepared by pyrolysis of the polymer of the triphenylene derivatives containing aromatic rings preorganized as an N-GNR precursor. It was found that the N-GNR precursors were converted to N-GNR with cobalt-chelating N2 ligand structures during the pyrolysis, and the cobalt-bound N-GNRs are incorporated into graphene layers. The resulting Co/N/C catalysts containing the Co−N_x active sites show the sufficiently high electrocatalytic HER activity.

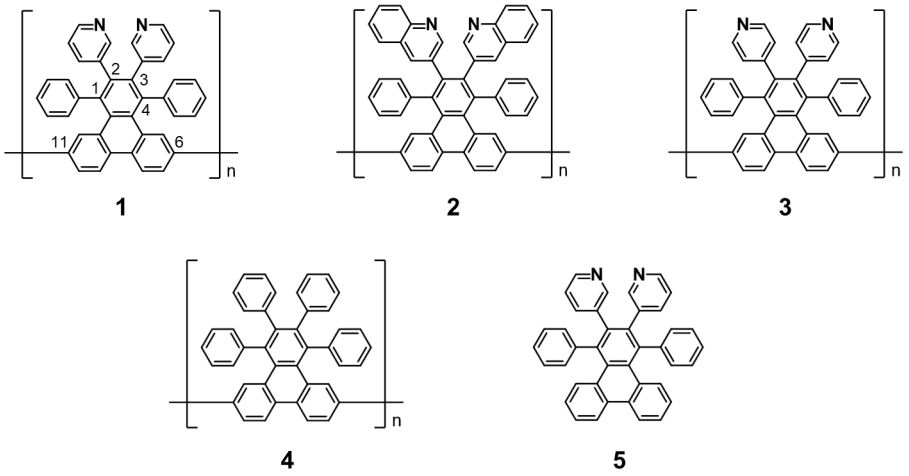

Figure 2-1. Chemical structures of precursors **1**−**5**.

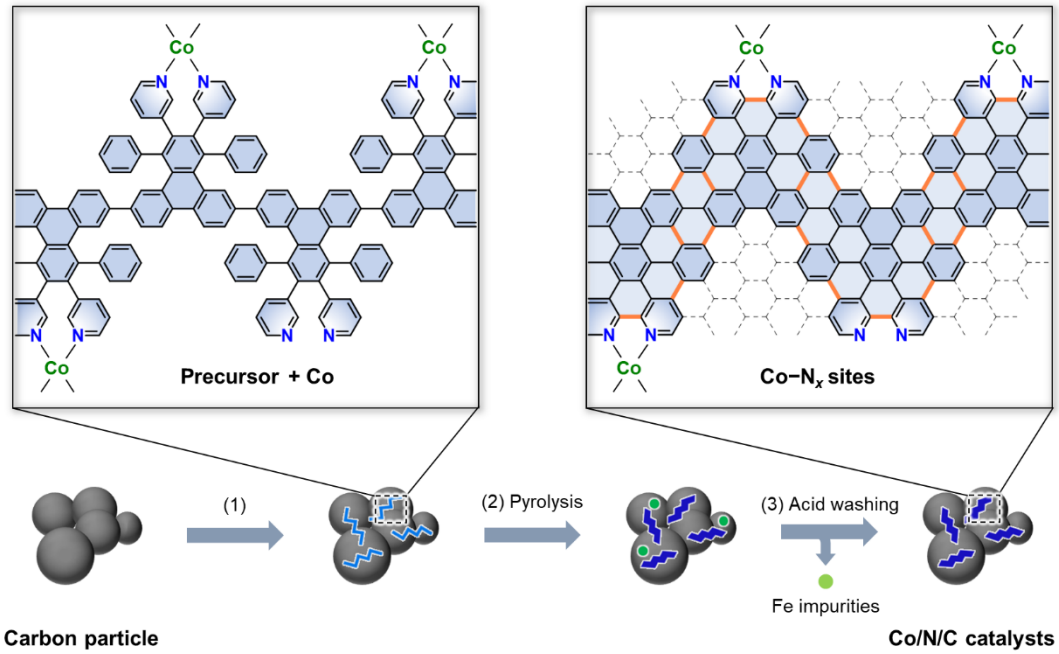

Figure 2-2. Schematic illustration of the procedures for preparation of the Co/N/C catalysts; (1) The precursor and cobalt ions (light blue) are mixed with carbon materials, (2) pyrolyzed at 1000 ºC under an N_2 atmosphere to construct Co−N_x sites derived from the precursor forming the N-GNR structure (blue), and (3) treated with a 0.5 M H_2SO_{4aq} solution to remove cobalt impurities (green).

2-2. Results and Discussion

Design and synthesis of precursors

To generate Co−N_x active sites along the GNR structure, the author employed polymer precursors **1**−**4**, in which 1,2,3,4-tetraaryltriphenylene units are connected at the positions of 6 and 11 (Figure 2-1). The phenyl or nitrogen-containing heterocycles linked to the triphenylene moiety were found to be converted to the GNR structure via intramolecular annulation during pyrolysis shown in the chapter 1.[32] Precursor **1** with two 3-pyridyl groups and precursor **2** with two 3-quinolyl groups were prepared to form N2 sites along with the GNR structure. Precursor **3** with two 4-pyridyl groups, precursor **4** without containing nitrogen atoms, and precursor **5** with a unit structure of precursor **1** were also prepared as references. The thermal durabilities of polymer precursors **1**−**4** are superior to monomer precursor **5**. Importantly, weight losses of polymer precursors **1**−**4**, determined by thermal gravimetric analysis performed under pyrolysis condition, are less than 20% because the precursors are converted to the thermally stable graphitized structure via formation of GNR structure at high temperature. In contrast, the weight loss of precursor **5** is almost 100% due to thermal decomposition or sublimation.[32] The thermal durability of the polymer precursors is thus expected to contribute to the efficient construction of Co−N_x active sites along with the GNR structure.

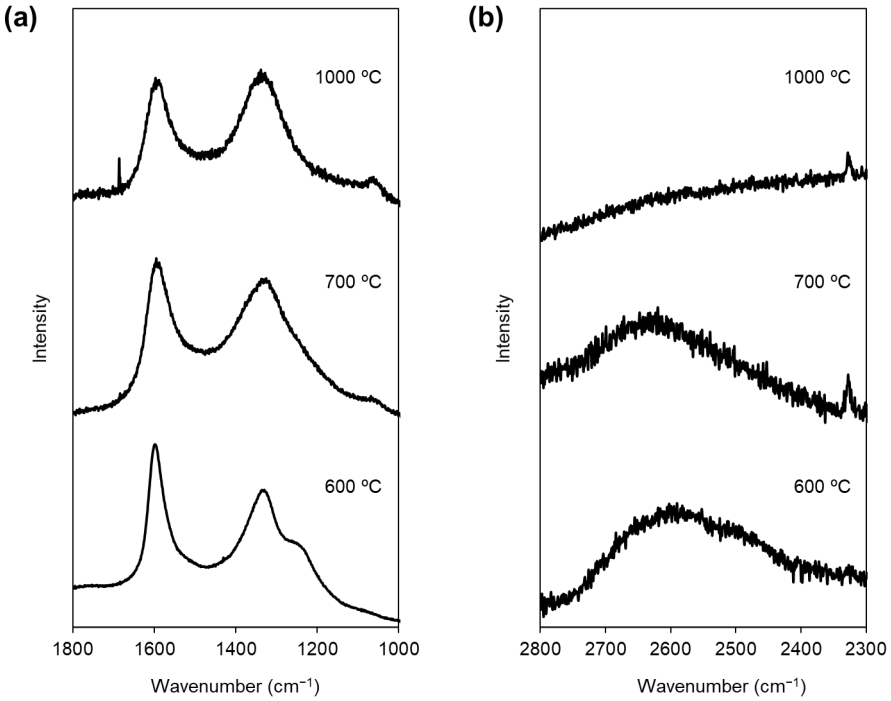

Figure 2-3. Raman spectra of the materials prepared by pyrolyzing precursor **1** at 600 ºC, 700 ºC, and 1000 ºC, respectively, under N_2 atmosphere without VC in the range of (a) 1000–1800 cm^{-1} and (b) 2200–2800 cm^{-1}.

The structural changes from the polymer precursor to N-GNR and from N-GNR to graphitic structure were confirmed by Raman spectroscopy. The polymer precursor **1** was pyrolyzed at 600 ºC, 700 ºC, and 1000 ºC, and these samples were analyzed by Raman spectroscopy (Figure 2-3). The material obtained by pyrolyzing precursor **1** at 600 ºC provides a sharp peak at 1600 cm^{-1} and two broad bands in the range of 1200–1400 cm^{-1} and 2400–2800 cm^{-1}. This spectral feature is consistent with that of the graphene nanoribbon reported in the literature.[34] The material obtained by pyrolyzing precursor **1** above 700 ºC provides broad D (1360 cm^{-1}) and G bands (1580 cm^{-1}), which are usually found in carbon materials. These findings suggest that the graphene nanoribbon structure converted from polymer precursor **1** is incorporated into the graphene layer above 700 ºC.

Preparation of the Co/N/C catalysts

The procedure for preparation of the Co/N/C catalysts is illustrated in Figure 2-2.[32,39,40] Precursor **1**−**5** and cobalt ions were combined with carbon supports, and the mixture was pyrolyzed and washed with a 0.5 M H_2SO_{4aq} solution to remove the cobalt impurities. The precursors are graphitized on the carbon support during pyrolysis via the formation of the Co−N_x structure on the edge of N-GNRs. The Co/N/C catalysts obtained from precursors **1**−**5** are shown as Co/**1**@VC, Co/**2**@VC, Co/**3**@VC, Co/**4**@VC, and Co/**5**@VC. Reference catalysts, Co@VC and VC, were prepared from the mixture of cobalt ion and VC, and only VC, respectively, following the same procedure.

Electrocatalytic activity for hydrogen evolution reaction (HER)

The HER activities of the carbon catalysts, Co/**1**@VC, Co/**2**@VC, Co/**3**@VC, Co/**4**@VC, Co/**5**@VC, Co@VC, and VC were determined using a rotating disk electrode (RDE) at 2000 rpm in N_2-saturated 0.1 M $HClO_{4aq}$ solution at pH 1 (Figure 2-4a). Co/**1**@VC and Co/**2**@VC show the high HER activities with the overpotentials of 311 and 315 mV (at 10 mA·cm^{-2}), respectively. In contrast, Co/**3**@VC needs greater overpotential of 387 mV, indicating that the position of the nitrogen atoms in the precursors affects the electrocatalytic performance of the Co/N/C catalysts. Furthermore, Co/**4**@VC demands much greater overpotential of 459 mV. Therefore, the nitrogen atoms in the precursors are essential for improving the HER activity. Co/**5**@VC prepared from monomeric precursor **5** requires overpotential of 458 mV, which is higher by 147 mV to Co/**1**@VC prepared from the corresponding polymer precursor **1**. Co@VC is less active than Co/**1**@VC−Co/**5**@VC although it is more active than VC.

HER promoted by the Co/N/C catalysts was analyzed using Tafel slopes obtained by the polarization curves (Figure 2-4b). The Tafel slopes of the different catalysts were determined to be 128 mV·dec^{-1} (Co/**1**@VC), 125 mV·dec^{-1} (Co/**2**@VC), 176 mV·dec^{-1} (Co/**3**@VC), 169 mV·dec^{-1} (Co/**4**@VC), 135 mV·dec^{-1} (Co/**5**@VC), 220 mV·dec^{-1} (Co@VC), and 233 mV·dec^{-1} (VC). The smaller values of the Tafel slope in Co/**1**@VC and Co/**2**@VC than those of the other carbon catalysts suggest that Co/**1**@VC and Co/**2**@VC show better electrocatalytic performance with high charge transfer coefficients in the HER.[41]

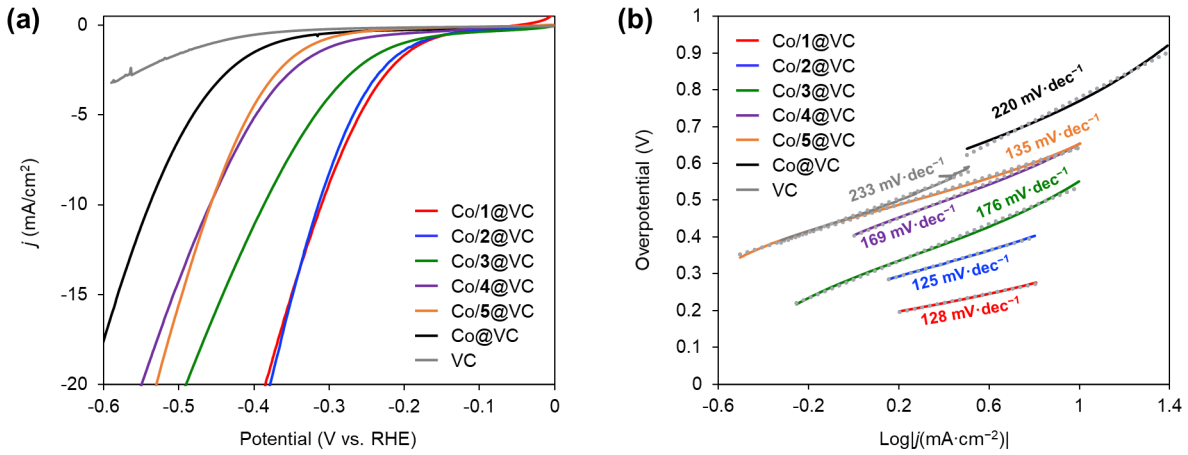

Figure 2-4. (a) Linear sweep voltammetry and (b) Tafel slopes in N_2-saturated 0.1 M $HClO_{4aq}$ solution at 5 $mV \cdot s^{-1}$ with 2000 rpm of Co/N/C catalysts: Co/**1**@VC (red), Co/**2**@VC (blue), Co/**3**@VC (green), Co/**4**@VC (purple), Co/**5**@VC (orange), Co@VC (black), and VC (gray).

The durability of Co/**1**@VC was evaluated by long-term chronoamperometric measurements (Figure 2-5a). The current value was maintained after three hours, indicating that Co/**1**@VC is tolerant under the experimental conditions. In addition, the amount of generated hydrogen gas was quantified by GC analysis (Figure 2-5b). Hydrogen was produced with Faradaic efficiency of 97%, as determined by the chronoamperometric curve and GC analysis.

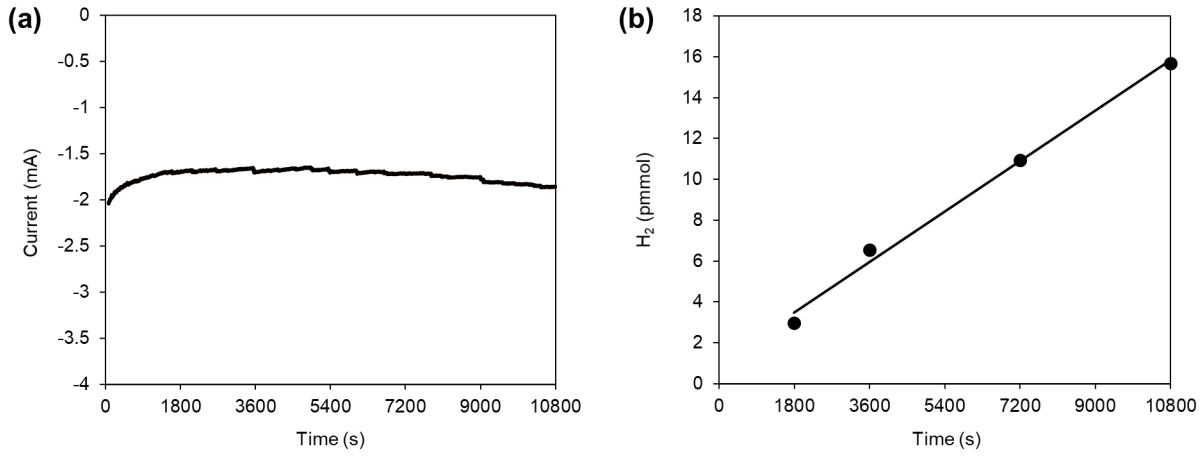

Figure 2-5. Evaluation of hydrogen gas. (a) Long-term chronoamperometric curve of Co/**1**@VC in an N_2-saturated 0.1 M $HClO_{4aq}$ solution. (b) GC analysis of the hydrogen gas produced during the chronoamperometry.

To determine the number of active species, mass-based site density (MSD), which represents the number of redox-active Co−N_x sites per unit mass of the catalyst, was calculated using the results of cyclic voltammetry (CV) in N_2-perged 0.1 M $HClO_{4aq}$ solution (Figure 2-6).[42] The obtained MSD values are 4.3×10^{19} sites·g_{cat}^{-1} (Co/**1**@VC), 3.5×10^{19} sites·g_{cat}^{-1} (Co/**2**@VC), 1.9×10^{19} sites·g_{cat}^{-1} (Co/**3**@VC), 0.7×10^{19} sites·g_{cat}^{-1} (Co/**4**@VC), 0.9×10^{19} sites·g_{cat}^{-1} (Co/**5**@VC), 0.8×10^{19} sites·g_{cat}^{-1} (Co@VC), suggesting that the chelating coordination between cobalt ion and nitrogen in the edge of precursors **1** and **2** promote the formations of the Co−N_x active sites. In addition, the HER activity is correlated with the MSD values. These results indicate that the redox-active Co−N_x sites largely contribute to the improvement of the HER activity. The results of electrochemical measurements are summarized in Table 2-1.

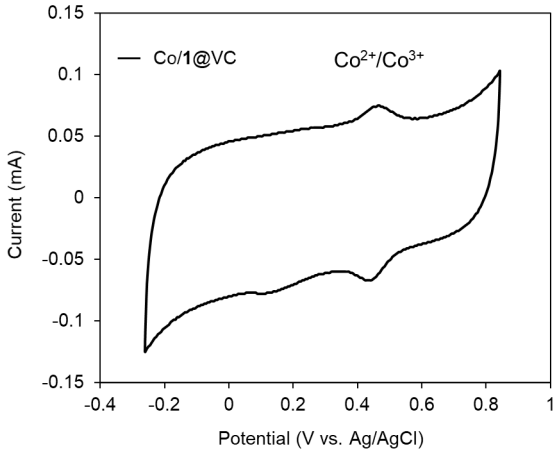

Figure 2-6. CV curve of Co/**1**@VC in an N_2-saturated 0.1 M $HClO_{4aq}$ solution at 10 mV·s^{-1} at 2000 rpm from −0.258 to 0.742 V vs. Ag/AgCl reference electrode.

Table 2-1. Summary of Electrochemical Measurements.

Co/N/C catalysts	Overpotential (mV)	Tafel slope (mV·dec^{-1})	MSD[a] (10^{19}·sites·g_{cat}^{-1})
Co/**1**@VC	311	128	4.3
Co/**2**@VC	315	125	3.5
Co/**3**@VC	387	176	1.9
Co/**4**@VC	459	169	0.7
Co/**5**@VC	458	135	0.9
Co@VC	539	220	0.8
VC	–	233	–

[a]Mass-based site density

Characterizations of the Co/N/C catalysts

The morphology of each catalyst was investigated by scanning transmission electron microscopy (STEM) (Figures 2-7 and 2-8). The annular dark field (ADF) STEM, and bright field (BF) STEM observations with EDX mapping analysis for caron and cobalt species for Co/**1**@VC, Co/**2**@VC, Co/**3**@VC, Co/**4**@VC, Co/**5**@VC, and Co@VC revealed that cobalt particles are present on all the catalysts. The average radii of cobalt particles in each catalyst determined by image analysis for the ADF-STEM images (Figures 2-7a−f) are 14 nm (Co/**1**@VC), 17 nm (Co/**2**@VC), 15 nm (Co/**3**@VC), 19 nm (Co/**4**@VC), 15 nm (Co/**5**@VC), and 42 nm (Co@VC). Most of these cobalt particles are encapsulated by the graphitic layers (Figure 2-7g). More detailed structures of the catalysts were investigated by high-angle annular dark field (HAADF) STEM (Figures 2-9). Importantly, bright spots with atomic size were observed in the HAADF-STEM images (Figures 2-9a−f). These species were identified as cobalt atoms by electron energy loss spectroscopy (EELS) coupled with the microscopy (Figure 2-9g). These results clarified that the Co/N/C catalysts contain atomically dispersed cobalt sites as well as cobalt particles.

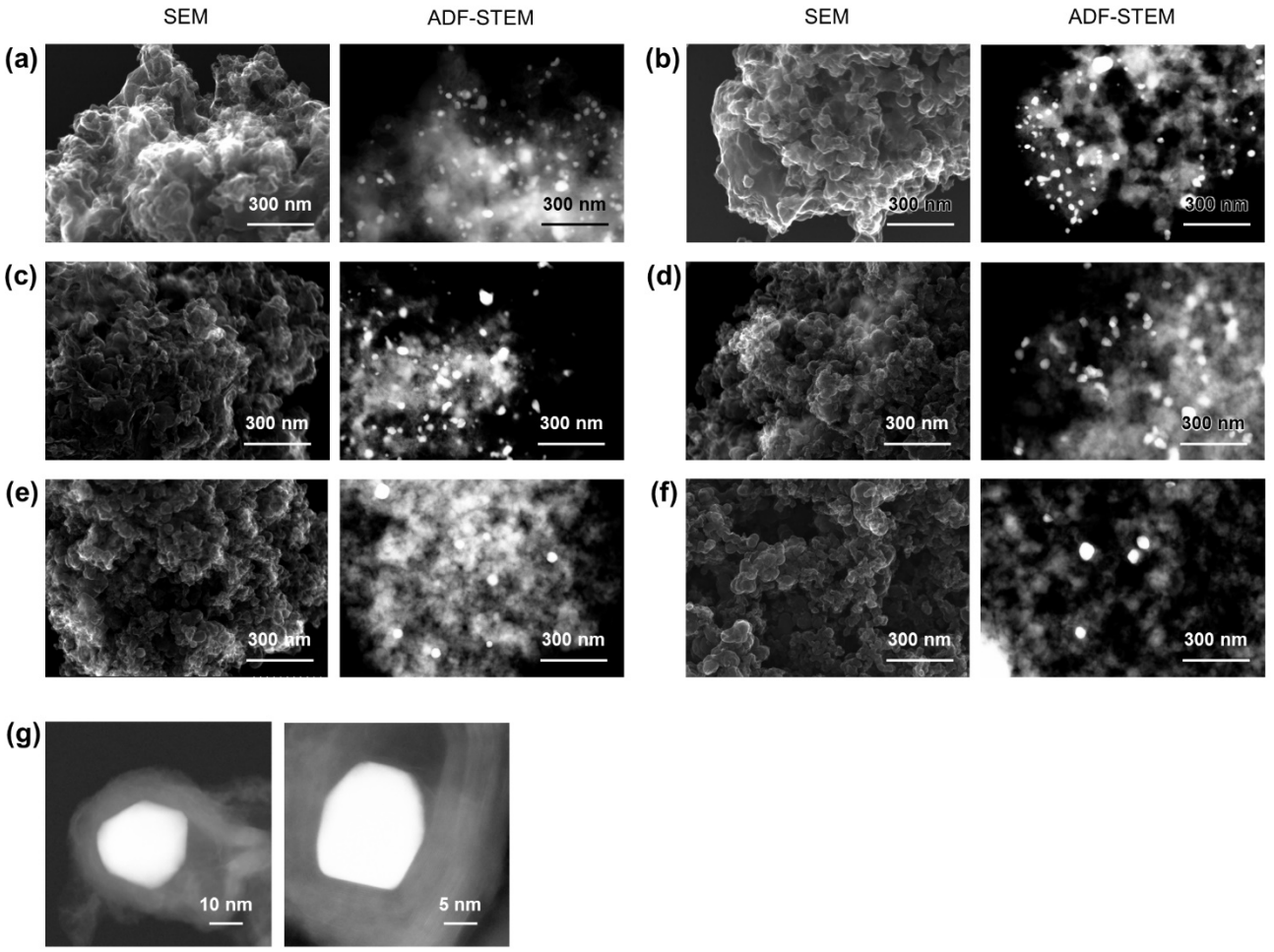

Figure 2-7. SEM and ADF-STEM images of (a) Co/**1**@VC, (b) Co/**2**@VC, (c) Co/**3**@VC, (d) Co/**4**@VC, (e) Co/**5**@VC, and (f) Co@VC. (g) ADF-STEM images of the representative cobalt particles in the catalysts.

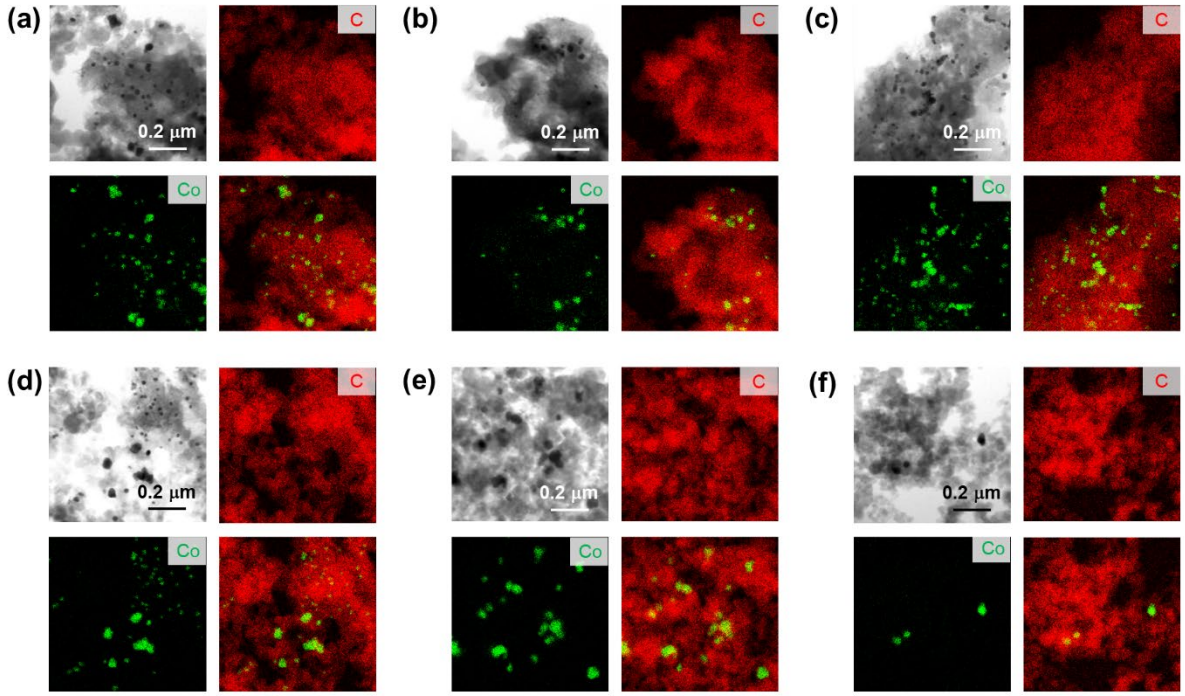

Figure 2-8. BF-STEM, EDX element mapping images of carbon (red) and cobalt (light green), and overlaid STEM images of (a) Co/**1**@VC, (b) Co/**2**@VC, (c) Co/**3**@VC, (d) Co/**4**@VC, (e) Co/**5**@VC, and (f) Co@VC.

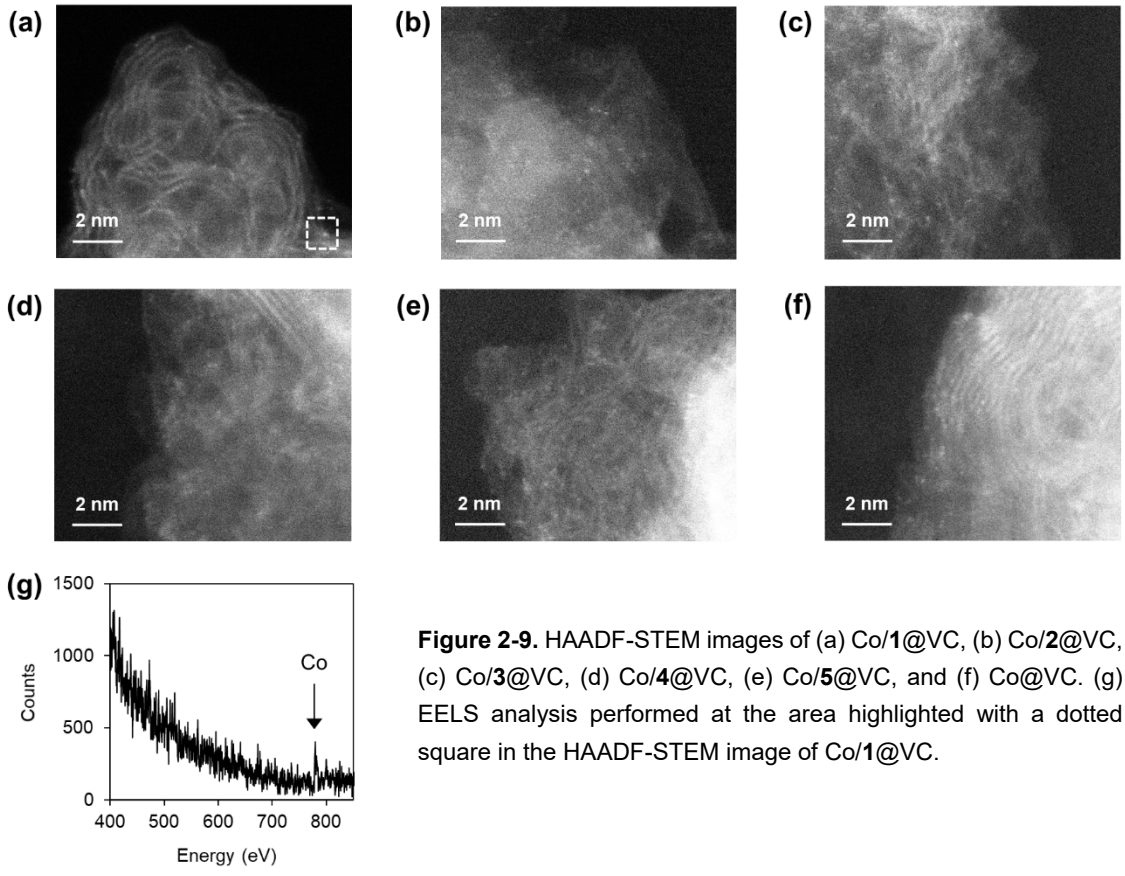

Figure 2-9. HAADF-STEM images of (a) Co/**1**@VC, (b) Co/**2**@VC, (c) Co/**3**@VC, (d) Co/**4**@VC, (e) Co/**5**@VC, and (f) Co@VC. (g) EELS analysis performed at the area highlighted with a dotted square in the HAADF-STEM image of Co/**1**@VC.

Powder X-ray diffraction

To obtain information about the cobalt particles observed by electron microscopic measurements, X-ray diffraction (XRD) analyses (Figure 2-10) were carried out. The broad peaks observed at ca. 26º and 43º in the XRD spectra of Co/**1**@VC, Co/**2**@VC, Co/**3**@VC, Co/**4**@VC, Co/**5**@VC, Co@VC and pyrolyzed carbon support (VC) are typical for amorphous structures of carbon materials. Moreover, the sharp peaks observed at 44.4º and 51.5º correspond to two lattice planes (111) and (101), respectively, of a face-centered-cubic (fcc) phases of cobalt particles.[25] The peak intensities of the cobalt particles in the catalysts prepared from precursors **1**−**5** are significantly less than that of Co@VC, indicating that the precursors suppress the growth of cobalt particles during pyrolysis. These results are matched with the STEM observations.

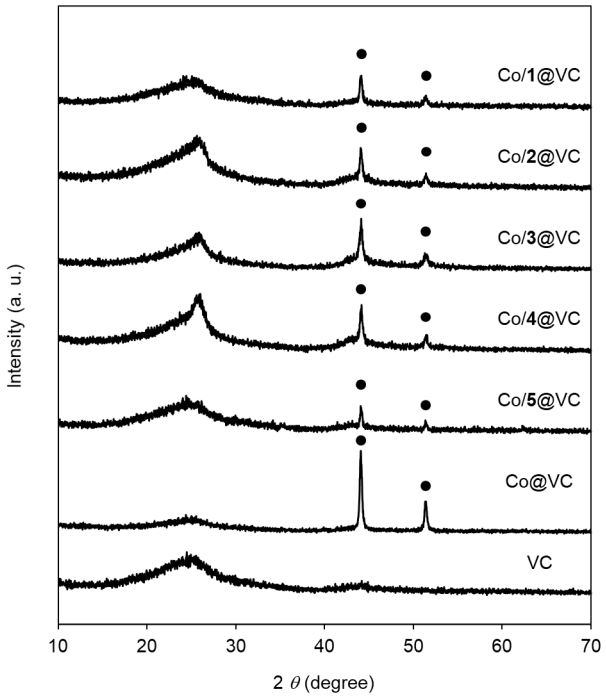

Figure 2-10. XRD patterns of Co/**1**@VC, Co/**2**@VC, Co/**3**@VC, Co/**4**@VC, Co/**5**@VC, Co@VC, and VC. The XRD peaks of bulk Co are marked by filled circle.

Raman spectrometry

The structures of the carbon in the catalysts, Co/**1**@VC, Co/**2**@VC, Co/**3**@VC, Co/**4**@VC, Co/**5**@VC, Co@VC, and pyrolyzed VC were analyzed by Raman spectroscopy (Figure 2-11). The peak appearing near 1360 cm^{-1} is assignable to a D band as seen in disordered carbon structure. In addition, the peak observed near 1580 cm^{-1} is assigned to a G band derived from the in-plane displacement of the carbon strongly coupled in the hexagonal sheets.[43,44] The peak height ratios of D and G bands (I_D/I_G) for the catalysts are approximately 1:1, suggesting that all the catalysts have similar contents of disordered and graphitic structures in the carbon materials.

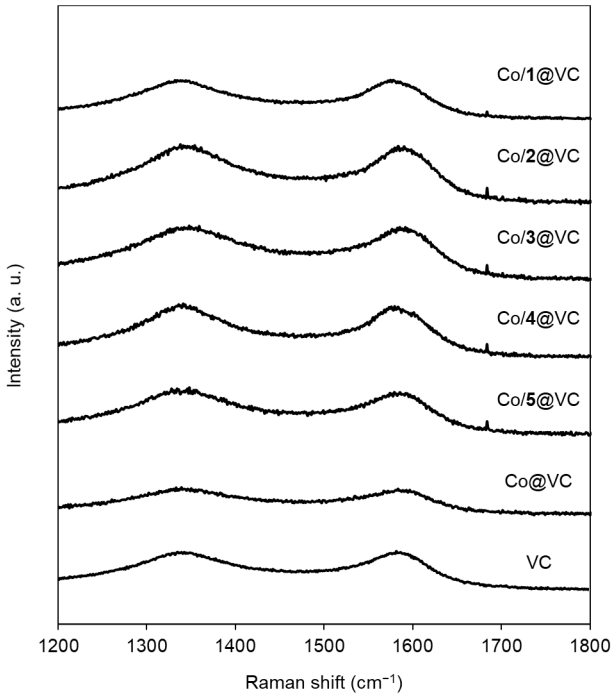

Figure 2-11. Raman spectra of Co/**1**@VC, Co/**2**@VC, Co/**3**@VC, Co/**4**@VC, Co/**5**@VC, Co@VC, and VC.

X-ray photoelectron spectroscopy

The chemical bonding states of nitrogen in the catalysts were analyzed by X-ray photoelectron spectroscopy (XPS) (Figure 2-12). The N1s spectra were deconvoluted into four different nitrogen species which are pyridinic *N* (398.0−398.9 eV), Co−*N* (399.5−400.2 eV), graphitic *N* (400.5−402.0), and *N*-oxide (> 402.0 eV) (Figure 2-12a).[45−48] The proportions of each nitrogen species in the catalysts are summarized in the bar graph (Figure 2-12b). The ratio of the Co−*N* species that form the Co−N_x active sites is clearly higher in Co/**1**@VC (40.2%) and Co/**2**@VC (35.4%) than the other Co/N/C catalysts, Co/**3**@VC (14.8%), and Co/**5**@VC (18.0%). These results suggest that the Co−N_x active sites within the graphitic layer would be efficiently constructed after pyrolysis from thermally durable precursors **1** and **2** containing the nitrogen atoms at the preferable positions to form N2-chelating coordination with a cobalt ion.

Electronic state of the cobalt species in the catalysts were identified by XPS analysis in Co 2p region (Figure 2-13). The peaks at around 780.5 eV and 796.3 eV with two satellite peaks at 785.5 eV and 803.2 eV, respectively, correspond to the characteristic Co $2p_{3/2}$ and Co $2p_{1/2}$ signals of a Co^{2+} species. The peak at around 776 eV is assignable to a Co^0 species.[25,49] While the peaks of Co^{2+} are clearly observed, the peak intensity of Co^0 is very weak. In contrast, the Co^0 particles are clearly observed in STEM images (Figures 2-7 and 2-8). These results indicate that the most of the Co^0 particles in the catalysts are encapsulated by the graphitic layers and embedded inside of the carbon framework (Figure 2-7g).

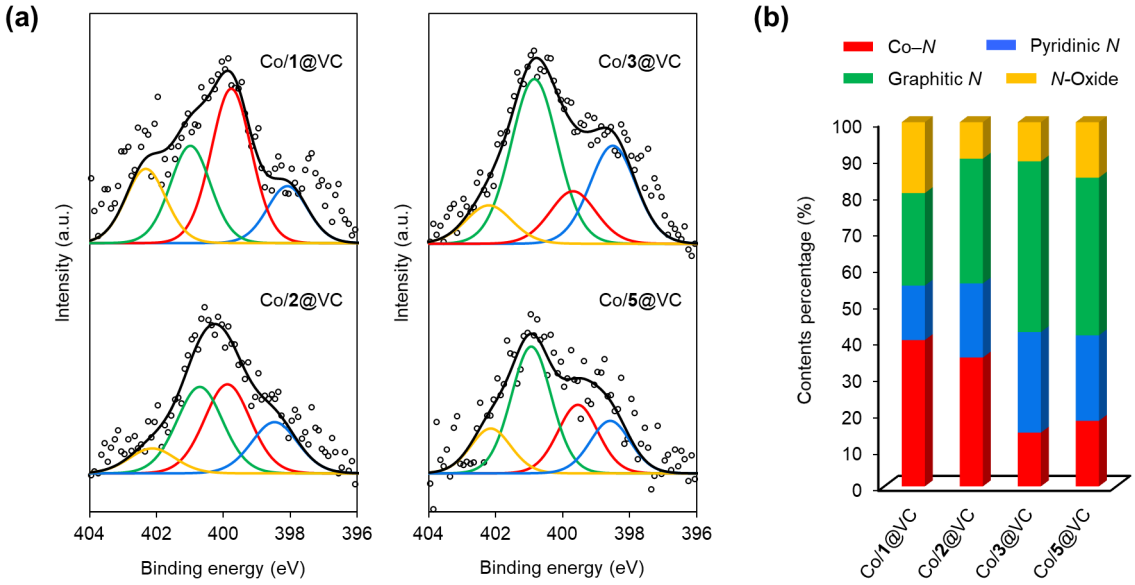

Figure 2-12. (a) XPS N1s spectra of Co/**1**@VC, Co/**2**@VC, Co/**3**@VC and Co/**5**@VC with the simulated peaks of Co−*N* (red), pyridinic *N* (blue), graphitic *N* (green), and *N*-oxide (yellow). (b) Relative ratios of the four nitrogen species.

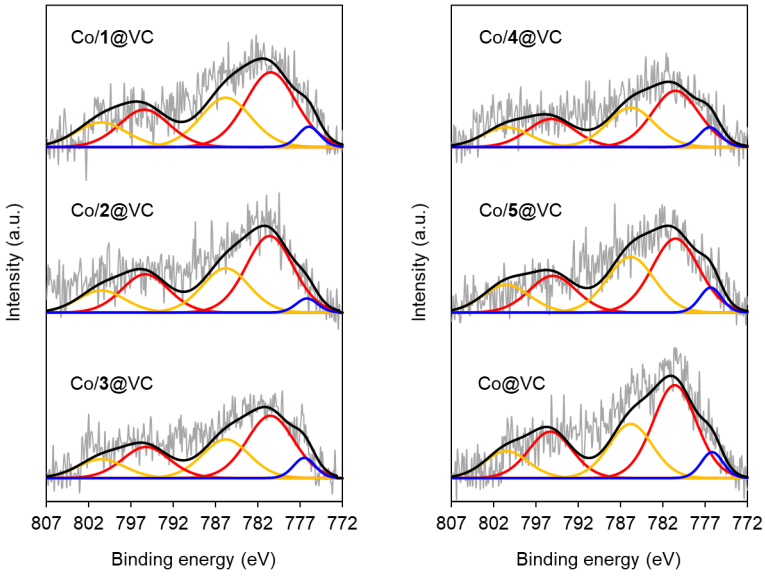

Figure 2-13. XPS Co2p spectra of Co/**1**@VC, Co/**2**@VC, Co/**3**@VC, Co/**4**@VC, Co/**5**@VC, and Co/**1**@VC with the simulated peaks of Co^0 (blue), Co $p_{3/2}$ and Co $p_{1/2}$ (red), and the satellite peaks (yellow).

The content of the cobalt and nitrogen species in the catalysts were quantified by inductively coupled plasma optical emission spectrometry (ICP-OES) measurements and elemental analysis (Table 2-2). The content of the cobalt species in Co/**1**@VC (1.7 wt%), Co/**2**@VC (1.6 wt%), Co/**3**@VC (1.9 wt%), and Co/**4**@VC (2.0 wt%) is lower than that of Co/**5**@VC (2.5 wt%). This is explained by the thermal durability of the precursors. More than 80 wt% of precursors **1**−**4** remain after pyrolysis. Therefore, the content of the cobalt species is relatively lower in the catalysts prepared from polymer precursors **1**−**4** than that of the catalyst prepared from monomer precursor **5**. In contrast, Co/**1**@VC–Co/**3**@VC prepared from polymer precursors **1**−**3** contain more nitrogen atoms than Co/**5**@VC prepared from monomer precursor **5**, although the amounts of the nitrogen in starting materials were fixed to the same value (0.2 mmol). This result indicates that the polymeric structure of precursors **1**−**3** promotes the incorporation of nitrogen atoms into the catalysts during pyrolysis.

The results of characterization and electrocatalytic HER activities of the Co/N/C catalysts are summarized in Table 2-2. The contents of the Co−*N* species which forms the Co−N_x active sites in the Co/N/C catalysts were calculated from the results of XPS and elemental analysis. Significantly large amounts of the Co−*N* species are present in Co/**1**@VC (0.31 wt%) and Co/**2**@VC (0.30 wt%), while there are less Co−*N* species in Co/**3**@VC (0.12 wt%) and Co/**5**@VC (0.06 wt%). Importantly, the contents of the Co−*N* species are found to clearly correlate with the performance in the electrocatalytic HER. The HER activities and the contents of Co−*N* species of Co/**1**@VC and Co/**2**@VC are almost same, suggesting that the Co−N_x active sites with the similar chemical structure are constructed in both catalysts although precursors **1** and **2** contain the different types of nitrogen atoms. These results suggest that the efficient formations of the Co−N_x active sites can be achieved by employing precursor **1** or **2** for preparation of the Co/N/C catalysts to improve the HER activity.

It has been well studied that the cobalt particles also have a catalytic activity for HER.[25] Co/**4**@VC containing the cobalt particles with an average size of 19 nm has slightly higher activity than Co@VC which has the cobalt particles with an average size of 42 nm, suggesting that the size of cobalt particles would affect the catalytic performance in HER. However, the HER activities of Co/**4**@VC and Co@VC which have no Co−N_x sites are clearly less than those of Co/**1**@VC−Co/**3**@VC. In addition, STEM observations and XPS measurements revealed that the cobalt particles in the catalysts are encapsulated by the graphitic layer (Figures 2-7g and 2-13). Therefore, the contribution of the cobalt particles for catalyzing HER in the catalysts is less than that of the Co−N_x sites.

Table 2-2. Summary of Characterizations and HER Activities of the Catalysts.

Catalysts		Co/**1**@VC	Co/**2**@VC	Co/**3**@VC	Co/**4**@VC	Co/**5**@VC	Co@VC
Thermal gravimetries							
T_D[a]	ºC	545	530	550	560	335	–
Weight loss[b]	wt%	16	17	14	20	92	–
Elemental analysis							
Co[c]	wt%	1.7	1.6	1.9	2.0	2.5	1.4
N	wt%	0.8	0.8	0.8	0.1	0.3	0.2
C	wt%	86.3	86.4	88.8	92.4	92.6	92.7
H	wt%	0.4	0.4	0.8	0.1	0.4	0.3
XPS (N1s)							
Co–*N*	wt%[d]	0.31	0.30	0.12	–	0.06	–
	%	40.2	35.4	14.8	–	18.0	–
Pyridinic *N*	%	15.0	20.3	27.6	–	25.5	–
Graphitic *N*	%	25.3	34.2	16.9	–	43.3	–
N-oxide	%	19.5	10.0	10.8	–	15.2	–
Electrochemical measurements							
MSD[e]	10^{19} sites·g_{cat}^{-1}	4.3	3.5	1.9	0.7	0.9	0.8
Overpotential[f]	mV	311	315	387	459	458	539
Tafel slope[g]	mV·dec^{-1}	128	125	176	169	135	220

[a]Thermal decomposition temperature and [b] and weight loss at 700 ºC of the precursors determined by TG analysis. [c]Determined by ICP-OES. [d]Calculated from the results of XPS and elemental analysis. [e]Evaluated from the cyclic voltammetry. [f]Overpotential at I = 10 mA·cm^{-2}. [g]Determined by the polarization curves.

2-3. Summary

The author demonstrates the preparation of the Co/N/C catalysts by pyrolysis of precursors forming N-doped graphene nanoribbon (N-GNR), cobalt ion, and Vulcan® XC-72R as a carbon support. The polymers of the substituted triphenylene, which have nitrogen atoms at precise positions, were employed as the precursors of the Co/N/C catalysts. These precursors were found to form the N2-chelating coordination sites with a cobalt ion along with the GNR framework, which would be incorporated into the graphene layer of the Co/N/C catalysts pyrolyzed at 1000 ºC. In fact, the Co/N/C catalysts, Co/**1**@VC and Co/**2**@VC that contain large amounts of the Co−*N* species exhibit the improved HER activities. Co/**1**@VC has the minimum overpotentials of 311 mV in 0.1 M $HClO_{4aq}$ at 10 mA·cm^{-2} in the catalysts, as shown in this chapter. This preparation method is useful for the construction of highly active Co−N_x active sites derived from the precursors forming the N-GNR structures in the Co/N/C catalysts. This work provides a new direction to design a precursor in order to achieve efficient construction of the active sites in the Co/N/C catalysts which serve an enhanced catalytic performance in HER.

2-4. Experimental Section

Materials and methods

All reagents were used without purification. All solvents were dried with molecular sieves 3Å before use. ^{1}H NMR and ^{13}C NMR spectra were recorded on a Bruker BioSpin DPX400 NMR spectrometer (400 MHz). ESI-TOF MS analyses were performed on a Bruker micrOTOF focus III mass spectrometer. The values of thernally decomposition temperature (T_d) of the precursors were determined by thermogravimetry analysis (TGA) using a Mac Science TG-DTA TMA DSC with a heating rate of 10 ºC·min^{-1} in an N_2 stream on platinum pan. The morphologies of the catalysts and their elemental mapping images were investigated by scanning electron microscopy (SEM) using JEOL JSM-7600F equipped with an energy-dispersive X-ray spectroscope (EDX). SEM images, annular dark field scanning transmission electron microscopic (ADF-STEM) images, and bright field scanning transmission electron microscopic (BF-STEM) images in the same field of view of the catalysts were collected by scanning transmission electron microscope (STEM) using HITACHI HD-2000. Image analyses to estimate the average particle radius in the Co/N/C catalysts were performed by ImageJ.[50] The atomically dispersed cobalt atoms in the catalysts were observed by high-angle annular dark field aberration-corrected scanning transmission electron microscopy (HAADF-STEM) using JEOL JEM-ARM200F equipped with an electron energy loss spectroscopy (EELS). X-ray diffraction (XRD) spectra were measured with Bruker D2 PHASER 2nd Generation with CuKα radiation. Raman spectra were obtained using a JASCO NRS3100 instrument with a 532 nm laser. Contents of cobalt species in each catalyst were determined by inductively coupled plasma optical emission spectroscopy (ICP-OES) using a SHIMAZDU ICPS-7510 system. The elemental analysis of carbon, hydrogen and nitrogen was performed on JM10 (J-SCIENCE LAB Co., Ltd.).

Synthesis of the precursors

The procedures for the synthesis of polymeric precursors **1**−**4** and monomeric precursor **5** are described in the chapter 1.

Preparation of the catalysts

Carbon black Vulcan® XC-72R (VC, Cabot, USA) was used as a carbon support. Electrocatalysts were prepared from precursors, cobalt ions and VC by pyrolysis in N_2 flow. The electrocatalysts, which are abbreviated as Co/**precursor**@VC, were prepared as follows: precursors (0.1 mmol) dissolved in $CHCl_3$ (50 mL) and $CoCl_2{\cdot}6H_2O$ (23.8 mg, 0.1 mmol) dissolved in methanol (10 mL) were mixed and then powders of VC (33.3 mg) were added to the mixture. The suspension was vigorously vortexed and sonicated for 30 min. After removal of the solvents, the residue was placed on an alumina boat (length: 80 mm, width: 16 mm, height: 10 mm), and then inserted into a quartz tube (diameter 50 mm, length 800 mm). The quartz tube was installed in a hinge split tube furnace (Koyo Thermo Systems Co. Ltd., KTF045N1). The residue was preheated from ambient temperature to 300 ºC for 1 h under N_2 flow (0.2 $L{\cdot}min^{-1}$), and incubated for 2 h. The obtained materials were then immediately heated to 1000 ºC for 1 h and incubated for 2 h. The temperature inside the quartz tube of the furnace was recorded by a thermocouple equipped with a data logger (CHINO Corporation, MC3000). After cooling, the pyrolyzed catalyst was ground and incubated in a 0.5 M H_2SO_4 solution at 80 ºC for 3 h to leach out impurities and then washed with excess volumes of deionized water. The dried carbon catalyst was used for the experiments. Co@VC was obtained using the same protocol without the addition of any precursors.

Electrochemical measurements

The performance of the catalyst in HER was evaluated in an N_2-purged 0.1 M $HClO_{4aq}$ solution. A rotating disk electrode (RDE) with a glassy carbon disk electrode (ϕ = 5 mm) was utilized for the electrochemical measurements. Electrode rotation rates were controlled using a Pine Instruments AFMSRCE rotator with a Pine MSRX motor controller. An electrode was polished to mirror flat with alumina powder (50 nm) before use. The catalyst ink was prepared with 4.0 mg of catalyst and 100 μL of 5 wt% Nafion® (Sigma–Aldrich) in a mixture of lower aliphatic alcohols and H_2O. The ink was vortexed and sonicated in an ultrasonic bath at 100 W at 35 kHz for 30 min. Then, 2 μL of catalyst ink was loaded onto the surface of the electrode and dried. Electrochemical tests were performed with a potentiostat (ALS, electrochemical analyzer model 610B) using a typical three-electrode system, with platinum wire as a counter electrode and Ag/AgCl as a reference electrode. The potential difference between Ag/AgCl and RHE was calculated, and the value is 0.258 V in a 0.1 M $HClO_{4aq}$ solution. The scan rate was 5 $mV{\cdot}s^{-1}$ from −0.858 to −0.253 V vs. the Ag/AgCl reference electrode. Before each potential scan, the electrolyte of the 0.1 M $HClO_{4aq}$ solution was saturated with N_2 for at least 30 min, and N_2 purging was continued during the electrochemical

experiments. The overpotentials for HER are defined as a potential showing $j = -10$ mA·cm^{-2} in RDE measurement, where j represents the current density. MSD (mass-based site density) corresponding to the number of the redox active cobalt species, which would be Co−N_x active species, in the catalysts normalized by mass of the catalyst (site·g^{-1}) was evaluated by the cyclic voltammetry (CV) in an N_2-saturated 0.1 M $HClO_{4aq}$ solution at 10 mV·s^{-1} at 2000 rpm from −0.258 to 0.742 V versus the Ag/AgCl reference electrode (Figure 2-6) and calculated by the following equation:

$$MSD = Q/(e \times n \times g_{cat})$$

where Q represents $Co^{2+/3+}$ coulombic charge (C) calculated by the CV in an N_2-saturated solution, n is reaction number (n = 1 in this redox system), and g_{cat} is loaded weight of the catalyst (0.08 mg).

References and Notes

[1] J. A. Turner, *Science*, **2004**, *305*, 972−974.

[2] J. Zhu, L. Hu, P. Zhao, L. Y. S. Lee, K. Y. Wong, *Chem*. *Rev*. **2020**, *120*, 851−918.

[3] H. Wang, J. Li, K. Li, Y. Lin, J.Chen, L. Gao, V. Nicolosi, X. Xiao, J. M. Lee, *Chem*. *Soc*. *Rev*. **2021**, *50*, 1354−1390.

[4] D. Kong, H. Wang, Z. Lu, Y. Cui, *J*. *Am*. *Chem*. *Soc*. **2014**, *136*, 4897−4900.

[5] X. Hou, H. Zhou, M. Zhao, Y. Cai, Q. Wei, *ACS Sustainable Chem*. *Eng*. **2020**, *8*, 5724−5733.

[6] S. Y. S. Jaberi, A. Ghaffarinejad, Z. Khajehsaeidi, *Int*. *J*. *Hydrogen Energy* **2021**, *46*, 3922−3932.

[7] B. Cao, G. M. Veith, J. C. Neuefeind, R. R. Adzic, P. G. Khalifah, *J*. *Am*. *Chem*. *Soc*. **2013**, *135*, 19186−19192.

[8] C. Wan, Y. N. Regmi, B. M. Leonard, *Angew*. *Chem*. *Int*. *Ed*. **2014**, *126*, 6525−6528.

[9] Q. Gong, Y. Wang, Q. Hu, J. Zhou, R. Feng, P. N. Duchesne, P. Zhang, F. Chen, N. Han, Y. Li, C. Jin, Y. Li, S. T. Lee, *Nat*. *Commun*. **2016**, *7*, 13216.

[10] Y. Shi, B. Zhang, *Chem*. *Soc*. *Rev*. **2016**, *45*, 1529−1541.

[11] X. Wang, J. He, B. Yu, B. Sun, D. Yang, X. Zhang, Q. Zhang, W. Zhang, L. Gu, Y. Chen, *Appl*. *Catal*. *B: Environ*. **2019**, *258*, 117996.

[12] H. Wang, Y. Lin, S. Liu, J. Li, L. Bu, J. Chen, X. Xiao, J. H. Choi, L. Gao, J. M. Lee, *J*. *Mater*. *Chem*. *A* **2020**, *8*, 7109−7116.

[13] H. Wang, X. Xiao, S. Liu, C. L. Chiang, X. Kuai, C. K. Peng, Y. C. Lin, X. Meng, J. Zhao, J. Choi, Y. G. Lin, J. M. Lee, L. Gao, *J*. *Am*. *Chem*. *Soc*. **2019**, *141*, 18578−18584.

[14] S. Cobo, J. Heidkamp, P. A. Jacques, J. Fize, V. Fourmond, L. Guetaz, B. Jousselme, V. Ivanova, H. Dau, S. Palacin, M. Fontecave, V. Artero, *Nat*. *Mater*. **2012**, *11*, 802−807.

[15] E. S. Andreiadis, P. A. Jacques, P. D. Tran, A. Leyris, M. Chavarot-Kerlidou, B. Jousselme, M. Matheron, J. Pécaut, S. Palacin, M. Fontecave, V. Artero, *Nat*. *Chem*. **2013**, *5*, 48−53.

[16] N. Kaeffer, M. Chavarot-Kerlidou, V. Artero, *Acc*. *Chem*. *Res*. **2015**, *48*, 1286−1295.

[17] C. Zhu, S. Fu, Q. Shi, D. Du, Y. Lin, *Angew*. *Chem*. *Int*. *Ed*. **2017**, *56*, 13944−13960.

[18] M. D. Hossain, Z. Liu, M. Zhuang, X. Yan, G. L. Xu, C. A. Gadre, A. Tyagi, I. H. Abidi, C. J. Sun, H. Wong, A. Guda, Y. Hao, X. Pan, K. Amine, Z. Luo, *Adv*. *Energy Mater*. **2019**, *9*, 1803689.

[19] S. Gupta, D. Tryk, I. Bae, W. Aldred, E. Yeager, *J*. *Appl*. *Electrochem*. **1989**, *19*, 19−27.

[20] H. W. Liang, S. Brüller, R. Dong, J. Zhang, X. Feng, K. Müllen, *Nat*. *Commun*. **2015**, *6*, 7992.

[21] H. Fei, J. Dong, M. J. Arellano-Jiménez, G. Ye, N. D. Kim, E. L. G. Samuel, Z. Peng, Z. Zhu, F. Qin, J. Bao, M. J. Yacaman, P. M. Ajayan, D. Chen, J.M. Tour, *Nat*. *Commun*. **2015**, *6*, 8668.

[22] L. Zhang, W. Liu, Y. Dou, Z. Du, M. Shao, *J*. *Phys*. *Chem*. *C* **2016**, *120*, 29047−29053.

[23] Y. Tong, X. Yu, H. Wang, B. Yao, C. Li, G. Shi, *ACS Catal*. **2018**, *8*, 4637−4644.

[24] H. Wang, N. Yang, W. Li, W. Ding, K. Chen, J. Li, L. Li, J. Wang, J. Jiang, F. Jia, Z. Wei, *ACS Energy Lett*. **2018**, *3*, 1345−1352.

[25] Y. J. Sa, S. O. Park, G. Y. Jung, T. J. Shin, H. Y. Jeong, S. K. Kwak, S. H. Joo, *ACS Catal*. **2019**, *9*, 83−97.

[26] H. Fei, J. Dong, D. Chen, T. Hu, X. Duan, I. Shakir, Y. Huang, X. Duan, *Chem*. *Soc*. *Rev*. **2019**, *48*, 5207−5241.

[27] D. Lyu, Y. Du, S. Huang, B. Y. Mollamahale, X. Zhang, S. W. Hasan, F. Yu, S. Wang, Z. Q. Tian, P. K. Shen, *ACS Appl*. *Mater*. *Interfaces* **2019**, *11*, 39809−39819.

[28] C. F. Li, J. W. Zhao, L. Q. Wu, G. R. Li, *Appl*. *Catal*. *B: Environ*. **2021**, *282*, 119463.

[29] X. Zhou, H. Yu, Y. Liu, Y. Kong, Y. Tao, Y. Qin, *RSC Adv*. **2019**, *9*, 33997−34003.

[30] L. Song, J. Chang, Y. Ma, X. Tan, Y. Xu, L. Guo, Z. Chen, T. Zhao, Y. Li, Y. Liu, Y. Zhang, W. Chu. *RSC Adv*. **2020**, *10*, 43248−43255.

[31] H. L. Jia, J. Zhao, L. Gu, Z. J. Peng, Z. L. Bao, X. L. Sun, M. Y. Guan, *Sustainable Energy Fuels* **2020**, *4*, 6165−6173.

[32] K. Matsumoto, A. Onoda, T. Kitano, T. Sakata, H. Yasuda, S. Campidelli, T. Hayashi, *ACS Appl*. *Mater*. *Interfaces* **2021**, *13*, 15101−15112.

[33] J. Cai, P. Ruffieux, R. Jaafar, M. Bieri, T. Braun, S. Blankenburg, M. Muoth, A. P. Seitsonen, M. Saleh, X. Feng, K. Müllen, *Nature*, **2010**, *466*, 470−473.

[34] T. H. Vo, M. Shekhirev, D. A. Kunkel, M. D. Morton, E. Berglund, L. Kong, P. M. Wilson, P. A. Dowben, A. Enders, A. Sinitskii, *Nat*. *Commun*. **2014**, *5*, 3189.

[35] J. Cai, C.A. Pignedoli, L. Talirz, P. Ruffieux, H. Söde, L. Liang, V. Meunier, R. Berger, R. Li, X. Feng, K. Müllen, R. Fasel, *Nat*. *Nanotechnol*. **2014**, *9*, 896−900.

[36] T. H. Vo, U. G. E. Perera, M. Shekhirev, M. M. Pour, D. A. Kunkel, H. Lu, A. Gruverman, E. Sutter, M. Cotlet, D. Nykypanchuk, P. Zahl, A. Enders, A. Sinitskii, P. Sutter, *Nano Lett*. **2015**, *15*, 5770−5777.

[37] Z. Chen, W. Zhang, C. A. Palma, A. L. Rizzini, B. Liu, A. Abbas, N. Richter, L. Martini, X. Y. Wang, N. Cavani, H. Lu, N. Mishra, C. Coletti, R. Berger, F. Klappenberger, M. Kläui, A. Candini, M. Affronte, C. Zhou, V. D. Renzi, U. Pennino, J. V. Barth, H. J. Räder, A. Narita, X. Feng, K. Müllen, *J*. *Am*. *Chem*. *Soc*. **2016**, *138*, 15488−15496.

[38] X. Y. Wang, X. Yao, A. Narita, K. Müllen, *Acc*. *Chem*. *Res*. **2019**, *52*, 2491−2505.

[39] Y. Tanaka, A. Onoda, S. Okuoka, T. Kitano, K. Matsumoto, T. Sakata, H. Yasuda, T. Hayashi, *ChemCatChem* **2018**, *10*, 743−750.

[40] A. Onoda, Y. Tanaka, K. Matsumoto, M. Ito, T. Sakata, H. Yasuda, T. Hayashi, *RSC Adv*. **2018**, *8*, 2892−2899.

[41] M. Zeng, Y. Li, *J*. *Mater*. *Chem*. *A* **2015**, *3*, 14942−14962.

[42] S. Yasuda, Y. Uchibori, M. Wakeshima, Y. Hinatsu, H. Ogawa, M. Yano, H. Asaoka, *RSC Adv*. **2018**, *66*, 37600−37605.

[43] Y. Wang, D. C. Alsmeyer, R. L. McCreery, *Chem*. *Mater*. **1990**, *2*, 557−563.

[44] T. Jawhari, A. Roid, J. Casado, *Carbon* **1995**, *33*. 1561−1565.

[45] Y. Du, H. Chen. Z. Huang, X. He, W. Fang, W. Li, L. Zhao, *ACS Appl*. *Energy Mater*. **2020**, *3*, 687−694.

[46] Q. Jim, B. Ren, H. Cui, C. Wang, *Appl*. *Catal*. *B: Environ*. **2021**, *283*, 119643.

[47] R. Wang, P. Zhang, Y. Wang, Y. Wang, K. Zaghib, Z. Zhou, *Prog*. *Mater*. *Sci*. **2020**, *30*, 855−860.

[48] Y. Ha, B. Fei, X. Yan, H. Xu, Z. Chen, L. Shi, M. Fu, W. Xu, R. Wu, *Adv*. *Energy Mater*. **2020**, *10*, 2002592.

[49] T. Cao, X. Dai, F. Li, W. Liu, Y. Bai, Y. Fu, W. Qi, *ChemCatChem*, **2021**, *13*, 3067−3073.

[50] C. A. Schneider, W. S. Rasband, K. W. Eliceiri, *Nat*. *Methods* **2012**, *9*, 671−675.

Chapter 3

One-step Preparation of Fe/N/C Single-atom Catalysts Containing $Fe-N_4$ Active Sites from an Iron Complex with Ligands Forming Nanographenes

Reproduced in part with permission from [*Chem*. *Eur*. *J*. **2021**, *27*, 1−6]
DOI: 10.1002/chem.202103545

3-1. Introduction

Development of non-precious metal catalysts for the oxygen reduction reaction (ORR) has been demanded for widespread use of environmentally friendly devices such as metal-air batteries and fuel cells.[1,2] M/N/C single-atom catalysts (M/N/C catalysts) have been investigated in this context because of their high catalitic activity toward ORR and durability. These catalysts contain atomically dispersed 3d-transition metal atoms as the active sites with coordinating nitrogen atoms, $M-N_x$ sites, in carbon materials.[3,4] In particular, Fe/N/C catalysts are known to have superior characteristics in the catalytic activity, durability, and utilization efficiency of metal atoms.[5−8]

The Fe/N/C catalysts with atomically dispersed $Fe-N_x$ sites have been prepared from a variety of precursors by a high-temperature pyrolytic treatment.[9,10] The $Fe-N_x$ active sites embedded within graphitic layer are constructed from precursors containing iron and nitrogen atoms during pyrolysis. An ideal precursor is thus needed for efficiently and precisely constructing $Fe-N_x$ sites. Precursors such as iron complexes combined with support materials[11−15] and nitrogen-containing polymers with iron salts[16−18] have been investigated to be graphitized during pyrolysis in the range of 700−1100 ºC, generating thermodynamically stable $Fe-N_x$ sites in graphitic layers. Concomitantly, iron atoms are also sintered and aggregated. As a result, iron aggregates such as iron oxides, iron carbides, and bulk iron particles covered with carbon shells are generated as byproducts.[19,20] These unfavorable and less active iron species were, therefore, leached out by an acid washing process under harsh conditions, although this process damages the carbon structure of the catalysts. (Figure 3-1a).[21,22] It has been recently reported that the $Fe-N_x$ sites can be efficiently constructed by employing an iron co-doped zeolitic imidazolate framework (ZIF-8) as a precursor, which is capable of isolation of iron atoms within a 3D network of ZIF-8 and prevention of the aggregation of iron atoms during pyrolysis.[23,24] However, other successful examples for constructing the $Fe-N_x$ sites without forming the iron byproducts have been still limited.[25]

A method to prepare Fe/N/C catalysts using a polymer precursor with preorganized pyridine and phenyl rings in triphenylene units was described in the chapter 1.[26] The aromatic rings were then intramolecularly annulated during pyrolysis to efficiently construct Fe–N_x sites along the structure of the graphene nanoribbon, although the iron aggregates were found to be formed to some extent. The author thus envisioned the construction of the Fe–N_4 sites in the Fe/N/C catalysts in a highly efficient manner using new iron complex precursors with 5,6,7,8-tetraphenyl-1,12-diazatripheneylene ligands containing bromo substituents. In the newly designed ligands, the nitrogen atoms in the aromatic plane can strongly bind the iron ion. At high temperature, the C–Br bonds are cleaved in a homolytic manner, generating the radical species at the periphery of the ligands. Thereby the graphitization of the ligands is promoted. Notably, the preorganized aromatic rings assist the formation of the thermodynamically stable nanographene structures of hexabenzocoronene capable of N2-coordination, which protect the iron center under pyrolytic conditions. Consequently, the iron complex precursors were converted to the Fe–N_4 sites with perfect suppression of the iron aggregation. In this chapter, the author descrives that the Fe/N/C catalysts with the Fe–N_4 sites which catalyze ORR can be prepared from the iron complex precursors containing the 5,6,7,8-tetraphenyl-1,12-diazatriphenylene ligands by one-step pyrolysis without requiring an acid washing process (Figure 3-1b).

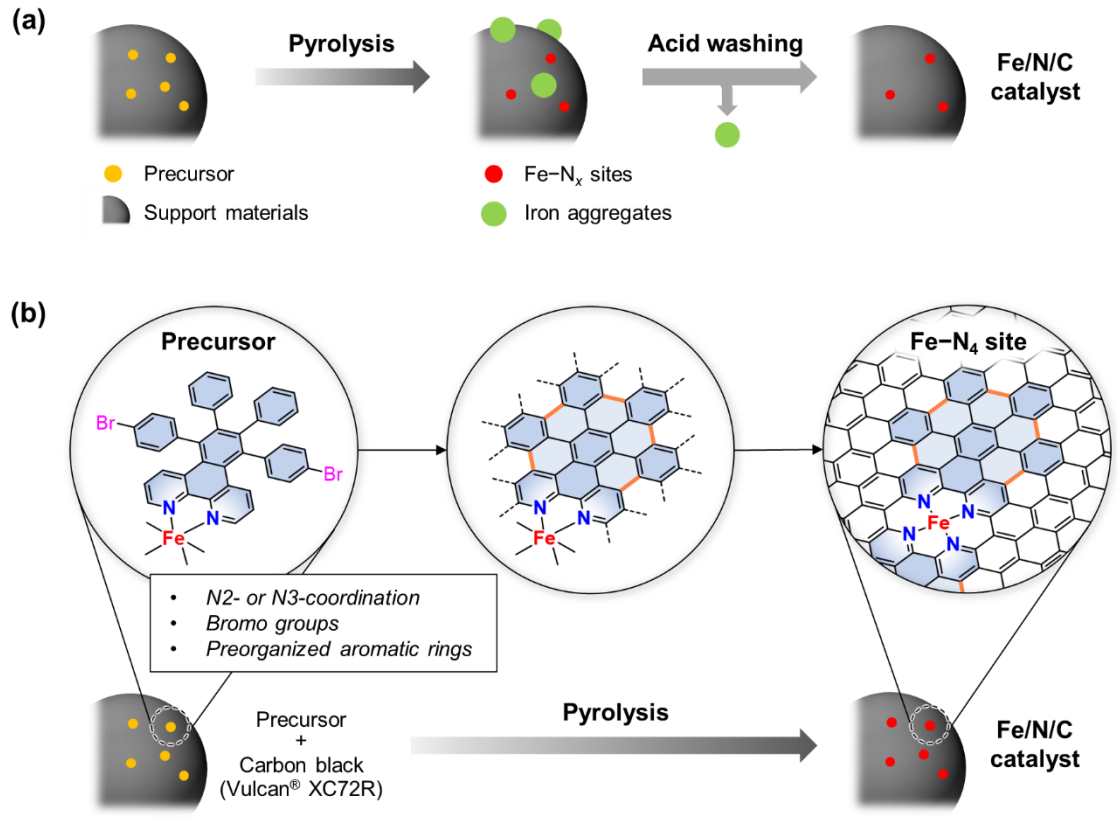

Figure 3-1. Schematic illustrations of the preparation of Fe/N/C catalysts in (a) the general high-temperature pyrolysis method and (b) the one-step pyrolysis method described in the chapter 3.

3-2. Results and Discussion

Design and synthesis of precursors

The author designed and synthesized the 5,8-di(*p*-bromophenyl)-6,7-diphenyl-1,12-diazatripheneylene derivatives, **L1**, **L2**, and **L3**. (Figure 3-2). **L1** and **L2** contain an N2- and N3-chelating coordination structure, respectively, to strongly bind an iron ion. As a reference sample, **L3**, which includes phenyl rings at the 2 and 11 positions and does not form a stable iron complex due to the steric hindrance, was prepared to investigate the importance of strong Fe−N coordination in the precursor. In addition, 5,6,7,8-tetraphenyl-1,12-diazatripheneylene (**L4**), 3,8-dibromo-1,10-phenanthroline (**L5**), and 1,10-phenanthroline (**L6**), were employed to verify the contribution of the bromo substituents and the preorganized aromatic rings within the diazatripheneylene framework for the construction of the active sites.

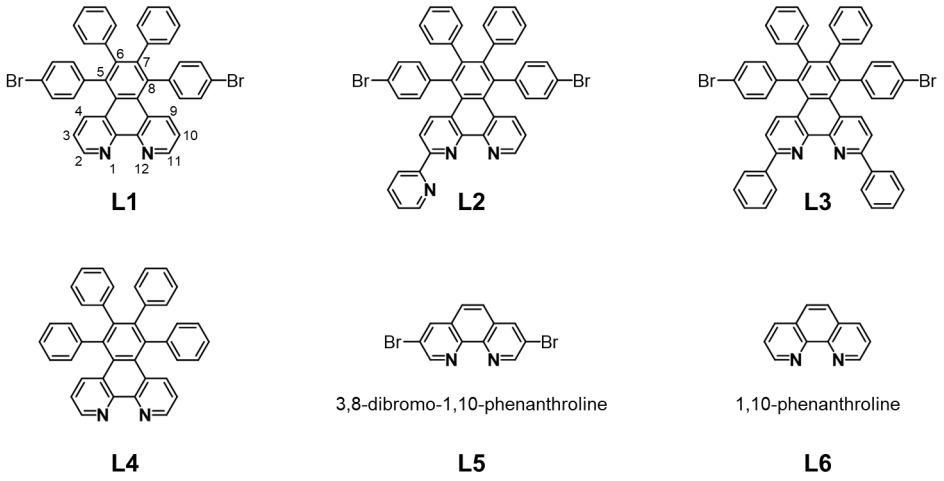

Figure 3-2. Chemical structures of the ligands used as the precursors for preparing Fe/N/C catalysts.

Thermal stabilities of **L1**−**L6** were evaluated from the thermal decomposition temperatures (T_d) and the mass loss values of the ligands under the pyrolysis condition, which were determined by thermogravimetric analysis (TGA) (Figures 3-3). The results are listed in Table 3-1. The 5,6,7,8-tetraaryl-diazatriphenylene ligands **L1**−**L4** have higher T_d values than those of **L5** and **L6**. Importantly, the mass loss values of **L1**−**L3** are significantly lower, while essentially 100% of the mass of **L4**−**L6** was lost by thermal decomposition or sublimation. The remaining masses of **L1**−**L3** correspond to the mass of diazahexabenzocoronene without the substituents. These results suggest that thermally durable nanographenes are generated from the ligands **L1**−**L3** during pyrolysis under the assistance of the preorganized aromatic rings and C−C coupling via the C−Br bond cleavage as planned by design.

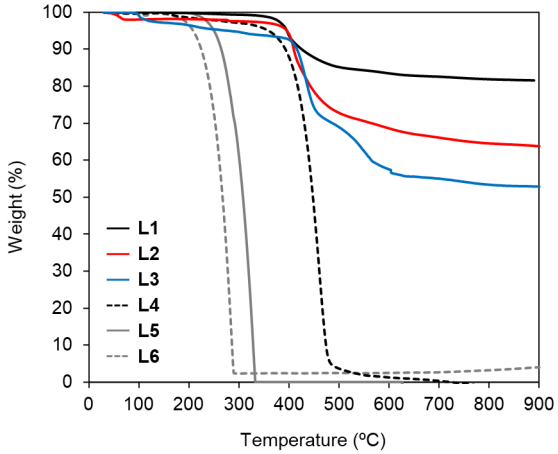

Figure 3-3. Thermal gravimetric analysis curves of **L1** (black solid line), **L2** (red solid line), **L3** (blue solid line), **L4** (black dashed line), **L5** (gray solid line), and **L6** (gray dashed line).

Table 3-1. Results of TG Measurements.

Precursor	T_D[a] (ºC)	Weight loss[b] (%)
L1	390	20
L2	400	35
L3	410	45
L4	385	99
L5	220	99
L6	200	97

[a]Thermal decomposition temperature values. [b]Weight loss values near the decomposition temperature.

The iron complexes containing **L1**, **L2**, **L4**, **L5**, and **L6**, respectively, were synthesized as the precursors of Fe/N/C catalysts. The obtained Fe(II) complexes, $[Fe(\mathbf{L1})_3]^{2+}$, $[Fe(\mathbf{L2})_2]^{2+}$, $[Fe(\mathbf{L4})_3]^{2+}$, $[Fe(\mathbf{L5})_3]^{2+}$, and $[Fe(\mathbf{L6})_3]^{2+}$, were characterized by UV-Vis absorption spectroscopy (shown in experimental section). In addition, X-ray crystallography revealed that $[Fe(\mathbf{L1})_3]^{2+}$, $[Fe(\mathbf{L2})_2]^{2+}$, and $[Fe(\mathbf{L4})_3]^{2+}$ have an octahedral geometry (Figure 3-4).[27] Ligand **L3**, in which the coordination site is sterically hindered by two adjacent phenyl groups, did not provide the corresponding iron complex. In fact, the tyipical absorption assigned to metal-ligand charge transfer (MLCT) is not observed in UV-Vis spectrum of **L3** before and after the addition of iron ions. Therefore, the mixture of **L3** and iron salts was utilized as a precursor.

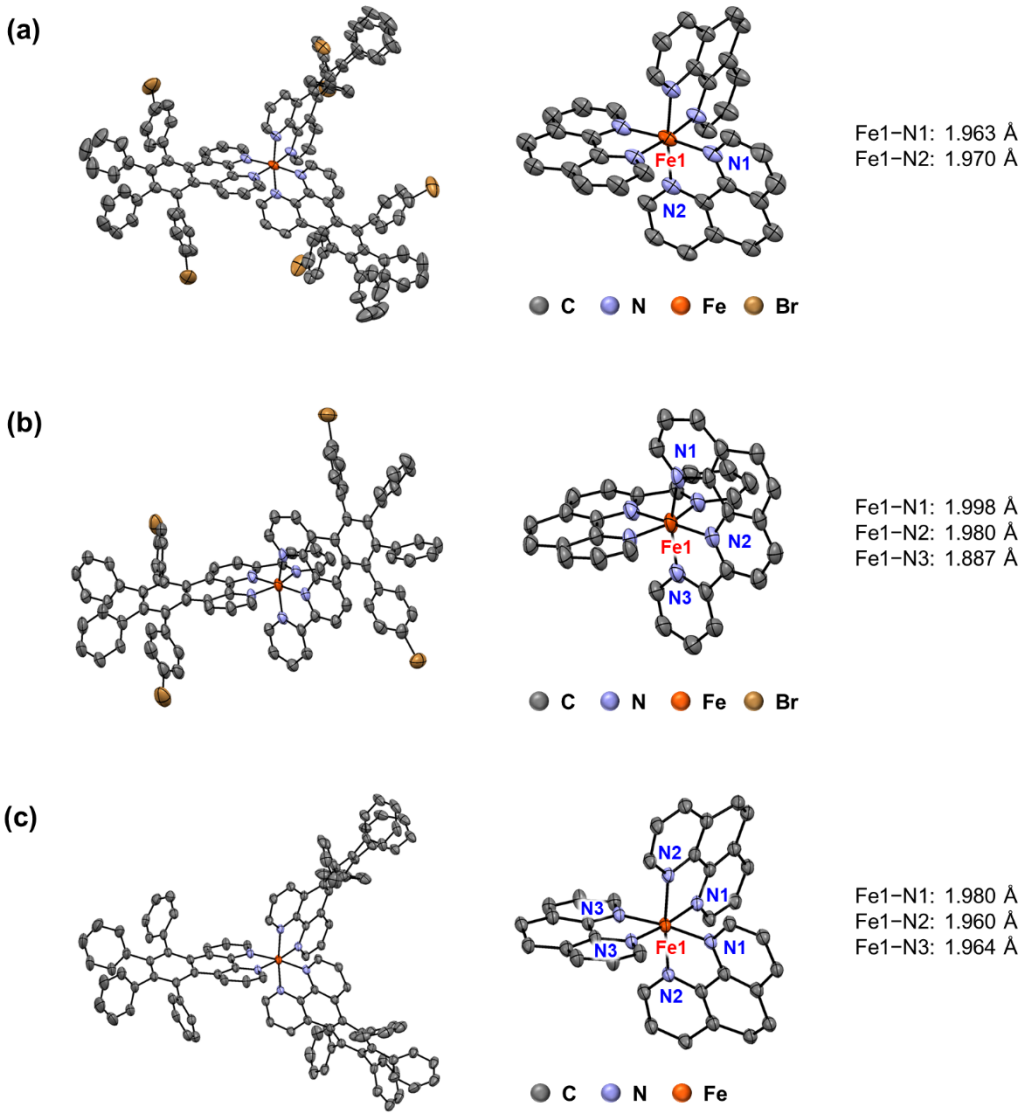

Figure 3-4. X-ray crystal structures of (a) $[Fe(\mathbf{L1})_3]^{2+}$, (b) $[Fe(\mathbf{L2})_2]^{2+}$, and (c) $[Fe(\mathbf{L4})_3]^{2+}$ with 50% thermal ellipsoid probability (hydrogen atoms, solvents, and non-bonding counter anion ClO_4^- are omitted for clarity.). Enlarged views of the iron complexes are shown on the right side.

Preparation of the Fe/N/C catalysts

The Fe/N/C catalysts were prepared from the iron complex precursors, $[Fe(\mathbf{L1})_3]^{2+}$, $[Fe(\mathbf{L2})_2]^{2+}$, $[Fe(\mathbf{L4})_3]^{2+}$, $[Fe(\mathbf{L5})_3]^{2+}$, $[Fe(\mathbf{L6})_3]^{2+}$, or the mixture of **L3** and iron salts. In brief, the precursor (0.05 mmol) was combined with carbon black (Vulcan® XC72R, VC) (100 mg), and the mixture was pyrolyzed at 700 ºC for 2 h. After cooling to room temperature, the Fe/N/C catalysts denoted as Fe/**L1**@VC, Fe/**L2**@VC, Fe/**L3**@VC, Fe/**L4**@VC, Fe/**L5**@VC, and Fe/**L6**@VC were obtained without performing an acid washing treatment. Although the results of TG analyses indicate that the ligands **L4**–**L6** are thermally decomposed or sublimed over 300 °C, these precursors are capable to form the active sites and be remained when they are pyrolyzed in the presence of VC.

Characterizations of the Fe/N/C catalysts

The structures of the carbon in the catalysts, Fe/**L1**@VC−Fe/**L6**@VC, were evaluated by Raman spectroscopy (Figure 3-5). The catalysts have similar carbon morphologies with a similar ratio of I_D/I_G (Table 3-2). The content of iron atoms in the catalysts was determined by ICP-OES. The amounts of iron atoms in Fe/**L1**@VC−Fe/**L4**@VC are relatively smaller than those of the Fe/**L5**@VC and Fe/**L6**@VC, although the contents of iron ions before pyrolysis were fixed to the same value (0.05 mmol). This is because the components of the thermally durable ligands **L1**−**L4** are remained on carbon support after pyrolysis while **L5** and **L6** are almost completely decomposed or sublimed. Surprisingly, over 90% of iron atoms in the precursor were found to be incorporated in Fe/**L1**@VC and Fe/**L2**@VC, while the 30−50% of iron atoms were lost in Fe/**L3**@VC−Fe/**L6**@VC after the pyrolysis. This result suggests that **L1** and **L2** suppress the gasification of the iron complex precursors under the pyrolytic condition (Table 3-2). In addition, Fe/**L1**@VC and Fe/**L2**@VC have larger BET surface areas than the other catalysts (Table 3-2).

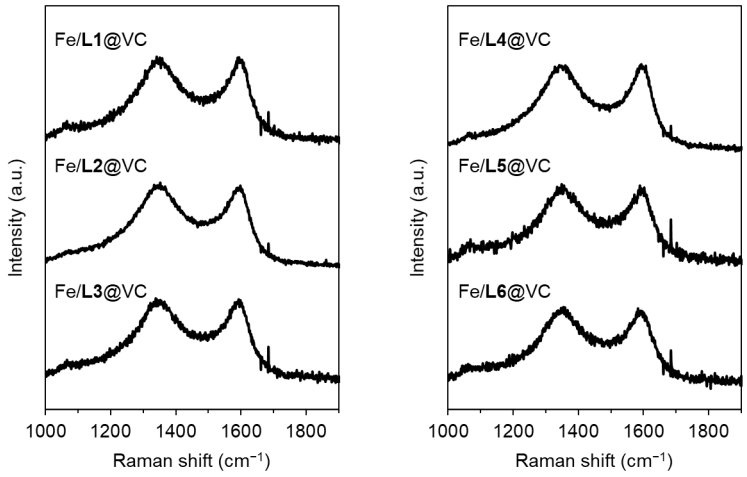

Figure 3-5. Raman spectra of Fe/**L1**@VC, Fe/**L2**@VC, Fe/**L3**@VC, Fe/**L4**@VC, Fe/**L5**@VC, and Fe/**L6**@VC.

Table 3-2. Summary of the Characterizations of the Fe/N/C Catalysts.

Catalysts		Fe/**L1**@VC	Fe/**L2**@VC	Fe/**L3**@VC	**Fe/L4@VC**	Fe/**L5**@VC	Fe/**L6**@VC
Raman spectroscopy							
I_D/I_G		1.07	1.07	1.07	1.14	1.12	1.05
ICP-OES							
Fe content	wt%	1.35	1.66	1.45	1.65	1.88	1.76
Remained Fe[a]	%	93	90	52	67	59	62
BET specific surface area	$m^2 \cdot g^{-1}$	328	304	121	155	128	108

[a]The percentage of iron content in the Fe/N/C catalyst relative to the amount of iron in the precursor (0.05 mmol).

Powder X-ray diffraction

The presence of the iron aggregates in the catalysts was confirmed by powder X-ray diffraction (powder-XRD) measurements (Figure 3-6). All the catalysts exhibit broad diffraction peaks at 2 θ = ca. 26.0 and 44.0º, which are typical signals of the amorphous carbon structure.[28] In addition, the sharp peaks at 35.5º and 42.6º, attributed to the iron oxide, are observed in the XRD spectra of Fe/**L3**@VC−Fe/**L6**@VC.[29] Importantly, only the broad peaks of the carbon structure are confirmed in the XRD spectra of Fe/**L1**@VC and Fe/**L2**@VC, suggesting that the iron complex precursors containing **L1** or **L2** are capable of effectively suppressing the formation of the iron aggregates during pyrolysis.

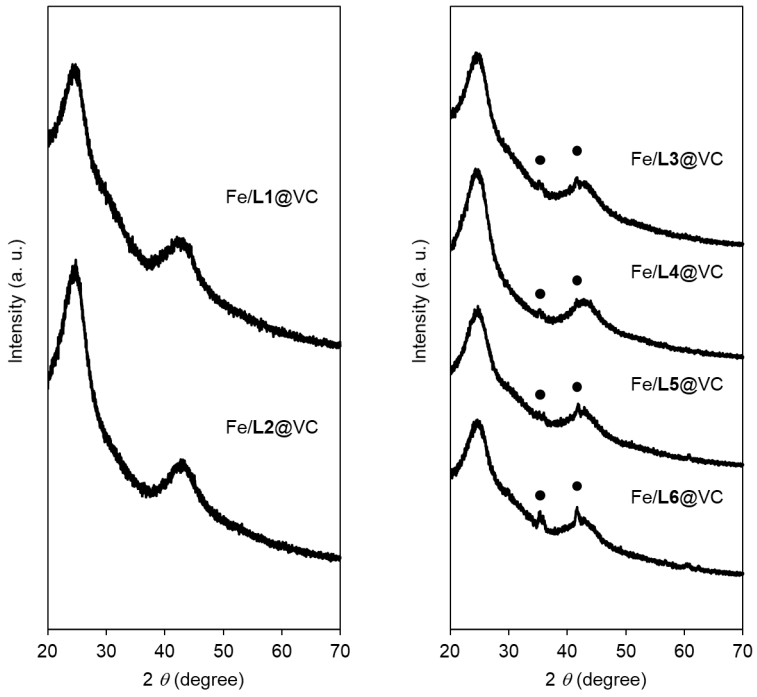

Figure 3-6. XRD patterns of Fe/**L1**@VC, Fe/**L2**@VC, Fe/**L3**@VC, Fe/**L4**@VC, Fe/**L5**@VC, and Fe/**L6**@VC. The XRD peaks of the iron oxide are highlighted with filled circles.

Electron microscopic observations

The absence of the iron aggregates in Fe/**L1**@VC and Fe/**L2**@VC are also confirmed by scanning transmission electron microscopy (STEM) (Figure 3-7). There are no iron aggregates in annular dark field (ADF) and bright field (BF) STEM images, whereas the iron aggregates are observed in the STEM images of Fe/**L3**@VC−Fe/**L6**@VC. These findings are clearly supported by EDX mapping analysis (Figure 3-8). Moreover, the atomical dispersion of iron atoms in Fe/**L1**@VC and Fe/**L2**@VC was confirmed by high-angle annular dark field STEM (HAADF-STEM) observations and electron energy loss spectroscopy (EELS) (Figures 3-9). Taken together, the iron complexes, $[Fe(\mathbf{L1})_3]^{2+}$ and $[Fe(\mathbf{L2})_2]^{2+}$, as the precursors provide atomically dispersed iron atoms in the Fe/N/C catalysts by one-step pyrolysis.

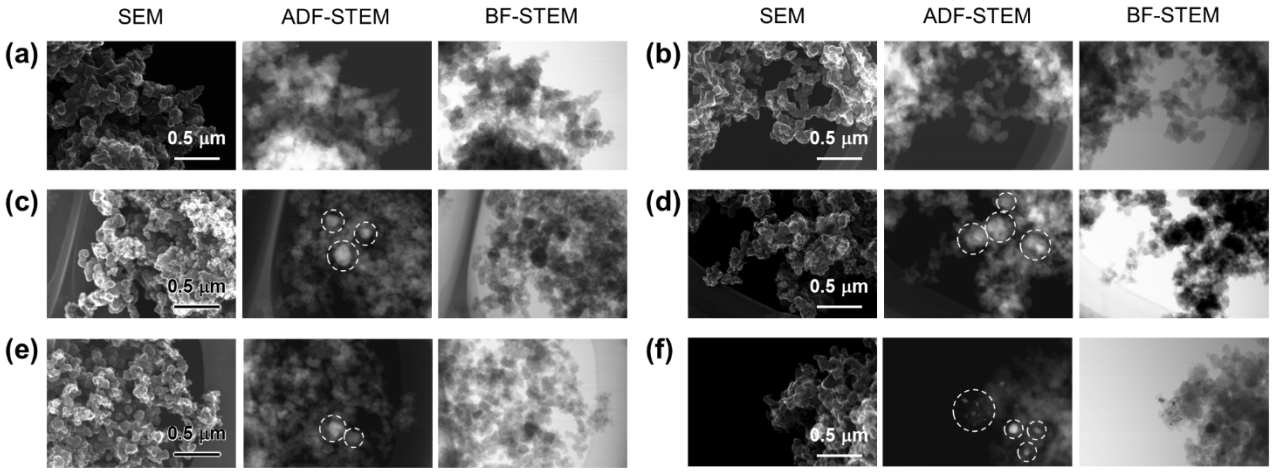

Figure 3-7. SEM, ADF-STEM and BF-STEM images of (a) Fe/**L1**@VC, (b) Fe/**L2**@VC, (c) Fe/**L3**@VC, (d) Fe/**L4**@VC, (e) Fe/**L5**@VC, and (f) Fe/**L6**@VC. The iron aggregates in ADF-STEM images are highlighted with dashed white circle.

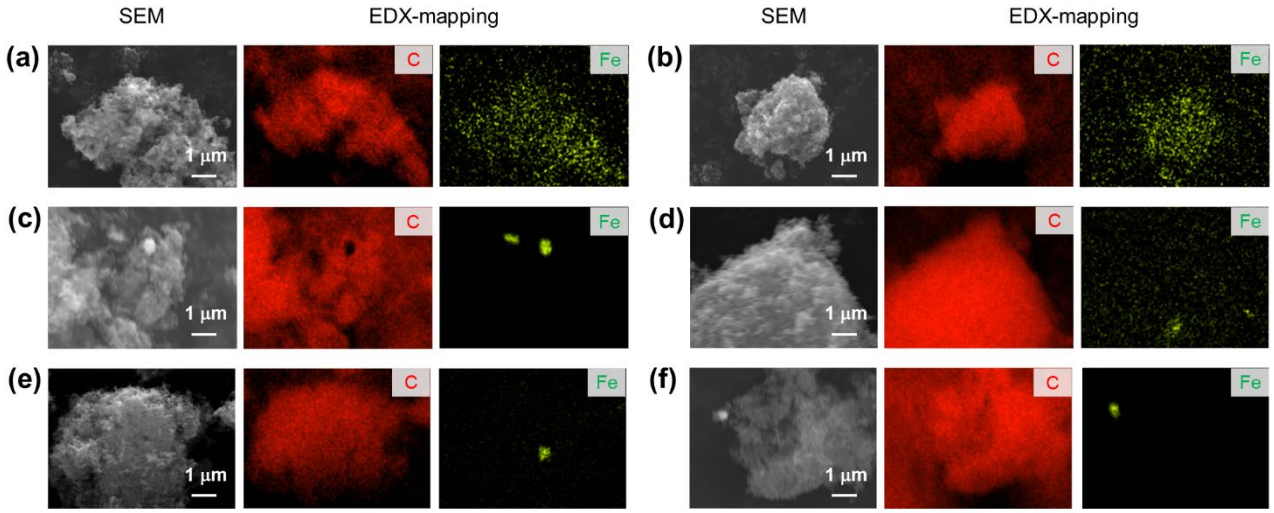

Figure 3-8. SEM and elemental mapping images of carbon (red) and iron (light green) of (a) Fe/**L1**@VC, (b) Fe/**L2**@VC, (c) Fe/**L3**@VC, (d) Fe/**L4**@VC, (e) Fe/**L5**@VC, and (f) Fe/**L6**@VC.

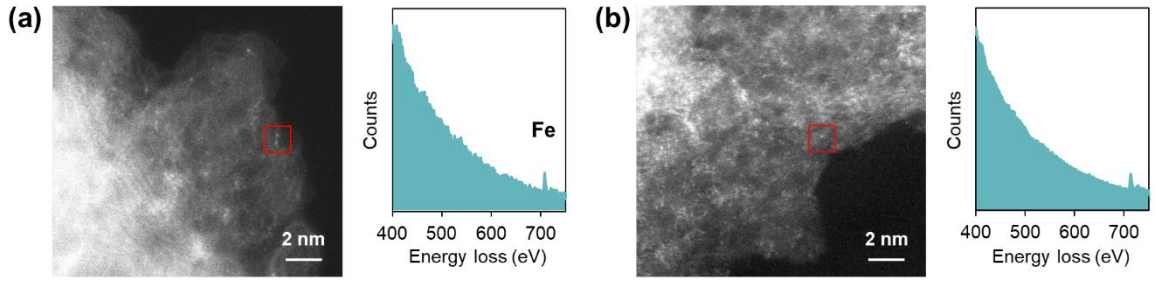

Figure 3-9. HAADF-STEM images of (a) Fe/**L1**@VC and (b) Fe/**L2**@VC and EELS spectra analyzed in the area highlighted with a red square.

X-ray photoelectron spectroscopy

The chemical bonding states of the nitrogen atoms in the Fe/N/C catalysts were evaluated by X-ray photoelectron spectroscopy (XPS). The XPS N1s spectra were fitted with peaks which are assignable to four nitrogen species including pyridinic *N*, Fe−*N*, graphitic *N*, and *N*-oxide (Figure 3-10) and the relative ratios of each nitrogen species are calculated from the peak areas (Table 3-3).[30,31] All the catalysts contain Fe−*N* species, indicating that the Fe−N_x sites are constructed from the iron complex precursors.

In addition, the content of the nitrogen atoms in the Fe−N_x sites (Fe−*N* species) were evaluated from the results of XPS and elemental analysis (Table 3-3). Fe/**L1**@VC (0.40 wt%) and Fe/**L2**@VC (0.63 wt%) have larger amounts of Fe−*N* species relative to Fe/**L3**@VC−Fe/**L6**@VC. This result indicates that the Fe−N_x sites are efficiently constructed from the iron complex precursors, $[Fe(\mathbf{L1})_3]^{2+}$ and $[Fe(\mathbf{L2})_2]^{2+}$, because of the strong coordination with an iron ion and significant thermal durability of **L1** and **L2**. Prticularly, greater quantities of the Fe−*N* species in Fe/**L2**@VC are expected to originate from strong N3-chelating coordination structures in $[Fe(\mathbf{L2})_2]^{2+}$ precursor.

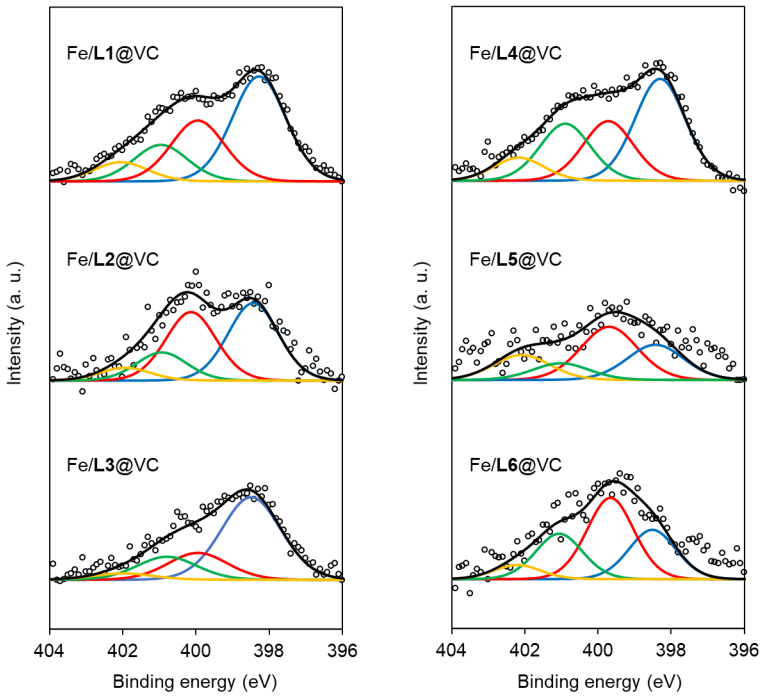

Figure 3-10. XPS N1s spectra of Fe/**L1**@VC, Fe/**L2**@VC, Fe/**L3**@VC, Fe/**L4**@VC, Fe/**L5**@VC, and Fe/**L6**@VC (open circle) with the simulated peaks of Fe−*N* (red), pyridinic *N* (blue), graphitic *N* (green), and *N*-oxide (yellow).

Table 3-3. Summary of XPS and Elemental Analysis.

Catalysts		Fe/**L1**@VC	Fe/**L2**@VC	Fe/**L3**@VC	**Fe/L4@VC**	Fe/**L5**@VC	Fe/**L6**@VC
XPS [N1s]							
Fe−*N*	%	28	37	19	24	41	43
Pyridinic *N*	%	47	42	60	42	27	26
Graphitic *N*	%	16	15	17	25	13	24
N-oxide	%	9	7	4	10	19	7
Elemental analysis							
N	wt%	1.4	1.7	1.1	1.3	0.6	0.4
C	wt%	85.3	85.6	92.2	89.8	92.5	95.7
H	wt%	0.4	0.3	0	0.5	0	0.13
Content of Fe−*N* species[a]	wt%	0.4	0.6	0.2	0.3	0.3	0.2

[a]Calculated from the results of XPS and elemental analysis.

***In-situ* electrochemical Fe K edge X-ray absorption spectroscopy**

To fully characterize the electronic states and the surrounding environment of the atomically dispersed iron atoms in Fe/**L1**@VC and Fe/**L2**@VC, *in-situ* electrochemical Fe K edge X-ray absorption spectroscopy (XAS) mesurements were performed in N_2-purged 0.1 M $HClO_{4aq}$ under the controlled potential. X-ray absorption near edge structure (XANES) profiles of Fe^{3+} species in Fe/N/C-type catalyst are observed when a voltage of 1.0 V vs. RHE is applied to the Fe/**L1**@VC and Fe/**L2**@VC (Figures 3-11).[32,33] When the potential lowers by 0.2 V from 1.0 V to 0 V, the spectrum changes with isosbestic points and the absorption edge shifts to lower energy, indicating a reduction of iron atoms from Fe^{3+} to Fe^{2+}. It was also confirmed that the original XANES spectrum at 1.0 V can be recovered when a potential of 1.0 V is applied again for Fe/**L2**@VC after reducing oxidation state of iron atoms to Fe^{2+}. This indicates that the iron atoms in the catalysts show a reversible Fe^{3+}/Fe^{2+} redox couple. Althought the XANES spectrum of Fe/**L1**@VC at 1.0 V has a pre-edge peak at about 7113 eV, the spectrum converts to match that of Fe/**L2**@VC when a potential of 1.0 V is applied again after reduction and oxidation in Fe/**L1**@VC (Figures 3-12).

The structures of the iron active sites in Fe/**L1**@VC and Fe/**L2**@VC were investigated by Fourier transform of extended X-ray absorption fine structure (FT-EXAFS) with the applied potential of 1.0 V (Figure 3-13). Only one peak was confirmed in the *R* range between 1.0−2.0 Å corresponding to the first coordination sphere of the iron atoms in the catalysts. The curve fitting analysis clarified that the coordination numbers of Fe−N are 4.3 ± 0.3 (Fe/**L1**@VC) and 4.1 ± 0.6 (Fe/**L2**@VC), and Fe−N bond lengths are 1.99 ± 0.02 Å (Fe/**L1**@VC) and 1.97 ± 0.02 Å (Fe/**L2**@VC) (Table 3-4). Therefore, the author concluded that the atomically dispersed iron atoms in Fe/**L1**@VC and Fe/**L2**@VC have the $Fe{-}N_4$ structure (Figure 3-13 inset).

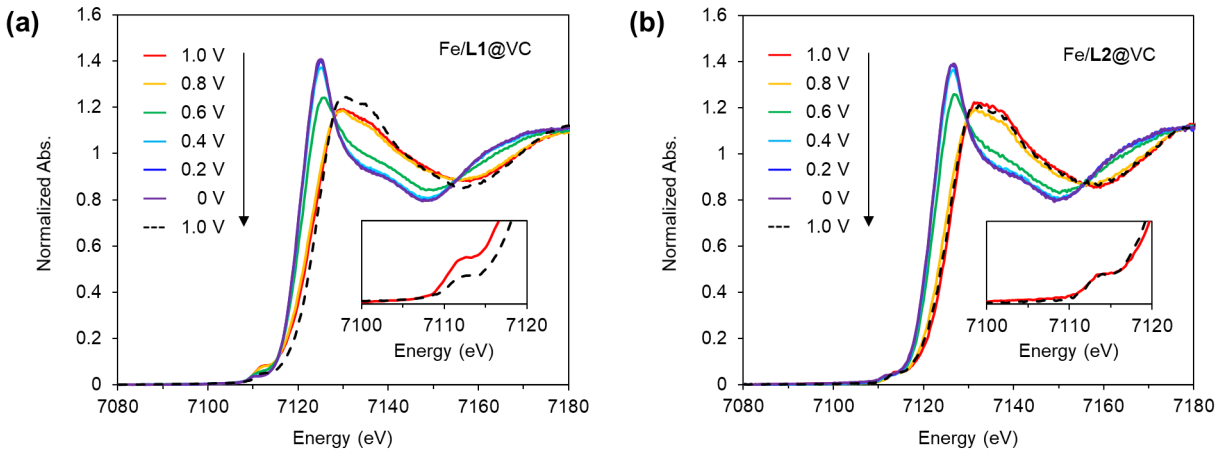

Figure 3-11. Potential-dependent Fe K-edge XANES spectra of (a) Fe/**L1**@VC and (b) Fe/**L2**@VC recorded in 0.1 M $HClO_{4aq}$ solution at 1.0 V (red line), 0.8 V (orange line), 0.6 V (green line), 0.4 V (light blue line), 0.2 V (blue line), and 0 V (purple line) vs. RHE under N_2 atmosphere. The XANES spectra at 1.0 V vs. RHE after sweeping voltage from 1.0 V to 0 V are shown in black dashed lines. The inset figures are the XANES spectra at the pre-edge region.

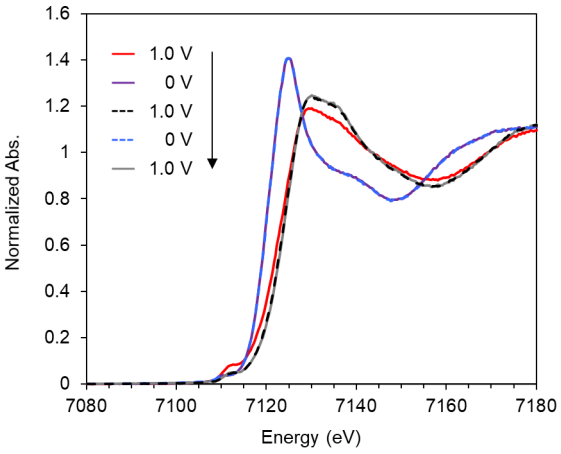

Figure 3-12. Potential-dependent Fe K-edge XANES spectra of (a) Fe/**L1**@VC recorded in 0.1 M $HClO_{4aq}$ solution in order at 1.0 V (red line), 0 V (purple line), 1.0 V (black dashed line), 0 V (blue dashed line), and 1.0 V (gray line) vs. RHE under N_2 atmosphere.

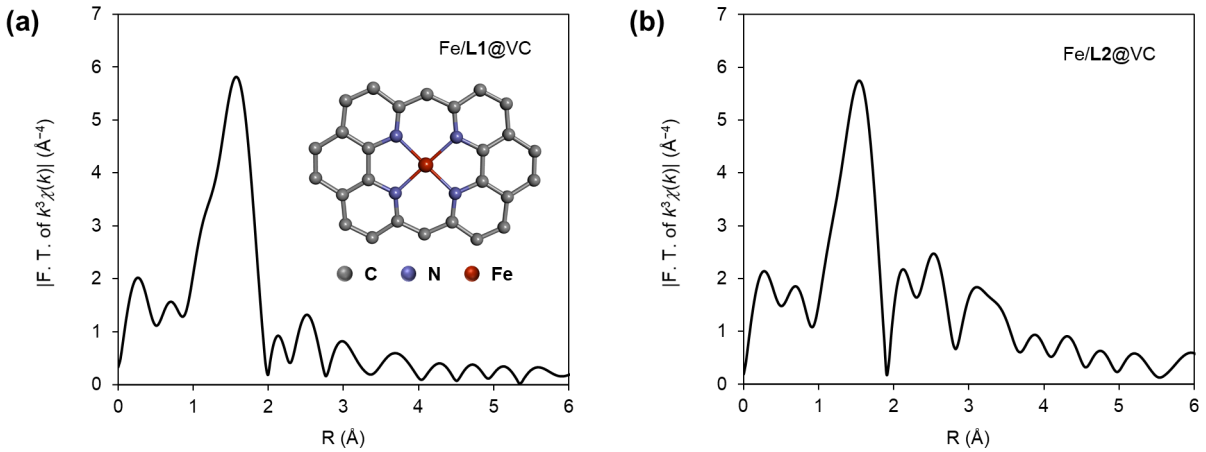

Figure 3-13. FT-EXAFS spectra of (a) Fe/**L1**@VC, and (b) Fe/**L2**@VC at 1.0 V vs. RHE. The inset figure is the model structure of Fe−N_4 sites which are present in Fe/**L1**@VC and Fe/**L2**@VC.

Table 3-4. Summary of the Curve Fitting Analysis for the Fe/N/C Catalysts at 1.0 V vs. RHE.

Fe/N/C catalysts	Fe/**L1**@VC	Fe/**L1**@VC
Coordination atom	Nitrogen	Nitrogen
Coordination number	4.3 ± 0.3	4.1 ± 0.6
R (Å)	1.99 ± 0.02	1.97 ± 0.02
Debye-Waller factor (Å)	0.08 ± 0.01	0.08 ± 002
R-factor (%)	1.6	0.8

Electrocatalytic activities for oxygen reduction reaction (ORR)

The ORR activities of the Fe/N/C catalysts including the Fe–N_4 sites were evaluated by rotating ring-disk electrode (RRDE) measurements (Figure 3-14). Fe/**L1**@VC exhibits high catalytic activity with an onset potential of 0.90 V vs. RHE. The onset potential of Fe/**L2**@VC is more positively shifted (0.93 V vs. RHE). In contrast, Fe/**L3**@VC shows much lower ORR activity (0.69 V vs. RHE), supporting the expectation that the precursor consisting of the stable iron–ligand complex with N2- or N3-chelating coordinations is essential for producing the highly active Fe/N/C catalyst. Fe/**L5**@VC (0.82 V vs. RHE) exhibits lower activity than Fe/**L1**@VC, because the diazatriphenylene framework would be better for the graphitization compared to phenanthroline because of the higher thermal durability. Moreover, Fe/**L4**@VC (0.86 V vs. RHE) and Fe/**L6**@VC (0.79 V vs. RHE) are less active than Fe/**L1**@VC and Fe/**L5**@VC. This means that the bromo substituents on the ligand frameworks promote the graphotization of the ligands and the formation of the active sites. Fe/**L2**@VC further provides lower hydrogen peroxide yields of less than 5% in the range from 0 V to 0.8 V vs. RHE relative to the other catalysts.

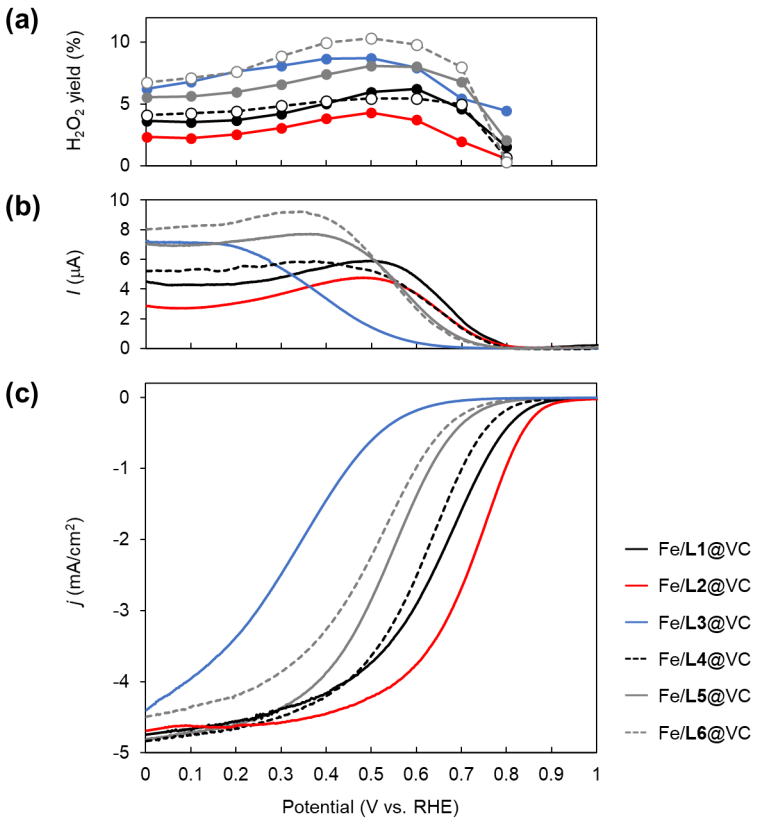

Figure 3-14. (a) H_2O_2 yield, (b) ring current and (c) disk current density of the catalysts. The linear sweep voltammograms were recorded during positive sweep with 5 $mV \cdot s^{-1}$ at 2000 rpm in an O_2-saturated 0.1 M $HClO_{4aq}$ solution.

In addition, the turnover frequency (TOF), which represents the number of electrons transferred per an active site and per a second, was evaluated based on the value of the mass-based site density (MSD), defined as the number of redox-active iron atoms, basically Fe–N_4 sites, per unit mass of the catalyst. The MSD values were calculated from the results of the cyclic voltammetry (CV) measurements in a N_2-purged electrolyte (Figure 3-15).[34,35] Fe/**L2**@VC exhibits the highest turnover frequency (TOF) at 0.8 V vs RHE with 0.21 e·site^{-1}·s^{-1}. This performance is better than that of Fe/**L1**@VC with 0.17 e·site^{-1}·s^{-1} (Table 3-5). Notably, these ORR activities clearly correlate with the amounts of Fe–*N* species (Table 3-3) and the value of MSD of the redox active iron atoms (Table 3-5). Taken together, the Fe–N_4 sites constructed in Fe/**L1**@VC and Fe/**L2**@VC contribute greatly to the enhancement of the ORR activities.

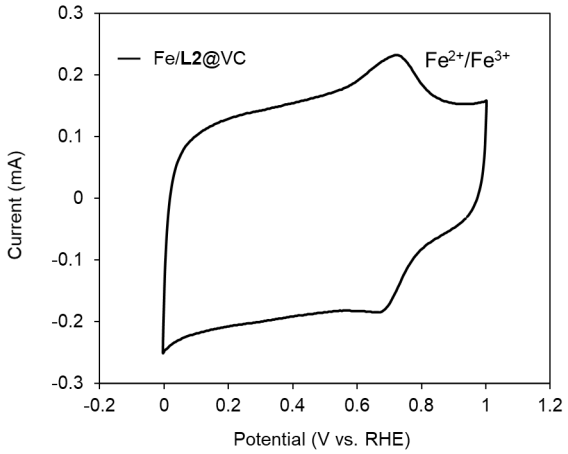

Figure 3-15. CV curve of Fe/**L2**@VC in an N_2-saturated 0.1 M $HClO_{4aq}$ solution at 50 mV·s^{-1} at 2000 rpm from 0 to 1.0 V vs. RHE. Catalyst loading: 0.41 mg_{cat}·cm^{-2}.

Table 3-5. Summary of the Electrochemical Measurements.

Catalysts		Fe/**L1**@VC	Fe/**L2**@VC	Fe/**L3**@VC	Fe/**L4**@VC	Fe/**L5**@VC	Fe/**L6**@VC
E_{onset}	V vs. RHE	0.90	0.93	0.69	0.86	0.82	0.79
H_2O_2[a]	%	< 7	< 5	< 8	< 6	< 8	< 10
MSD[b]	10^{19}·sites·g_{cat}^{-1}	1.8	3.6	0.2	2.7	1.5	1.9
$TOF_{at\ 0.8\ V}$[c]	10^{-2}·e·site^{-1}·s^{-1}	17	21	3	4	2	2

[a]The percentage of H_2O_2 during O_2 reduction. [b]Mass-based site density. [c]Turnover frequency at 0.8 V vs. RHE.

3-3. Summary

The Fe/N/C single-atom catalysts were prepared by one-step pyrolysis of the iron complexes containing thermally durable 5,6,7,8-tetraphenyl-1,12-diazatriphenylene ligands **L1** or **L2**, which have N2- or N3-chelating coordination, respectively, and preorganized aromatic rings with bromo substituents. The design of the ligand for the iron complex precursor is a key to provide the construction of atomically dispersed Fe−N_4 sites without generating the iron aggregates during pyrolysis. In particular, $[Fe(\mathbf{L2})_2]^{2+}$ is more efficiently converted to the Fe−N_4 site than $[Fe(\mathbf{L1})_3]^{2+}$. This indicates the significance of N3-cooridination provided by the 5,6,7,8-tetraphenyl-1,12-diazatriphenylene ligand with an additional pyridine moiety for constructing the Fe−N_4 sites. Consequently, Fe/**L2**@VC contains a high quantity of the Fe−N_4 sites and has the high electrocatalytic activity in ORR with positively shifted onset potentials of 0.93 V vs. RHE and a TOF value of 0.21 $e \cdot site^{-1} \cdot s^{-1}$. The work described in the chapter 3 provides an attractive strategy for preparation of Fe/N/C single-atom catalysts with atomically-defined active sites in a graphene layer by one-step pyrolysis, paving the way for the construction of on-demand metal active sites on the surface of carbon materials and other heterogeneous catalysts.

3-4. Experimental Section

Materials and methods

All reagents were used without purification. All solvents were dried with molecular sieves 3Å before use. ^1H NMR and ^{13}C NMR spectra were recorded on a Bruker BioSpin DPX400 NMR spectrometer (400 MHz). Chemical shifts were reported in ppm relative to the residual solvent resonances. ESI-TOF MS analyses were performed on a Bruker micrOTOF focus III mass spectrometer. The values of thernally decomposition temperature (T_d) of the ligands were evaluated by thermogravimetry-differential thermal analysis (TG-DTA) using a Mac Science TG-DTA TMA DSC with a heating rate of 10 ºC$\cdot min^{-1}$ in an N_2 stream on platinum pan. The morphologies of the catalysts and their elemental mapping images were investigated by scanning electron microscopy (SEM) using JEOL JSM-7600F equipped with an energy-dispersive X-ray spectroscope (EDX). SEM images, annular dark field scanning transmission electron microscopic (ADF-STEM) images, and bright field scanning transmission electron microscopic (BF-STEM) images in the same field of view of the catalysts were collected by scanning transmission electron microscope (STEM) using HITACHI HD-2000. The atomically dispersed iron atoms in the catalysts were observed by high-angle annular dark field aberration-corrected scanning transmission electron microscopy (HAADF-STEM) using JEOL JEM-ARM200F equipped with an electron energy loss spectroscopy (EELS). The iron content of each Fe/N/C catalysts was determined by inductively coupled plasma atomic emission spectroscopy (ICP-AES) using a SHIMAZDU ICPS-7510 system. The elemental analysis of carbon, hydrogen and nitrogen was conducted on JM10 (J-SCIENCE LAB Co., Ltd.). Raman spectra were obtained using a JASCO NRS3100 instrument with a 532 nm laser. The chemical bonding states of nitrogen atoms in the catalysts were determined by X-ray photoelectron

spectroscopy (XPS) using a SHIMADZU KRATOSAXIS-165x. X-ray diffraction (XRD) spectra were measured with Bruker D2 PHASER 2nd Generation with CuKα radiation. Specific surface areas were evaluated using a MicrotracBEL BELSORP-mini II analyzer and calculated by Brunauer–Emmett–Teller (BET) method. XAS experiments were carried out at the beamline BL12C in Photon Factory (Proposal No. 2021G083).

Synthesis of the precursors

Scheme 3-1. Synthesis of compound **L1**.

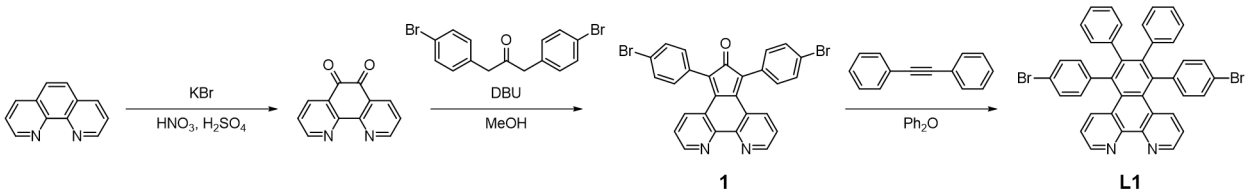

Scheme 3-2. Synthesis of compound **L2**.

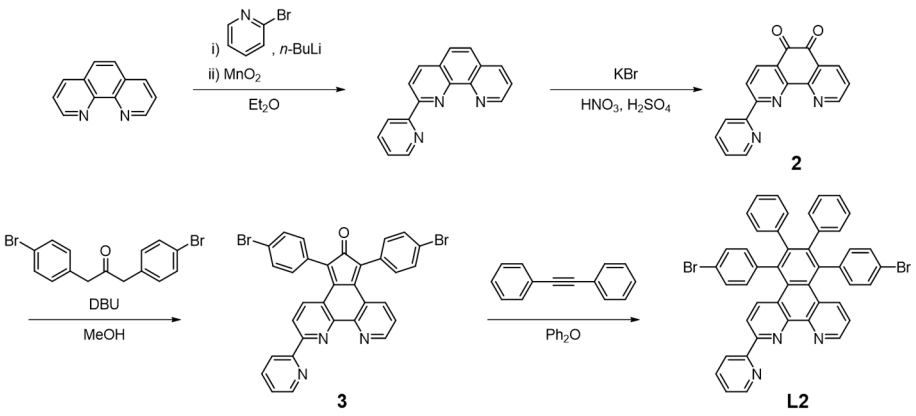

Scheme 3-3. Synthesis of compound **L3**.

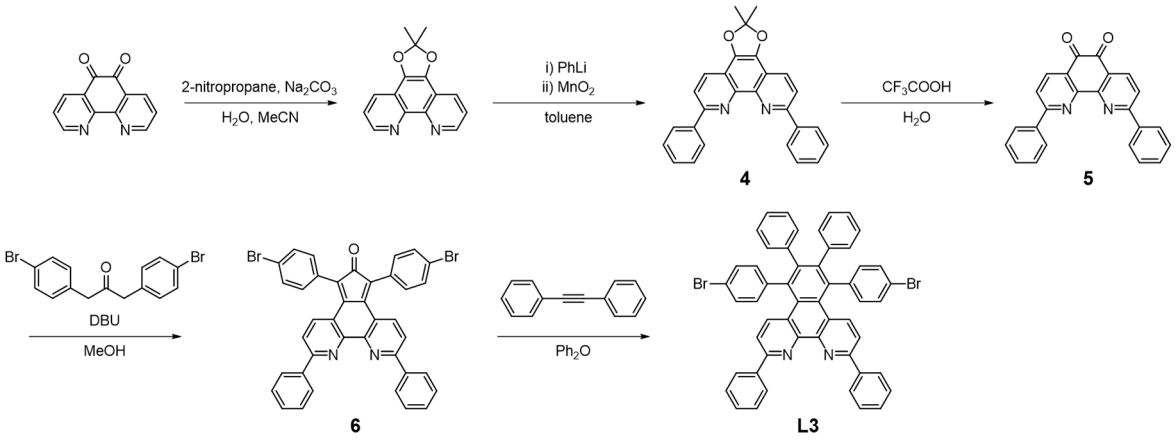

Scheme 3-4. Synthesis of compound **L4**.

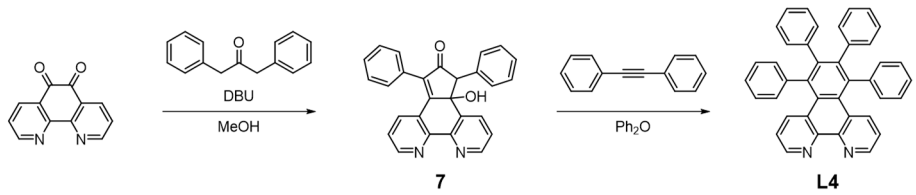

General procedure for synthesis of 1,10-phenathroline-5,6-dione and compound 2.[36]

A mixture of 1,10-phenanthoroline, or 2-(pyridin-2-yl)-1,10-phenanthroline (10 mmol), and KBr (1.79 g, 15 mmol) were slowly added to an ice-cooled mixture of H_2SO_4 (20 mL) and HNO_3 (10 mL). The mixture was refluxed with stirring for 4 h, and then poured onto 100 mL ice-cooled water. The yellow aqueous solution was carefully neutralized with NaOH, then the product was extracted with CH_2Cl_2. The solution was dried over Na_2SO_4, and concentrated to afford the product.

General procedure for synthesis of compounds 1, 3, 6, and 7.

To a suspension of 1,10-phenanthroline-5,6-dione derivative (1.25 mmol) and 1,3-diphenylpropane-2-one derivative (1.0 mmol) in dry MeOH (50 mL) was slowly added 1,8-diazabicyclo[5.4.0]undec-7-ene (DBU) (179 μL, 1.2 mmol). The mixture was stirred at room temperature for 24 h. The precipitates were collected and washed with cold MeOH to afford the products.

General procedure for synthesis of compounds L1, L2, L3, and L4.[37,38]

Compound **1**, **3**, **6**, or **7** (0.25 mmol) and 1,2-diphenylacetylene (89.1 mg, 0.5 mmol) were suspended in diphenyl ether (5 mL) and the mixture was deoxygenated by freeze-pump-thaw cycling. The mixture was stirred at 160 ºC under an Ar atmosphere for 24 h. After the mixture was cooled to room temperature, the residues were purified by silica gel column chromatography to afford the product.

Synthesis of 5,7-bis(4-bromophenyl)-6*H*-cyclopenta[f][1,10]phenanthrolin-6-one (1).

1,10-phenanthroline-5,6-dione (263 mg, 1.25 mmol) and 1,3-bis(4-bromophenyl)propan-2-one (368 mg, 1.0 mmol) were used for the reaction, and compound **1** was obtained as a green solid. Yield 58%. ^{1}H NMR (400 MHz, CD_2Cl_2): δ = 8.86 (dd, 2H, J = 0.8, 4.0 Hz), 7.81 (dd, 2H, J = 0.8, 8.4 Hz), 7.27 (d, 4H, J = 8.4 Hz), 7.10 (dd, 2H, J = 4.4, 8.4 Hz), 7.08 (dd, 2H, J = 4.8, 8.4 Hz); ^{13}C NMR (100 MHz, CD_2Cl_2): δ = 198.91, 152.90, 152.07, 150.75, 146.66, 135.44, 132.55, 131.78, 130.60, 126.23, 124.50, 123.42; ESI-TOF MS (positive mode) m/z calcd. for $C_{27}H_{14}Br_2N_2O$ $[M + H]^+$ 540.9546, found 540.9538.

Synthesis of 5,8-bis(4-bromophenyl)-6,7-diphenyl-1,12-diazatriphenylene (L1).

Compound **1** (135 mg, 0.25 mmol) and 1,2-diphenylacetylene (89.1 mg, 0.5 mmol) were used for the reaction, and the product was purified by silica gel column chromatography ($CHCl_3$/MeOH/TEA = 100 : 1 : 1) to afford compound **L1** as a colorless solid. Yield 38%. ^{1}H NMR (400 MHz, CD_2Cl_2): δ = 8.68 (dd, 2H, J = 1.2, 4.4 Hz), 7.83

(dd, 2H, J = 1.2, 4.8 Hz), 7.66 (d, 4H, J = 8.4 Hz), 7.31 (d, 4H, J = 8.4 Hz), 7.08 (dd, 2H, J = 4.4, 4.8 Hz), 6.95 (m, 10H), 6.73 (d, 4H, J = 8.4 Hz); ^{13}C NMR (100 MHz, CD_2Cl_2): δ = 149.38, 147.78, 141.89, 141.34, 139.84, 137.43, 136.81, 133.84, 131.93, 131.62, 129.92, 127.76, 127.30, 126.18, 121.70, 121.40; ESI-TOF MS (positive mode) *m*/*z* calcd. for $C_{40}H_{24}Br_2N_2$ $[M + H]^+$ 691.0379, found 691.0384.

Synthesis of 2-(pyridin-2-yl)-1,10-phenanthroline.

According to the procedure described in the literature,[39] 2-(pyridin-2-yl)-1,10-phenanthroline was prepared.

Synthesis of 2-(pyridin-2-yl)-1,10-phenanthroline-5,6-dione (2).

2-(pyridin-2-yl)-1,10-phenanthroline (2.57 g, 10 mmol) was used for the reaction, and compound **2** was obtained as a yellow solid. Yield 71%. ^{1}H NMR (400 MHz, $CDCl_3$): δ = 9.35 (d, 1H, J = 4.0 Hz), 9.07 (d, 1H, J = 8.4 Hz), 9.00 (d, 1H, J = 8.4 Hz), 8.96 (d, 1H, J = 8.4 Hz), 8.78 (d, 1H, J = 4.0 Hz), 8.54 (d, 1H, J = 8.4 Hz), 7.94 (t, 1H, J = 8.0 Hz), 7.84 (dd, 1H, J = 4.0, 4.4 Hz), 7.44 (dd, 1H, J = 4.8, 8.0 Hz); ^{13}C NMR (100 MHz, $CDCl_3$): δ = 159.74, 155.37, 151.68, 149.52, 147.51, 146.50, 144.35, 138.95, 137.41, 132.79, 125.79, 125.69, 125.14, 124.42, 123.34, 122.35, 121.58; ESI-TOF MS (positive mode) *m*/*z* calcd. for $C_{17}H_9N_3O_2$ $[M + H]^+$ 288.0768, found 288.0775.

Synthesis of 5,7-bis(4-bromophenyl)-2-(pyridin-2-yl)-6*H*-cyclopenta[f][1,10]phenanthrolin-6-one (3).

Compound **2** (359 mg, 1.25 mmol) and 1,3-bis(4-bromophenyl)propan-2-one (368 mg, 1.0 mmol) were used for the reaction, and compound **3** was obtained as a colorless solid. Yield 45%. ^{1}H NMR (400 MHz, DMSO-d_6): δ = 8.81 (d, 1H, J = 4.0 Hz),8.75 (d, 1H, J = 4.0 Hz), 8.66 (d, 1H, J = 8.0 Hz), 8.20 (d, 1H, J = 8.0 Hz), 8.03 (t, 1H, J = 7.6 Hz), 7.96 (d, 1H, J = 7.6 Hz), 7.68 (m, 3H), 7.62 (d, 2H, J = 8.0 Hz), 7.53 (m, 4H), 7.34 (d, 2H, J = 8.0 Hz), 6.44 (s, 1H), 4.77 (s, 1H); ^{13}C NMR (100 MHz, DMSO-d_6): δ = 203.28, 160.63, 157.35, 154.73, 150.16, 149.97, 149.62, 149.37, 137.70, 137.34, 137.09, 136.13, 135.21, 134.52, 132.17, 132.00, 131.69, 131.39, 130.99, 129.87, 125.30, 125.07, 122.46, 121.60, 120.83, 120.39, 74.46, 59.92; ESI-TOF MS (positive mode) *m*/*z* calcd. for $C_{32}H_{17}Br_2N_3O$ $[M + H_3O]^+$ 635.9917, found 635.9920.

Synthesis of 5,8-bis(4-bromophenyl)-6,7-diphenyl-2-(2-pyridyl)-1,12-diazatriphenylene (L2).

Compound **3** (193 mg, 0.25 mmol) and 1,2-diphenylacetylene (89.1 mg, 0.5 mmol) were used for the reaction, and the prduct was purified by silica gel column chromatography ($CHCl_3$/MeOH/TEA = 100 : 1 : 1) and followed by reprecipitation in a solution of hexane/CH_2Cl_2 to afford compound **L2** as a colorless solid. Yield 25%. ^{1}H NMR (400 MHz, CD_2Cl_2): δ = 8.92 (dd, 2H, J = 1.2, 4.4 Hz), 8.79 (d, 1H, J = 8.0 Hz), 8.68 (d, 1H, J = 4.0 Hz), 8.20 (d, 1H, J = 4.4 Hz), 7.92 (m, 2H), 7.84 (dd, 1H, J = 1.2, 8.0 Hz), 7.37 (dd, 1H, J = 1.2, 6.0 Hz), 7.29 (dd, 4H, J = 3.6, 8.4 Hz), 7.14 (dd, 1H, J = 4.4, 4.8 Hz), 6.98 (m, 10H), 6.74 (m, 4H); ^{13}C NMR (100 MHz, CD_2Cl_2): δ = 155.92, 154.70, 149.23, 148.91, 147.36, 146.80, 141.59, 141.57, 140.94, 140.87, 139.45, 137.46, 137.16, 137.04, 136.95, 136.60, 133.45, 131.58, 131.54, 131.23, 129.64, 127.73, 127.56, 126.91, 125.79, 124.05, 121.69, 121.32, 121.11, 121.01, 118.68; ESI-TOF MS (positive mode) *m*/*z* calcd. for $C_{45}H_{27}Br_2N_3$ $[M + H]^+$ 786.0512, found 786.0513.

Synthesis of 2,2-dimethyl-6,9-diphenyl-[1,3]dioxolo[4,5-f][1,10]phenanthroline (4).

Compound **4** was synthesized according to the literature with some modifications.[40] A solution of 2,2-dimethyl-[1,3]dioxolo[4,5-f][1,10]phenanthroline (4.0 g, 15.9 mmol) in dry and degassed toluene (150 mL) was cooled to 0 ºC under an Ar atmosphere and stirred vigorously. The mixture was slowly added a solution of 1.2 equivalent of phenyllithium (1.9 mol·L^{-1}) in *n*-butyl ether (10 mL, 19 mmol) and the mixture was stirred for 2 h. The reaction was quenched by adding H_2O (30 mL) and the product was extracted with CH_2Cl_2. To the solution was added MnO_2 (15 g) and the mixture was stirred for 2 h. After the precipitates were filtered through celite, the solution was concentrated *in vacuo* to afford a mono-substituted compound. The same procedure was performed again to obtain compound **4** as a red oil. Yield 92%. ^{1}H NMR (400 MHz, $CDCl_3$): δ = 8.45 (d, 4H, J = 7.6 Hz), 8.32 (d, 2H, J = 8.4 Hz), 8.15 (d, 2H, J = 8.4 Hz), 7.59 (t, 4H, J = 7.6 Hz), 7.48 (t, 2H, J = 7.6 Hz), 1.91 (s, 6H); ^{13}C NMR (100 MHz, $CDCl_3$): δ = 154.57, 142.49, 139.74, 136.66, 129.31, 128.96, 127.59, 120.82, 119.88, 117.47, 26.29; ESI-TOF MS (positive mode) *m*/*z* calcd. for $C_{27}H_{22}N_2O_2$ $[M + H]^+$ 407.1754, found 407.1749.

Synthesis of 2,9-diphenyl-1,10-phenanthroline-5,6-dione (5).

Compound **5** was synthesized according to the literature with some modifications.[41] Compound **4** (2.0 g, 5.0 mmol) was dissolved in a mixture of water (25 mL) and trifluoroacetic acid (50 mL), and the mixture was stirred at 50 ºC for 5 h under aerobic conditions. After the mixture was cooled to room temperature, the solvents were evaporated *in vacuo*. The residue was extracted with CH_2Cl_2 and washed with an aqueous solution of $NaHCO_3$ (1.0 mol·L^{-1}) and water. The organic layer was dried over $NaSO_4$, and the solvent was evaporated *in vacuo* to afford compound **5**. Yield 85%. ^{1}H NMR (400 MHz, $CDCl_3$): δ = 8.54 (d, 2H, J = 8.4 Hz), 8.36 (dd, 4H, J = 1.2, 8.4 Hz), 8.02 (d, 2H, J = 8.4 Hz), 7.58 (m, 6H); ^{13}C NMR (100 MHz, $CDCl_3$): δ = 179.97, 163.10, 153.13, 138.19, 137.79, 131.25, 129.28, 128.06, 126.85, 121.58; ESI-TOF MS (positive mode) *m*/*z* calcd. for $C_{24}H_{14}N_2O_2$ $[M + H]^+$ 363.1128, found 363.1128.

Synthesis of 5,7-bis(4-bromophenyl)-2,10-diphenyl-6*H*-cyclopenta[f][1,10]phenanthrolin-6-one (6).

Compound **5** (453 mg, 1.25 mmol) and 1,3-bis(4-bromophenyl)propan-2-one (368 mg, 1.0 mmol) were used for the reaction, and the crude products containing compound **6** were obtained as a brown solid. The crude products were used for synthesis of compound **L3** without further purification. ESI-TOF MS (positive mode) *m*/*z* calcd. for $C_{39}H_{22}Br_2N_2O$ $[M + H_3O]^+$ 711.0277, found 711.0280.

Synthesis of 5,8-bis(4-bromophenyl)-2,6,7,11-tetraphenyl-1,12-diazatriphenylene (L3).

Compound **6** (174 mg, 0.25 mmol) and 1,2-diphenylacetylene (89.1 mg, 0.5 mmol) were used for the reaction, and the prduct was purified by silica gel column chromatography ($CHCl_3$/MeOH/TEA = 100 : 1 : 1). The product was precipitated from hexane/CH_2Cl_2 to afford compound **L3** as a colorless solid. Yield 28%. ^{1}H NMR (400 MHz, $CDCl_3$): δ = 8.41 (d, 4H, J = 8.0 Hz), 7.83 (d, 2H, J = 8.8 Hz), 7.63 (d, 2H, J = 8.8 Hz), 7.56 (t, 4H, J = 7.2 Hz), 7.48 (d, 2H, J = 7.2 Hz), 7.28 (d, 4H, J = 8.0 Hz), 6.95 (m, 10H), 6.70 (d, 2H, J = 7.2 Hz); ^{13}C NMR (100 MHz, $CDCl_3$):

δ = 155.72, 147.29, 141.36, 140.97, 139.43, 138.92, 137.62, 137.06, 133.51, 131.82, 131.34, 129.74, 129.60, 128.92, 127.45, 127.20, 126.53, 126.02, 121.33, 118.13; ESI-TOF MS (positive mode) *m*/*z* calcd. for $C_{52}H_{32}Br_2N_2$ $[M + H]^+$ 843.1005, found 843.1013.

Synthesis of 4b-hydroxy-5,7-diphenyl-4b,5-dihydro-6*H*-cyclopenta[f][1,10]phenanthrolin-6-one (7).

1,10-phenanthroline-5,6-dione (263 mg, 1.25 mmol) and 1,3-diphenylpropane-2-one (210 mg, 1.0 mmol) were used for the reaction, and compound **7** was obtained as a colorless solid. Yield 45%. ^{1}H NMR (400 MHz, $CDCl_3$): δ = 8.83 (d, 1H, *J* = 4.4 Hz), 8.79 (d, 1H, *J* = 4.4 Hz), 8.04 (d, 1H, *J* = 7.6 Hz), 8.04 (d, 1H, *J* = 7.6 Hz), 7.49 (m, 4H), 7.42 (m, 3H), 7.16 (dd, 1H, *J* = 4.4, 7.6 Hz), 4.51 (s, 1H), 2.45 (s, 1H); ^{13}C NMR (100 MHz, $CDCl_3$): δ = 202.84, 158.86, 152.69, 151.03, 150.39, 150.30, 140.39, 136.66, 136.57, 135.00, 134.07, 132.03, 129.99, 129.25, 129.19, 129.08, 129.05, 128.40, 125.35, 124.77, 123.75, 74.93, 61.08; ESI-TOF MS (positive mode) *m*/*z* calcd. for $C_{27}H_{18}N_2O_2$ $[M + H]^+$ 403.1441, found 403.1440.

Synthesis of 5,6,7,8-tetraphenyl-1,12-diazatriphenylene (L4).

Compound **7** (101 mg, 0.25 mmol) and 1,2-diphenylacetylene (89.1 mg, 0.5 mmol) were used for the reaction, and the prduct was purified by silica gel column chromatography ($CHCl_3$/MeOH/TEA = 100 : 1 : 1). The product was precipitated from hexane/CH_2Cl_2 to afford compound **L4** as a colorless solid. Yield 47%. ^{1}H NMR (400 MHz, $CDCl_3$): δ = 8.90 (d, 2H, *J* = 4.4 Hz), 7.80 (d, 2H, *J* = 8.8 Hz), 7.13 (m, 6H), 7.04 (m, 4H), 7.01 (d, 2H, *J* = 4.4 Hz), 6.89 (m, 6H), 6.70 (m, 4H); ^{13}C NMR (100 MHz, $CDCl_3$): δ = 149.22, 147.46, 142.01, 141.58, 139.88, 138.30, 136.90, 131.89, 131.43, 129.63, 128.56, 127.93, 126.94, 126.89, 125.67, 121.39; ESI-TOF MS (positive mode) *m*/*z* calcd. for $C_{40}H_{26}N_2$ $[M + H]^+$ 535.2169, found 535.2174.

Synthesis of Fe complex ($[Fe(L1)_3](ClO_4)_2$).

A solution of compound **L1** (208 mg, 0.3 mmol) in $CHCl_3$ (50 mL) and a solution of $Fe(ClO_4)_2 \cdot 6H_2O$ (36.3 mg, 0.1 mmol) in MeOH (10 mL) were combined and the mixture was stirred for 2 h at room temperature under an N_2 atmosphere. Then, the obtained precipitates were filtered and washed with a small amount of MeOH and Et_2O to afford the iron complex $[Fe(\mathbf{L1})_3](ClO_4)_2$ as a red solid. The complexation was confirmed by UV-Vis titration experiment (Figure 3-16) and single crystals for X-ray crystal structure analysis were grown from MeCN/Et_2O by gas-liquid diffusion method (Figure 3-4a).

Synthesis of Fe complex ($[Fe(L2)_2](ClO_4)_2$).

A solution of compound **L2** (154 mg, 0.2 mmol) in $CHCl_3$ (50 mL) and a solution of $Fe(ClO_4)_2 \cdot 6H_2O$ (36.3 mg, 0.1 mmol) in MeOH (10 mL) were combined and the mixture was stirred for 2 h at room temperature under an N_2 atmosphere. Then, the obtained precipitates were filtered and washed with a small amount of MeOH and Et_2O to afford the iron complex $[Fe(\mathbf{L2})_2](ClO_4)_2$ as a purple solid. The complexation was confirmed by UV-Vis titration experiment (Figure 3-17) and single crystals for X-ray crystal structure analysis were grown from MeCN/Et_2O by gas-liquid diffusion method (Figure 3-4b).

Synthesis of Fe complex ([Fe(L4)$_3$](ClO$_4$)$_2$).

A solution of compound **L4** (160 mg, 0.3 mmol) in $CHCl_3$ (50 mL) and a solution of $Fe(ClO_4)_2 \cdot 6H_2O$ (36.3 mg, 0.1 mmol) in MeOH (10 mL) were combined and the mixture was stirred for 2 h at room temperature under an N_2 atmosphere. Then, the obtained precipitates were filtered and washed with small amount of MeOH and Et_2O to afford the iron complex [Fe(**L4**)$_3$](ClO$_4$)$_2$ as a red solid. Single crystals for X-ray crystal structure analysis were grown from MeCN/Et_2O by gas-liquid diffusion method (Figure 3-4c).

Preparation of the mixture of Fe ion and compound L3.

A solution of compound **L3** (253 mg, 0.3 mmol) in $CHCl_3$ (50 mL) and a solution of $Fe(ClO_4)_2 \cdot 6H_2O$ (36.3 mg, 0.1 mmol) in MeOH (10 mL) were combined and the mixture was stirred for 2 h at room temperature. Then, the solvents were evaporated in vacuo to afford the mixture of Fe ion and compound **L3**. The UV-Vis spectrum almost unchanged before and after addition of iron ions, indicating that the stable coordination structure is not formed between an iron ion and **L3** (Figure 3-18).

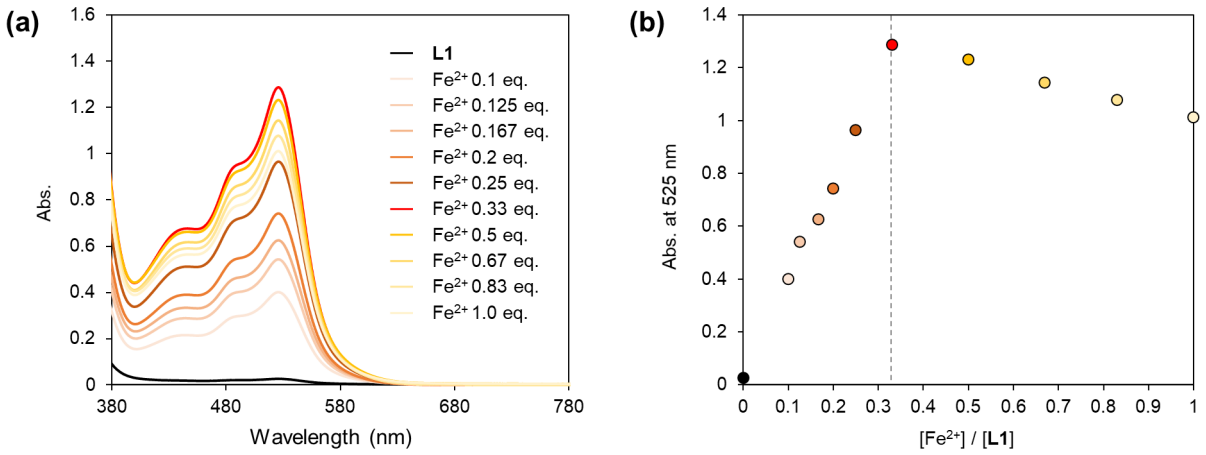

Figure 3-16. (a) UV-Vis spectra of **L1** vs. Fe^{2+} in $CHCl_3$. (b) Plots of absorbance at 525 nm against the ratio of [Fe^{2+}]/[**L1**].

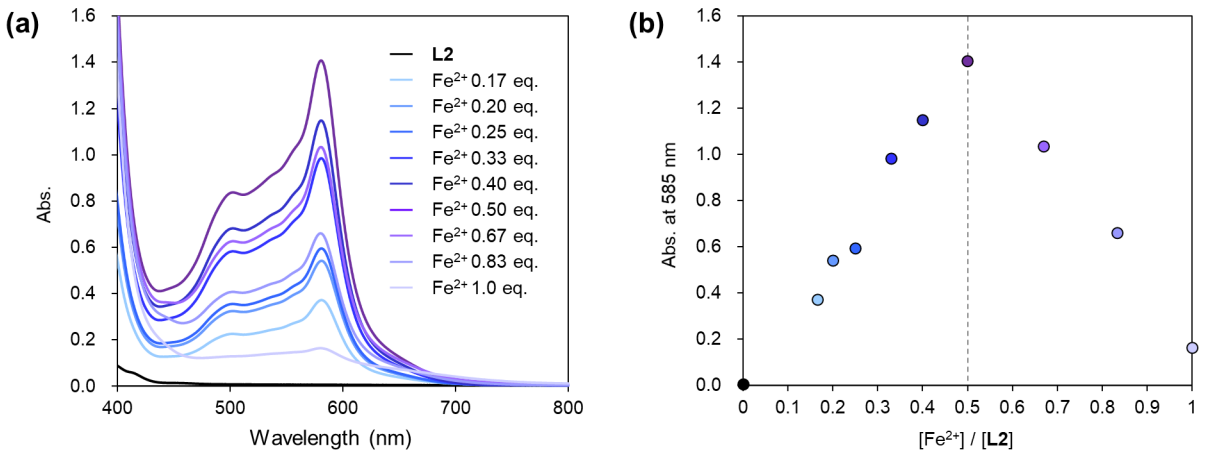

Figure3-17. (a) UV-Vis spectra of **L2** vs. Fe^{2+} in $CHCl_3$. (b) Plots of absorbance at 585 nm against the ratio of [Fe^{2+}]/[**L2**].

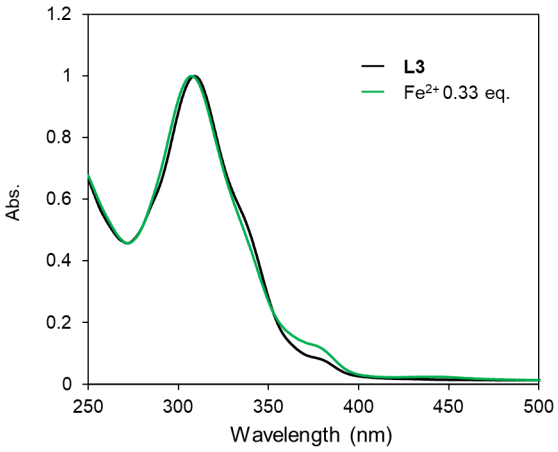

Figure3-18. UV-Vis spectra of **L3** (black) and **L3** with Fe^{2+} (0.33 eq.) (green) in $CHCl_3$.

X-ray crystallography

Diffraction data of the iron complexes were collected on a two-dimensional X-ray detector (PILATUS 200K/R) equipped in Rigaku XtaLAB P200 diffractometer using multi-layer mirror monochromated CuKα radiation (λ = 1.54187 Å) at 223 or 93 K. Diffraction Data collection, cell refinement, and data reduction were carried out with CrysAlis PRO.[42] SHELXT[43] was used for the structure solution of the crystals. These calculations were performed with the observed reflections [$I > 2\sigma(I)$] with the program CrystalStructure crystallographic software.[44–46] Structural refinement was performed by SHELXL. All non-hydrogen atoms were refined with anisotropic displacement parameters, and hydrogen atoms were placed in idealized positions and refined as rigid atoms with the relative isotropic displacement parameters. SQUEEZE function equipped in the PLATON program was used to treat severely disordered solvent molecules in voids.[47,48]

Preparation of the catalysts

Carbon black Vulcan® XC-72R (VC, Cabot, USA) was used as a carbon support. The catalysts were prepared from the iron complexes, $[Fe(\mathbf{L1})_3]^{2+}$, $[Fe(\mathbf{L2})_2]^{2+}$, $[Fe(\mathbf{L4})_3]^{2+}$, $[Fe(\mathbf{L5})_3]^{2+}$, $[Fe(\mathbf{L6})_3]^{2+}$, or the mixture of **L3** and iron ion with VC by pyrolysis in N_2 gas flow; their names are abbreviated as Fe/**L1**@VC, Fe/**L2**@VC, Fe/**L4**@VC, Fe/**L5**@VC, and Fe/**L6**@VC, and Fe/**L3**@VC, respectively. The Fe/N/C catalysts were prepared as follows: one of the iron complexes or a mixture of **L3** and Fe^{2+} (0.05 mmol) was dissolved in CH_2Cl_2 (50 mL) and mixed with a powder of VC (100 mg). The suspension was vigorously vortexed and sonicated for 30 min, and then the solvent was removed. The obtained mixture was placed on an alumina boat (length: 80 mm, width: 16 mm, height: 10 mm) which was then placed in a quartz tube (diameter 50 mm, length 800 mm). The quartz tube was installed in a hinge split tube furnace (Koyo Thermo Systems Co. Ltd., KTF045N1). The mixture was heated from ambient temperature to 700 ºC (heating rate is 2 ºC·min^{-1}) for 2 h under N_2 flow (0.2 L·min^{-1}) and incubated for 2 h. The temperature of the

sample inside the furnace was recorded with a thermocouple equipped with a data logger (CHINO Corporation, MC3000). After cooling to ambient temperature, the pyrolyzed materials were ground to be uniform, and then, the Fe/N/C catalyst was obtained.

X-ray absorption spectrometric (XAS) analysis

In-situ electrochemical Fe K-edge XAS measurements were carried out at the beamline BL12C, Photon Factory (PF), Institute of Materials Structure Science (IMSS), KEK, Japan. The XAS data were collected at room temperature in the fluorescent mode using a manganese K-edge filter (absorption edge height = 3) and a 7-element silicon drift detector (SDD). A three-electrode electrochemical flow cell was utilized for the *in-situ* XAS experiments.[49,50] A Pt wire counter electrode and the Ag/AgCl (sat. KCl) reference electrode were used. The potential applying to the working electrode during the measurements were controlled using an Ivium Compactstat potentilstat. All *in-situ* XAS measurements were performed in a 0.1 M $HClO_{4aq}$ under N_2. To prepare working electrodes of Fe/**L1**@VC and Fe/**L2**@VC for *in-situ* XAS experiments, the catalyst ink containing the Fe/N/C catalysts (Fe/**L1**@VC, Fe/**L2**@VC) (4.0 mg) and 5% Nafion 117 dispersion (100 μL) was sonicated for at least 2 h, and then the ink (ca. 50 μL) was drop-cast on a gold film sputtered on a Kapton window. The resulting electrode was heated in an oven at 418 K for 5 min. *In-situ* XAS data were analyzed using software packages REX2000 (Rigaku Co.) or Athena (Demeter 0.9.24). Extended X-ray absorption fine structure (EXAFS) oscillation values, $\chi(k)$, in the k range from 3 to 12 $Å^{-1}$ were extracted from XAS spectra. The $k^3 \cdot \chi(k)$ values were Fourier-transformed into R-space, followed by the inverse Fourier transform into k-space for curve-fitting using the following equation:

$$\chi(k) = S_0^2 \sum_j \frac{N_j F_j(k) \exp(-2k^2\sigma_j^2)}{kR_j^2} \sin(2kR_j + \varphi_j(k))$$

where S_0^2 is the amplitude reduction factor, $F_j(k)$ is the effective curved-wave backscattering amplitude, N_j is the number of neighbors in the j^{th} atomic shell, R_j is the distance between the X-ray absorbing central atom and the atoms in the j^{th} atomic shell (backscatterer), $\varphi_j(k)$ is the phase function (including the phase shift for each shell and the total central atom phase shift), and σ_j is the Debye-Waller parameter of the j^{th} atomic shell (variation of distances around the average R_j). The $\varphi_j(k)$, and $F_j(k)$ were calculated using the FEFF8.20 program.[51,52] For FEFF calculations, a molecular geometry was taken from the single crystal X-ray analysis data of the iron complex of hexaaza macrocylic (HAM) ligand, $[(H_2O)\{Fe(H_2HAM)\}\mu\text{-}O)\{Fe(H_2HAM)\}(\mu\text{-}O)\{Fe\text{-}(H_2HAM)\}(OH_2)]Br_6$.[5] The curve-fitting analysis was performed using the REX2000 software package.[53,54]

Electrochemical measurements

The performance of the catalyst in ORR was evaluated in a 0.1 M $HClO_{4aq}$ solution. A rotating ring-disk electrode (RRDE) with a glassy carbon disk electrode (ϕ = 5 mm) and platinum ring was used for the electrochemical measurements. Electrode rotation rates were controlled using a Pine Instruments AFMSRCE rotator with a Pine MSRX motor controller. An electrode was polished to mirror flat with alumina powder (50 nm) before use. The catalyst ink was prepared with 4.0 mg of catalyst and 100 μL of 5 wt% Nafion® (Sigma–Aldrich) in a mixture of lower aliphatic alcohols and H_2O. The ink was vortexed and sonicated in an ultrasonic bath at 100 W at 35 kHz for 30 min. Then, 2 μL of catalyst ink was loaded onto the surface of the electrode and dried. Electrochemical tests were conducted with a potentiostat (ALS, electrochemical analyzer model 610B) using a typical three-electrode system, with platinum wire as a counter electrode and Ag/AgCl as a reference electrode. The potential difference between Ag/AgCl and RHE was calculated, and the value is 0.258 V in a 0.1 M $HClO_{4aq}$ solution. The scan rate was 5 $mV{\cdot}s^{-1}$ from −0.258 to 0.742 V vs. the Ag/AgCl reference electrode. Before each potential scan, the electrolyte of the 0.1 M $HClO_{4aq}$ solution was saturated with O_2 for at least 30 min, and O_2 purging was continued during the electrochemical experiments. The measured currents of disk and ring electrodes were subtracted from the background current at the N_2-saturated electrolyte. In the RRDE test, the ring potential was set to 1.0 V versus the Ag/AgCl reference electrode. The onset potentials (E_{onset}) are defined as a potential showing j = −0.05 $mA{\cdot}cm^{-2}$ in RDE measurement, where j represents the current density. The RRDE collection efficiency (N) was calibrated in 0.1 M $HClO_{4aq}$ solution with 10 mM $K_3Fe(CN)_6$ electrolyte. The measured N value is 0.26 in our system. The percentage of H_2O_2 in total amount of the product was calculated by equation 1:

$$X_{H_2O_2} = 2\,I_r\,(I_r + N \times |I_d|) \times 100 \quad \text{---------- (1)}$$

The TOF value which is defined as the number of electrons transferred per an active site and unit time (second) ($e{\cdot}site^{-1}{\cdot}s^{-1}$) was calculated by equation 2:

$$TOF = J_{kin}(0.8\ \text{V vs. RHE})/(MSD \times e) \quad \text{---------- (2)}$$

where J_{kin} (0.8 V vs. RHE) represents the gravimetric kinetic current density ($A{\cdot}g^{-1}$) at 0.8 V vs. RHE, MSD (mass-based site density) is the number of the Fe–N_x active sites normalized by mass of the catalyst ($sites{\cdot}g^{-1}$), and e is elementary charge. The J_{kin} value is calculated by equation 3:

$$J_{kin}(0.8\ \text{V vs. RHE}) = J_{lim} \times J(0.8\ \text{V vs. RHE})/(|J_{lim}| - |J(0.8\ \text{V vs. RHE})|) \quad \text{---------- (3)}$$

where J_{lim} represents the gravimetric limiting current density, and $J_{0.8\,V}$ is the gravimetric current density observed at 0.8 V vs. RHE. J_{lim} and $J_{0.8\,V}$ can be evaluated from the linear sweep voltammograms in the RDE measurement. MSD was evaluated by the cyclic voltammetry (CV) in an N_2-saturated 0.1 M $HClO_{4aq}$ solution at 50 $mV{\cdot}s^{-1}$ at 2000 rpm from −0.258 to 0.742 V vs. the Ag/AgCl reference electrode (Figure 3-15) and calculated by equation 4:

$$MSD = Q/(e \times n \times g_{cat})$$ ---------- (4)

where Q represents $Fe^{2+/3+}$ coulombic charge (C) calculated by the CV in an N_2-saturated solution, n is reaction number (n = 1 in this redox system), and g_{cat} is loaded weight of the catalyst (0.08 mg).

References and Notes

[1] S. Zaman, L. Huang, A. I. Douka, H. Yang, B. You, B. Y. Xia, *Angew. Chem. Int. Ed.* **2021**, *60*, 17832−17852.

[2] X. Zhao, L. Shao, Z. Wang, H. Chen, H. Yang, L. Zeng, *J. Mater. Chem. C* **2021**, *9*, 11252−11260.

[3] C.-X. Zhao, B.-Q. Li, J.-N. Liu, Q. Zhang, *Angew. Chem. Int. Ed.* **2021**, *60*, 4448−4463.

[4] S. K. Kaiser, Z. Chen, D. F. Akl, S. Mitchell, J. Pérez-Ramírez, *Chem. Rev.* **2020**, *120*, 11703−11809.

[5] M. Moriya, R. Takahama, K. Kamoi, J. Ohyama, S. Kawashima, R. Kojima, M. Okada, T. Hayakawa, Y. Nabae, *J. Phys. Chem. C* **2020**, *124*, 20730−20735.

[6] T. Marshall-Roth, N. J. Libretto, A. T. Wrobel, K. J. Anderton, M. L. Pegis, N. D. Ricke, T. V. Voorhis, J. T. Miller, Y. Surendranath, *Nat. Commun.* **2020**, *11*, 5283.

[7] U. Martinez, S. Komini Babu, E. F. Holby, H. T. Chung, X. Yin, P. Zelenay, *Adv. Mater.* **2019**, *31*, 1806545.

[8] A. Li, S. A. Nicolae, M. Qiao, K. Preuss, P. A. Szilágyi, A. Moores, M.-M. Titirici, *ChemCatChem* **2019**, *11*, 3602−3625.

[9] H. Fei, J. Dong, D. Chen, T. Hu, X. Duan, I. Shakir, Y. Huang, X. Duan, *Chem. Soc. Rev.* **2019**, *48*, 5207−5241.

[10] R. Jasinski, *Nature* **1964**, *201*, 1212−1213.

[11] Z. Chen, D. Higgins, A. Yu, L. Zhang, J. Zhang, *Energy Environ. Sci.* **2011**, *4*, 3167−3192.

[12] M. Kato, N. Fujibayashi, D. Abe, N. Matsubara, S. Yasuda, I. Yagi, *ACS Catal.* **2021**, *11*, 2356−2365.

[13] M. Lefèvre, E. Proietti, F. Jaouen, J.-P. Dodelet, *Science* **2009**, *324*, 71−74.

[14] Y. Tanaka, A. Onoda, S. Okuoka, T. Kitano, K. Matsumoto, T. Sakata, H. Yasuda, T. Hayashi, *ChemCatChem* **2018**, *10*, 743−750.

[15] A. Onoda, Y. Tanaka, K. Matsumoto, M. Ito, T. Sakata, H, Yasuda, T. Hayashi, *RSC Adv.* **2018**, *8*, 2892−2899.

[16] R. Bashyam, P. Zelenay, *Nature* **2006**, *443*, 63−66.

[17] M. Ferrandon, X. Wang, A. J. Kropf, D. J. Myers, G. Wu, C. M. Johnston, P. Zelenay, *Electrochim. Acta* **2013**, *110*, 282−291.

[18] G. Wu, K. L. More, C. M. Johnston, P. Zelenay, *Science* **2011**, *332*, 443−447.

[19] A. L. Bouwkamp-Wijnoltz, W. Visscher, J. A. R. van Veen, E. Boellaard, A. M. van der Kraan, S. C. Tang, *J. Phys. Chem. B* **2002**, *106*, 12993−13001.

[20] U. I. Kramm, I. Herrmann-Geppert, J. Behrends, K. Lips, S. Fiechter, P. Bogdanoff, *J. Am. Chem. Soc.* **2016**, *138*, 635−640.

[21] M.-X. Chen, M. Zhu, M. Zuo, S.-Q. Chu, J. Zhang, Y. Wu, H.-W. Liang, X. Feng, *Angew. Chem. Int. Ed.* **2020**, *59*, 1627−1633.

[22] W. Yang, T.-P. Fellinger, M. Antonietti, *J. Am. Chem. Soc.* **2011**, *133*, 206−209.

[23] H. Zhang, H. T. Chung, D. A. Cullen, S. Wagner, U. I. Kramm, K. L. More, P. Zelenay, G. Wu, *Energy Environ. Sci.* **2019**, *12*, 2548−2558.

[24] C. H. Choi, C. Baldizzone, G. Polymeros, E. Pizzutilo, O. Kasian, A. K. Schuppert, N. Ranjbar Sahraie, M.-T. Sougrati, K. J. J. Mayrhofer, F. Jaouen, *ACS Catal.* **2016**, *6*, 3136−3146.

[25] X. F. Lu, B. Y. Xia, S.-Q. Zang, X. W. Lou, *Angew. Chem. Int. Ed.* **2020**, *59*, 4634−4650.

[26] K. Matsumoto, A. Onoda, T. Kitano, T. Sakata, H. Yasuda, S. Campidelli, T. Hayashi, *ACS Appl. Mater. Interfaces* **2021**, *13*, 15101−15112.

[27] H. Petzold, P. Djomgoue, G. Hörner, S. Heider, C. Lochenie, B. Weber, T. Rüffer, D. Schaarschmidt, *Dalton Trans.* **2017**, *46*, 6218−6229.

[28] J. Maruyama, I. Abe, *Chem. Mater.* **2006**, *18*, 1303−1311.

[29] Z. Tian, C. Wang, Z. Si, L. Ma, L. Chen, Q. Liu, Q. Zhang, H. Huang, *Appl. Catal. A: Gen.* **2017**, *541*, 50−59.

[30] Y. J. Sa, J. Kim, S. Joo, *J. Electrochem. Sci. Technol.* **2017**, *8*, 169−182.

[31] L. Zhou, C. Yang, J. Wen, P. Fu, Y. Zhang, J. Sun, H. Wang, Y. Yuan, *J. Mater. Chem. A* **2017**, *5*, 19343−19350.

[32] M. Ferrandon, A. J. Kropf, D. J. Myers, K. Artyushkova, U. Kramm, P. Bogdanoff, G. Wu, C. M. Johnston, P. Zelenay, *J. Phys. Chem. C* **2012**, *116*, 16001−16013.

[33] J. Li, M. T. Sougrati, A. Zitolo, J. M. Ablett, I. C. Oğuz, T. Mineva, I. Matanovic, P. Atanassov, Y. Huang, I. Zenyuk, A. Di Cicco, K. Kumar, L. Dubau, F. Maillard, G. Dražić, F. Jaouen, *Nat. Catal.* **2021**, *4*, 10−19.

[34] N. Ramaswamy, U. Tylus, Q. Jia, S. Mukerjee, *J. Am. Chem. Soc.* **2013**, *135*, 15443−15449.

[35] S. Yasuda, Y. Uchibori, M. Wakeshima, Y. Hinatsu, H. Ogawa, M. Yano, H. Asaoka, *RSC Adv.* **2018**, *8*, 37600−37605.

[36] Y. Qin, L. Zhang, J. Lv, S. Luo, J.-P. Cheng, *Org. Lett.* **2015**, *17*, 1469−1472.

[37] J. Cai, C. A. Pignedoli, L. Talirz, P. Ruffieux, H. Söde, L. Liang, V. Meunier, R. Berger, R. Li, X. Feng, K. Müllen, R. Fasel, *Nat. Nanotechnol.* **2014**, *9*, 896−900.

[38] T. H. Vo, M. Shekhirev, D. A. Kunkel, M. D. Morton, E. Berglund, L. Kong, P. M. Wilson, P. A. Dowben, A. Enders, A. Sinitskii, *Nat. Commun.* **2014**, *5*, 3189.

[39] K. Keiichi, S. Takahiro, T. Norihiro, S. Naoki, *Chem. Lett.* **2007**, *36*, 11222−1123.

[40] S. Jakobse, M. Tilset, *Tetrahedron Lett.* **2011**, *52*, 3072−3074.

[41] J. Frey, T. Kraus, V. Heitz, J.-P. Sauvage, *Chem. Eur. J.* **2007**, *13*, 7584−7594.

[42] Rigaku Oxford Diffraction (2015), Software CrysAlisPro 1.171.39.20a. Rigaku Corporation, Tokyo, Japan.

[43] G. M. Sheldrick, *Acta Crystallogr. Sect. A* **2015**, 71, 3−8.

[44] Rigaku (2018). CrystalStructure. Version 4.3. Rigaku Corporation, Tokyo, Japan.

[45] O. V. Dolomanov, L. J. Bourhis, R. J. Gildea, J. A. K. Howard and H. Puschmann, H. *J. Appl. Cryst.* **2009**, *42*, 339–341.

[46] L. J. Bourhis, O. V. Dolomanov, R. J. Gildea, J. A. K. Howard and H. Puschmann, *Acta Crystallogr. Sect. A* **2015**, *71*, 59−75.

[47] P. V. D. Sluis, A. L. Spek, *Acta Crystallogr. Sect. A* **1990**, *46*, 194.

[48] A. L. Spek, *Acta Crystallogr. Sect. D* **2009**, *65*, 148−155.

[49] M. Kato, K. Kimijima, M. Shibata, H. Notsu, K. Ogino, K. Inokuma, N. Ohta, H. Uehara, Y. Uemura, N. Oyaizu, T. Ohba, S. Takakusagi, K. Asakura, I. Yagi, *Phys. Chem. Chem. Phys.* **2015**, *17*, 8638−8641.

[50] M. Kato, M. Muto, N. Matsubara, Y. Uemura, Y. Wakisaka, T. Yoneuchi, D. Matsumura, T. Ishihara, T. Tokushima, S. Noro, S. Takakusagi, K. Asakura, I. Yagi, *ACS Appl. Energy Mater.* **2018**, *1*, 2358−2364.

[51] S. I. Zabinsky, J. J. Rehr, A. Ankudinov, R. C. Albers, M. J. Eller, *Phys. Rev. B* **1995**, *52*, 2995−3009.

[52] J. J. Rehr, R. C. Albers, *Rev*. *Mod*. *Phys*. **2000**, *72*, 621−654.

[53] T. Taguchi, *AIP Conf*. *Proc*. **2006**, *882*, 162−164.

[54] T. Taguchi, T. Ozawa, H. Yashiro, *Phys*. *Scr*. **2005**, *2005*, 205.

Conclusions

M/N/C single-atom catalysts have a great potential to be developed dramatically because their well-defined structures of the active sites (M−N_x site) provide clear insights in the relationship between the structure and the catalytic activity. However, the method to synthesize M/N/C single-atom catalysts with high structural precision has been limited. In this context, the author proposed the new strategy for precisely constructing the M−N_x sites in the catalysts by applying the synthetic method to atomically defined nanographene compounds.

In the chapter 1, it was described that the Fe/N/C catalysts were prepared by pyrolysis of N-doped graphene nanoribbon (N-GNR) precursors, which are the polymers of triphenylene units containing preorganized aromatic rings, with iron salts and carbon substrates. The catalyst prepared from the N-GNR precursor contains the large amount of the Fe−N_x active sites and shows catalytic activity in ORR with a high onset potential of 0.88V vs. RHE in 0.1 M $HClO_{4aq}$. In addition, the details of the graphitization process of the precursor were investigated by analyzing the precursors pyrolyzed at various temperatures using MgO particles. The results verify that the Fe−N_x active sites are efficiently constructed via the intramolecular annulation and the graphitization of the N-GNR precursor.

In the chapter 2, the preparation of the Co/N/C catalysts was described. This was performed applying the method using N-GNR precursor demonstrated in the chapter 1. The Co/N/C catalysts from the N-GNR precursor exhibit superior catalytic activity toward HER with a low overpotential of 311 mV in 0.1 M $HClO_{4aq}$. Atomically dispersed Co−N_x sites in the catalysts are observed by electron microscopy. Moreover, the amount of Co−N_x sites increases up to 0.31 wt% as confirmed by XPS and elemental analysis. These results clearly show the advantage of the preparation method using the N-GNR precursors in the construction of the highly active Co−N_x sites in the Co/N/C catalyst.

In the chapter 3, development of the iron complexes containing chelating coordination structures as preorganized aromatic rings in a 1,12-diazatriphenylene framework tethering bromo substituents was described. They were used as precursors to precisely construct the Fe−N_4 active sites along with the nanographene structure in the Fe/N/C catalysts. One-step pyrolysis of the iron complex with carbon black forms the Fe−N_4 active sites without the iron aggregates. XAS and electrochemical measurements revealed that the iron complex with N3-coordination is precisely converted to the Fe−N_4 sites catalyzing ORR with a TOF value of 0.21 $e \cdot site^{-1} \cdot s^{-1}$ at 0.8 V vs. RHE. This indicates that the formation of the Fe−N_4 sites is controlled by precise tuning of the chemical structure of the precursor.

In conclusion, the author demonstrated the promising preparation method of M/N/C single-atom catalysts which is capable of the precise construction of the M−N_x sites. The use of the nanographene precursors containing preorganized aromatic rings. The thesis provides the new guideline in designing the chemical structure of precursors to promote the formation of the M−N_x sites during pyrolysis. Furthermore, the author believes that the strategy for the preparation of M/N/C catalysts described in the thesis is applicable to the wide range of carbon-based catalysts and contributes to further development of the catalysts containing an atomically defined structure of an active site.

List of Publications

1. Thermally Controlled Construction of Fe−N_x Active Sites on the Edge of a Graphene Nanoribbon for an Electrocatalytic Oxygen Reduction Reaction
   Koki Matsumoto**,** Akira Onoda, Tomoyuki Kitano, Takao Sakata, Hidehiro Yasuda, Stéphane Campidelli, and Takashi Hayashi
   ACS Appl. *Mater*. *Interfaces*, **2021**, *13*, 15101–15112. DOI: 10.1021/acsami.0c21321

2. Electrocatalytic Hydrogen Evolution Reaction Promoted by Co/N/C Catalysts Containing Co−N_x Active Sites Derived from Precursors Forming N-doped Graphene Nanoribbons
   Koki Matsumoto, Akira Onoda, Stéphane Campidelli, and Takashi Hayashi
   Bull. *Chem*. *Soc*. *Jpn*., **2021**, *94*, 2898–2905. DOI: 10.1246/bcsj.20210302

3. One-step Preparation of Fe/N/C Single-atom Catalysts Containing Fe−N_4 Sites from an Iron Complex Precursor with 5,6,7,8-Tetraphenyl-1,12-diazatriphenylene Ligands
   Koki Matsumoto, Masaru Kato, Ichizo Yagi, Siqi Xie, Kiyotaka Asakura, Shin-ichiro Noro, Norimitsu Thonai, Stéphane Campidelli, Takashi Hayashi, and Akira Onoda
   Chem. *Eur*. *J*. **2021**, *27*, 1−6. DOI: 10.1002/chem.202103545

List of Supplementary Publications

1. Nonprecious-metal Fe/N/C Catalysts Prepared from π-Expanded Fe Salen Precursors toward an Efficient Oxygen Reduction Reaction
   Yuta Tanaka, Akira Onoda, Shin-ichi Okuoka, Tomoyuki Kitano, Koki Matsumoto, Takao Sakata, Hidehiro Yasuda, Takashi Hayashi
   ChemCatChem, **2018**, *10*, 742–750. DOI: 10.1002/cctc.201701629

2. Bimetallic M/N/C Catalysts Prepared from π-expanded Metal Salen Precursors toward an Efficient Oxygen Reduction Reaction
   Akira Onoda, Yuta Tanaka, Koki Matsumoto, Minoru Ito, Takao Sakata, Hidehiro Yasuda, Takashi Hayashi
   RSC Adv., **2018**, *8*, 2892–2899. DOI: 10.1039/c7ra12657c

Acknowledgements

The study presented in this thesis has been carried out at Department of Applied Chemistry, Graduate School of Engineering, Osaka University from April 2016 to March 2022. The author would like to express his best gratitude to Professor Takashi Hayashi for his continuous guidance, insightful suggestion, constant discussions, and warm encouragement throughout this research. The author would like to deeply thank Professor Akira Onoda for his kind and continuous guidance, valuable suggestions, and helpful discussions. The author also acknowledges Professor Susumu Kuwabata and Professor Satoshi Minakata for reviewing this thesis and their valuable suggestions.

Acknowledgements are also made to Professor Norimitsu Tohnai at Department of Applied Chemistry, Graduate School of Engineering, Osaka University for technical support and valuable discussions on Thermogravimetry-Differential Thermal Analyzer measurements, and X-ray crystal structural analysis. The author acknowledges Mr. Takao Sakata, and Professor Hidehiro Yasuda at the Research Center, Osaka University for their technical support and insightful comments on ultra-high voltage electron microscopic observations. The author would like to specially thank Dr. Tomoyuki Kitano at the Analysis Technology Center, Nippon Shokubai Co., Ltd, for their sincerely technical support and suggestions for X-ray Absorption Fine Structure measurements and Extended X-ray Absorption Fine Structure analysis. The author would like to express his gratitude to Associate Professor Shinji Tamura, and Professor Nobuhito Imanaka at Department of Applied Chemistry, Graduate School of Engineering, Osaka University for their technical support on X-ray diffraction analysis and Raman spectroscopy. The author acknowledges Associate Professor Masaru Kato, and Professor Ichizo Yagi at Faculty of Environmental Earth Science, Hokkaido University for their technical supports and valuable discussions on electrochemical measurements and X-ray Absorption Spectroscopy measurements. The author would like to express his gratitude to Professor Kiyotaka Asakura at Catalyst Surface Research Division, Institute for Catalysis, Hokkaido University for their technical supports and insightful comments on X-ray Absorption Spectroscopy measurements. The author also acknowledges Professor Shin-ichiro Noro at Faculty of Environmental Earth Science, Hokkaido University for his technical supports and helpful discussions on X-ray diffraction analysis and specific surface area measurements by Brunauer-Emmett-Teller theory. The author would like to thank Ms. Naomi Hirai at Research Institute for Electronic Science, Hokkaido University for her kind technical supports and helpful discussion on Scanning Transmission Electron Microscopy and Electron Energy Loss Spectroscopy measurements.

The author would like to express his gratitude to Associate Professor Koji Oohora for his helpful suggestion and insightful discussion. Acknowledgement is also made to Ms. Kiyomi Lee for her kind help in laboratory life, and all members at Professor Hayashi's group for their discussions, encouragements, and friendship.

Finally, the author expresses great gratitude to his family, Tsunetaka, Yukari, and Fuka for their heartfelt assistance and encouragements.

This study was financially supported by Research Fellowship of Japan Society for the Promotion of Science for Young Scientists.

Koki Matsumoto

January 2022